Design of Metallic Nanocomposites for High-Strength, Plasticity and Fracture Resistance

by

Yuchi Cui

A dissertation submitted in partial fulfillment
of the requirements for the degree of
Doctor of Philosophy
(Materials Science and Engineering)
in The University of Michigan
2020

Doctoral Committee:

Professor Amit Misra, chair
Professor Fei Gao
Professor Liang Qi
Associate Research Scientist Kai Sun

Yuchi Cui

tedcui@umich.edu

ORCID iD: 0000-0001-6004-6105

For my loved ones and for all the heroes fighting against the coronavirus.

Acknowledgements

I would like to express my most sincere gratitude to my thesis advisor, Professor. Amit Misra, for your time, guidance and constant support, since the first day I became your student. None of these will happen without you. I would also like to thank the rest of my dissertation committee, Professor Fei Gao, Professor Liang Qi and Dr. Kai Sun, for your insights and valuable critiques. Special thanks to Dr. Kai Sun, for leading me into the wonderland of electron microscopy.

I would also like to thank Dr. Nan Li at Los Alamos National Laboratories, who generously passed me his knowledge on *in situ* nanomechanical testing techniques, and his colleague, Mr. Kevin Baldwin, who provided essential samples for my experiments. I thank our collaborators Nathan Beets and Dr. Diana Farkas from Virginia Polytechnic Institute and State University, for your hard work on simulation support and insightful discussion. My thanks also go to Dr. Haiping Sun, Dr. Bobby Kerns and Dr. Allen Hunter at Michigan Center for Materials Characterization, for your technique support with the electron microscopes and nanoindenters, which were the vital tools for my research.

I owe many thanks to all my current and former colleagues, who have made this journey more pleansant and productive, Dr. Qian Lei, Ben Derby, Dr. Zhihua Huang, Dr. Shujuan Wang, Mohsen Taheri, Max Powers, Huai-Hsun Lien, Dr. Li Jiang, Nicholas Etrick and Dr. Arya Chatterjee.

Last but not least, I must thank my family for your unconditional love and support: my mother, Qizhi Li, for blindly believing in me, my father, Dr. Gang Cui, for setting the best role model for me, and my grandparents, for your understanding and emotional sacrifice. 最后也是最重要的我要感谢我的家人对我无条件的爱和支持。我亲爱而伟大的母亲，李奇志女士，谢谢你对我近乎“盲目”的信任和包容。我的父亲，崔刚先生，谢谢你以身作则，给我树立榜样。我亲爱的爷爷奶奶外公外婆，谢谢你们的理解宽容和情感上的牺牲。

I acknowledge the support from NSF under the DMREF program. Electron microscopy was performed partly at the Michigan Center for Materials Characterization operated by the College of Engineering, University of Michigan. This work was performed, in part, at the Center for Integrated Nanotechnologies, an Office of Science User Facility operated for the U.S. Department of Energy (DOE) Office of Science. Los Alamos National Laboratory, an affirmative action equal opportunity employer, is managed by Triad National Security, LLC for the U.S. Department of Energy’s NNSA, under contract 89233218CNA000001.

Table of Contents

Dedication ……...ii
Acknowledgement……..…….…. iii
List of Figures ……..……vii
Abstract…….……..…..xiv
Chapter 1 Introduction 1
1.1 References 5
Chapter 2 Background 6
2.1 Achieving high strength in metallic materials 6
2.2 Metallic nanolayered composites (MNLC) 8
2.2.1 Interface strengthening in MNLCs 8
2.2.2 Length-scale-dependent deformation mechanisms of MNLCs 10
2.2.3 Modes for shear band formation in MNLCs 12
2.3 Strategies to prevent flow localization 19
2.3.1 Increasing strain hardening rate 19
2.3.2 Flow delocalization in MNCs 20
2.4 Measurements of hardness and elastic modulus using nanoindentation 23
2.5 *In situ* nanomechanics in transmission electron microscope (TEM) 26
2.5.1 Deformation twin vs dislocation pile-up against interface 27
2.5.2 Dislocation confined layer slip mechanism 30
2.5.3 Interface mediated deformation twinning mechanism 30
2.5.4 Room temperature dislocation climb at interfaces 32
2.5.5 Fracture mechanisms in multilayers 34
2.5.6 Measurement of the shear strength of the interface 35
2.5.7 Phase transitions and grain activities 38

2.6 References 40
Chapter 3 Experimental 47
3.1 Synthesis of Metallic nanocomposites through physical vapor deposition 47
3.2 Morphological Characterization of nanocomposites 49
3.3 Nanoindentation test 51
3.4 In situ nanomechanical testing 52
3.4.1 Platforms for in situ nanomechanical testing 52
3.4.2 In situ micro-/nano pillar compression 54
3.4.3 In situ Tensile test in TEM 56
3.4.4 In situ pre-notched 3-point bend test in SEM 57
3.5 References 59
Chapter 4 Deformation Mechanisms of Monolithic Cu/Mo Nanocomposites 60
4.1 Introduction 60
4.2 Experimental 64
4.3 Results 65
4.3.1 Multilayer nanocomposite with mixed interfaces 65
4.3.2 LCM nanocomposite with coherent interfaces 67
4.3.3 LCM nanocomposite with semi-coherent interfaces 69
4.3.4 RCM nanocomposite with semi-coherent interfaces 71
4.4 Discussion 73
4.4.1 Shear banding in the multilayer 73
4.4.2 Strain localization in the coherent LCM nanocomposite 75
4.4.3 Kink banding in the semi-coherent LCM nanocomposite 76
4.4.4 Enhanced deformability in the semi-coherent RCM nanocomposite 78
4.5 Conclusions 85

4.6 References 86
Chapter 5 Suppression of Shear Band in Hierarchical Cu-Mo Nanocomposites 89
5.1 Introduction 89
5.2 Experimental 90
5.3 Microstructure and mechanical behavior 90
5.3.1 Nanocomposite with coarse-length-scale bicontinuous zones 90
5.3.2 Nanocomposite with fine-length-scale bicontinuous zones 93
5.4 Discussion 96
5.4.1 Low-strength hierarchical nanocomposite without shear banding 96
5.4.2 High-strength hierarchical nanocomposite without shear banding 97
5.5 Conclusions 98
5.6 References 100
Chapter 6 Fracture Resistance of Hierarchical Cu-Mo Nanocomposite Thin Film 101
6.1 Introduction 101
6.2 Experimental 104
6.3 Results 105
6.4 Discussion 115
6.4.1 Crack initiation 115
6.4.2 Crack growth 118
6.5 Conclusions 121
6.6 References 123
Chapter 7 Conclusions and future work 126
7.1 Conclusions 126
7.2 Future work 129

List of Figures

Figure 2.1 Schematic showing structure of a MNLC. A and B represent two different metals. 7
Figure 2.2 Plot of hardness as a function of inverse square root of layer thickness in several Cu-based MNLCs. [34] 10
Figure 2.3 Schematic illustration of the key unit processes that determine the yield mechanism in LMC [40]. 11
Figure 2.4 (a) Schematic illustration of shear banding in coherent MNLC, (b) TEM image showing rotation and shearing at the corner of Al/Al_3Sc pillar [46]. 13
Figure 2.5 (a) TEM image showing shear band in Cu/Nb MNLC, (b) schematic illustration of dislocation movement under uniaxial loading, (c) non-uniaxial loading where interface rotate to shear orientation and (d) TEM image showing shear band in 5 nm Cu/Nb MNLC after nanoindentation [37]. 14
Figure 2.6 Cross-sectional bright-field TEM image showing region of macroshear in 50 nm Al/Nb MNLC [29]. 15
Figure 2.7 SEM image showing (a, b) h=100 nm and (c, d) h=50 nm micropillars (e, f) h=20 nm micropillars showing shear deformation and co-deformation; (g, h) h=5 nm micropillars showing highly localized shear banding by interface crossing [47] 16
Figure 2.8 Deformation map for Cu/Zr and Cu/Cr systems [47] 16
Figure 2.9 Schematic illustration of (a) buckling-assisted GB sliding of the 25 nm Au/Cu multilayer and (b) dislocation plasticity-dominated shearing of the 250 nm multilayer [28]. 17
Figure 2.10 SEM images showing the deformation in (a) 25 nm Au/Cu multilayer and (b) 250 nm multilayer [28]. 18
Figure 2.11 TEM images of the λ=20 nm Al/Pb pillar showing bending of individual layers and shearing [48]. 18
Figure 2.12 Stress-strain plot showing Considere's criterion for necking. 19

Figure 2.13 SEM backscattered electron image of *in situ* composite microstructure. (inset: X-ray diffraction pattern for the composite) [18]..... 20
Figure 2.14 SEM image showing shear band pattern array from compressive failure region of bend test specimen [18]. 21
Figure 2.15 (a) SEM micrograph of a Ta–Cu composite; (b) SEM micrograph of the composite with Cu dissolved away; (c) SEM micrograph of a composite with a 5μm ligament size. (d) Elemental mapping overlay of (c): green is Ta, red is Cu, and blue is residual Ti in Cu-rich phase [20]..... 22
Figure 2.16 Schematics showing geometry of the indenter tips (a) spherical, (b) conical, (c) Vickers and (d) Berkovich [57]..... 23
Figure 2.17 A schematic representation of a section through an indentation [56]. 24
Figure 2.18 A schematic representation of load versus indenter displacement curve [56]. 25
Figure 2.19 TEM images showing **(a)** continuous deformation twin across Cu/Ag interface, (**b)** thickening of the deformation twin in two phases, **(c)** generation of stacking faults in Ag with leading partials against the interface, (**d)** absorption of the leading and trailing partials by the interface, **(e)** emission of a perfect dislocation in Cu, **(f)** dislocation pile-up in Ag, **(g)** and **(h)** cross-slip of dislocations out of the pile-up and emission of dislocations back into Ag [85]. 28
Figure 2.20**.** MD simulations showing (**a)** initial cube-on-cube AgCu interface, **(b)** partial dislocation transmitted from Ag to Cu and the twin thickened from the partial dislocation indicated by the arrowhead, **(c)** partial dislocation in Ag accommodated by the interface and (**d)** nucleation of a partial back into Ag and emission of two perfect dislocations in Cu. 29
Figure 2.21 *In situ* TEM study on Cu/Nb multilayer showing (a)-(c) confined layer slip and formation of new dislocations, (d)-(e) dislocation emission from the interfaces and (f) co-deformation of the nanolayers. 31
Figure 2.22(a)-(c) *In situ* TEM study on ARB process Cu/Nb multilayer showing formation of deformation twin from twin nuclei 1 and 2 and (d) HRTEM image at the twin boundary. 32
Figure 2.23 HRTEM snapshots showing dislocation climb and annihilation near Al/Nb interface. 33

Figure 2.24 TEM images showing **(a)** formation of microcrack, **(b)** crack deviation, **(c)**layer necking and (**d)**crack blunting of 65 nm Cu/150 nm Nb MNC [100], and snapshots from the tensile test on 63 nm Cu/Nb when the load is **(e)** parallel to the interface and **(f)** perpendicular to the interfaces [101]. 35
Figure 2.25 (a) Displacement and load data record during the test, point b to d correspond to images b to d, (b) to (d) *in situ* TEM study on Cu/Nb multilayer showing shearing at the interface. 37
Figure 2.26 TEM image of the NiTi pillar (a) before the test. (b) after compressed for 20% engineering strain. Inset: diffraction patterns. 38
Figure 2.27 Sequential extracts from dark -filed TEM video recorded during *in situ* nanoindentation on nanocrystalline Al. 39
Figure 3.1 Schematics of (a) conventional sputtering chamber with two targets and (b) magnetron sputtering process..... 47
Figure 3.2 Process of conventional preparation of TEM sample..... 49
Figure 3.3 Process of preparing H-bar TEM sample. 50
Figure 3.4 Process of preparing TEM sample using FIB lift-out technique. 51
Figure 3.5 Photos of (a) Hysitron PI95 Picoindenter, (b) Hysitron PI85 Picoindenter inside an SEM chamber, and (c) Thermo Fisher STM-TEM holder..... 53
Figure 3.6 (a)-(c) SEM images taken during the fabrication of a nanopillar. (d) Schematic showing taper angle of a nanopillar. (e) Process of making taper-free pillars. (f)(g) Micro-pillar with no taper angle. 55
Figure 3.7 (a) SEM image of the push-to-pull device. Inset: photo of the deviced mounted on a sample state; (b) SEM image of the working part of the push-to-pull device. (c) to (i) Process of fabricating a tensile test sample using FIB lift-out technique..... 57
Figure 3.8 Schematics showing the process of making pre-notched bean for *in situ* bend test.... 58
Figure 1.1 Schematics of nanocomposites with a vertical concentration modulation, b lateral concentration modulation and c random concentration modulation. 62
Figure 1.2 (a) TEM image of the Cu/Mo multilayer; inset: SADP of the circled area. (b) Atomic images showing Cu layer having BCC (left) and FCC (right) structures. (c) STEM image of

indented multilayer. (d) STEM images of the top region of a multilayer nanopillar after the compression test. 66
Figure 1.3 True stress-strain curved obtained from the nanopillar compression test. 67
Figure 1.4 (a) cross-sectional STEM image of the coherent LCM nanocomposite, inset: SADP of the region; (b) atomic image across a coherent Cu/Mo interface; (c) plan-view STEM image of the sample; (d) STEM image of the nanopillar after compression test. 68
Figure 1.5 (a) cross-sectional STEM images of the semi-coherent LCM nanocomposite, inset: SADP of the region; (b) atomic image across a semi-coherent Cu/Mo interface; c plan-view STEM image of the sample; (d) STEM images of the nanopillar after 33% compression; (e) high magnification image showing the kink band at the top of the pillar and (f) STEM image of the nanopillar after 10 % compression. 70
Figure 1.6 STEM images (a) cross-sectional view of the semi-coherent RCM nanocomposite, inset: SADP of the region; (b) atomic image across a semi-coherent Cu/Mo interface; (c) plan-view of the sample; (d) nanopillar compression test. 72
Figure 1.7 Schematics showing (a) formation of shear band in the multilayer from dislocations cutting the interface, (b) localized shearing semi-coherent LCM structure, (c) kink band formation in semi-coherent LCM structure, (d) slip systems in two metals have K-S OR and (e) deformation events in a semi-coherent RCM structure. 74
Figure 1.8 (a) Image of the computational sample with 15 nm ligament diameter, (b) stress-strain curves obtained from simulations, (c) stress evolution in each phase, (d) emission of dislocation into the Cu phase during simulation, (e) evolution of residual dislocation density during the compression test, (f) non-uniform displacement maps obtained from the Mo and Cu phases respectively. 82
Figure 1.1 (a) Cross-sectional view STEM image of the nanocomposite with coarse-length-scale bicontinuous zones; inset: SADP of the region. (b) plan-view STEM image of the bicontinuous layer. (c) STEM image of the Cu layer showing Mo particles; inset: atomic image of a Mo particle showing FCC structure. (d) Schematics showing the 3D structure of the nanocomposite. (e) STEM

image of the deformed sample. (f) TEM images of the nanopillars at different plastic strains during the *in situ* nanocompression test. 91
Figure 1.2 Engineering stress-strain curves obtained from the nanopillar compression tests. 92
Figure 1.3 TEM images showing interface shearing during an off-axis compression test. 93
Figure 1.4 (a) Cross-sectional view STEM image of the nanocomposite with fine-length-scale bicontinuous zones. (b) STEM image showing the fine layered structure; inset: SAPD of the region. (c) Atomic image of a few Cu/Mo layers. (d) Plan-view STEM image of the Mo-rich matrix. (e) 3D schematics of the bicontinuous zone. (f) STEM image of the Cu islands. (g) STEM images of the indented area. (h) STEM image of the nanopillar before and after compression test..... 94
Figure 1.5 (a) dislocation pile-up in submicron scale Cu and Mo and (b) slip systems in a bicontinuous intertwined morphology. 96
Figure 6.1 SEM images showing the setup for (a) the notched micro-beam bend test, (b) the pillar compression test, (c) sample selection for the *in situ* tensile test, yellow: Cu-rich phase, blue: Mo-rich phase, and (d) tensile test sample glued to the push-to-pull device..... 104
Figure 6.2 Cross-sectional STEM images of (a) the hierarchical Cu-Mo nanocomposite , inset: SADP of the region; (b) the hierarchical Cu-Mo nanocomposite at a higher magnification, inset: schematic of the two phases; (c) atomic resolution inside the Cu-rich domain showing both bcc and fcc Mo precipitates. and (d) schematic showing 3-dimensional structure of the nanocomposite. 106
Figure 6.3 Cross-sectional TEM images of the 5 nm Cu/5 nm Mo multilayer nanocomposite at two magnifications, inset: SADP of the region. The yellow arrow indicates the film growth direction. 108
Figure 6.4 Stress-deflection curves for the nanocomposites measured from the *in situ* notched bend tests. 109
Figure 6.5 Snapshots captured during the in situ tests showing (a) crack opening displacement, (b) crack growth in 5 nm Cu/Mo multilayer, (c) multiple cracking in hierarchical nanocomposite, and (d) crack defection via shear along the Cu/Mo interface in hierarchical nanocomposite..... 110

Figure 6.6 Plot of (a) *J*-internal vs. crack length and (b) K_I vs. crack length measured during the bend test for the hierarchical nanocomposite. Upper bound values were calculated using compressive yield strength and lower bound values were calculated using tensile fracture stress. 111
Figure 6.7 STEM images showing (a) crack propagation at an early stage, red arrows: breakage at the Mo-rich layers, yellow arrows: bridging at the copper-rich layers; (b) local shear crack along the interface..... 112
Figure 6.8 Engineering stress-strain curves measured from the *in situ* tensile tests on the Cu-rich composite domains (yellow) and the Mo-rich composite domains (blue) in the hierarchical composite (Figure 1c and d show the locations in the microstructure from where the tensile samples were cut and the test geometry, respectively); inset: snapshots from the tests..... 114
Figure 6.9 Schematic of the three toughening mechanisms. Purple arrow: bridging of the crack by the soft composite; red arrow: shear crack along the interface; blue arrow: multiple cracking. 119

Abstract

In metallic materials, flow strength and plasticity are typically mutually exclusive and there is a pressing demand for the design of nanostructures that will solve the strength-deformability trade-off. Metallic nanocomposites (MNC) have been studied to exhibit high uniaxial strengths in the form of multilayers, with a general "smaller is stronger" trend in terms of the layer thickness. However, localized deformation in the form of shear bands results in limited deformability of these multilayer MNCs. It was hypothesized that, through high-temperature co-sputtering of two immiscible metals, novel morphological designs at nano-scale, including bicontinuous intertwined structure and heterogeneous structures where larger crystalline phases present, will be produced and they will promote plasticity while maintaining high strength of the nanocomposite. Cu-Mo nanocomposites with various morphologies have been prepared via high-temperature co-sputtering, including vertical concentration modulation (VCM), lateral concentration modulation (LCM), random concentration modulation (RCM) structures and a hierarchical "composite of composites" architecture where sub-micron scale Cu-rich islands containing Mo nano-precipitates are dispersed in a matrix of phase-separated Cu-Mo with nanoscale ligaments. Through advanced electron microscopy characterizations and *in situ* nanomechanical testing, deformation mechanisms of these nanocomposites have been studied and related to the nanostructures. High flow stress over 2 GPa were measured from all these nanocomposites. It has been discovered that the VCM and LCM structures lack uniform deformability due to the formation of localized shear

bands or kink bands. On the other hand, uniform deformability was observed in the rest two structures: the RCM or bicontinuous intertwined structure and the hierarchical structures. The complexity in the RCM structure poses geometric constraint on the softer Cu phase, promoting strain hardening and thus increasing the strength of the material. The tortuous interfaces effectively block the propagation of local strain concentration, resulting in the uniform deformation. In the hierarchical structure, the stronger matrix provides strength while the larger grain-size Cu-rich island promote deformability. The hierarchical structure has also been shown to have significant higher fracture resistance compared to the multilayers. These findings will provide insights to the understanding of interface microstructure-induced plasticity and fracture toughness enhancement in metallic materials and thus facilitate the design of metallic nanocomposites for advanced structural applications.

Chapter 1 Introduction

Metallic materials play essential roles in human history and the advancement of civilization, the discovery, development and utilization of which have been directing the way that people live and societies evolve. One important application of metallic materials is serving for structural purposes, owing to their superior mechanical properties, strength and deformability being the two most important aspects. The combination of high strength and good deformability has always been sought after for the safe application of a metallic material under various loading environments. The strength of a material describes its ability to withstand an applied load without failure or plastic deformation, or in other words, its ability to resist deformation. Deformability is a measure of the extent of deformation a material can sustain before failure. The deformation of a metallic material generally includes two parts: the elastic portion and the plastic portion. Elastic deformation is related to the stretching or compressing of the atomic bonding and fully recoverable after the applied load is removed. It is typically characterized as the linear segment of the stress-strain curve from a standard tensile test, the gradient of which is the elastic modulus of the material. On the other hand, plastic deformation is permanent, non-recoverable after load removal, and determines the strength, deformability and failure mode of a material. Complex interplay of defects is involved during plastic deformation, which may involve dislocation slip, twining, shear banding, dislocation-grain boundary interactions and phase transformations. Manipulation of these defects

will tailor the mechanical behavior of the material for desired applications. Common practices include increasing dislocation density through mechanical or thermal routes, introducing precipitates, tuning grain size and microstructure, and triggering phase transformations. It is crucial to study the evolution of these defects so that they can be harnessed to facilitate the development of advanced metallic materials that will survive more and more stringent loading conditions for modern engineering applications.

A conventional approach to study the deformation is *post-mortem*, which is a Latin phrase borrowed from the medical world meaning investigation of a dead body to determine the cause of death. In the context of materials study, *post-mortem* denotes that the materials and defects within are examined after the applied load is removed. For instance, transmission electron microscopy (TEM) enables the observation of dislocation structures induced by deformation, and electron backscatter diffraction (EBSD) helps to investigate the change in crystallographic orientation and texture[1-3]. The dynamic evolution of defect structures can only be postulated, without direct evidence. With the development of advanced electron microscopy and small-scale mechanical testing apparatus, *in situ* testing inside electron microscopes is gaining popularity in studying deformation of metallic materials. In Latin, *in situ* means “on site” or in the original place. *In situ* mechanical test indicates that the test is conducted inside a microscope, where images are taken during the deformation process[4-6]. In many cases, the load and displacement data are recorded to quantify the mechanical properties and determine the stress states that certain deformation events take place.

There are, in general, three aspects that *in situ* straining experiments in electron microscopes are helpful and essential in studying the deformation of advanced metallic materials. First, metallic nanocomposites are currently fabricated only in relatively small scale, such as in the

thin film form, which is only a few hundred nm to a few μm thick. Conventional testing methods cannot be applied to these materials due to this limitation in size. *In situ* micro- and oftentimes nano- mechanical testing methods are being developed to measure the compressive, tensile and bending behavior at small scale. Second, *in situ* experiments enable the acquisition of data on dynamic changes in the material. The most advanced charge-coupled device (CCD) camera today is able to capture images at a remarkable speed of a few thousand frames per second. Processes like dislocation interactions, twinning/de-twinning, dislocation/grain boundary interaction and phase transformations can be studied under direct observation[7-9]. Another advantage of *in situ* approach is that grains with different orientations or phases with different chemical compositions can be studied individually with careful experimental design and sample preparation[10].

In this dissertation, the utilization of *in situ* straining experiments to better understand the deformation of metallic nanocomposites will be explored. The focus of my Ph.D. research is to investigate the deformation and fracture mechanisms in thin film metallic nanocomposites and thus develop the best structure for high-strength and simultaneous plastic deformability and fracture resistance. It was hypothesized that nanocomposites with different structures could be produced by elevated-temperature co-sputtering two immiscible metals together. Among the achievable structures, a bicontinuous intertwined structure and heterogeneous structures where larger crystalline phases present are hypothesized to possess simultaneous high strength, uniform plastic deformability and improved fracture toughness. Cu and Mo are chosen as the model system because they have positive heat of mixing and thus are immiscible even at high temperatures. More importantly, Cu being face-centered-cubic (fcc) in crystal structure and Mo being body-centered-cubic (bcc), their semi-coherent interface presents strong barrier to dislocation transmission. In addition, the elastic modulus and melting temperature (in ^{o}C) of Mo are more than twice the values

of Cu, suggesting that a composite formed from the two metals have high strength. The maximum flow stress of a 5 nm Cu/5 nm Mo multilayer was measured at 2.8 GPa [11]. Cu-Mo nanocomposites with various structures including vertical concentration modulation (VCM), lateral concentration modulation (LCM), random concentration modulation (RCM), and "composite of composites" hierarchical structures were prepared through high-temperature co-sputtering. Nanopillars of these nanocomposites were fabricated using focused ion beam (FIB) to conduct *in situ* compression test. In Chapter 4, the mechanical behavior of the hierarchical structures is presented and compared with that of Cu/Mo multilayers prepared through sequential deposition of Cu and Mo layers [12]. Shear band suppression was observed in the hierarchical structures. Chapter 5 continues to discuss the deformation of the LCM and RCM nanocomposites [13, 14]. It was found that the RCM, or a bicontinuous intertwined structure provides simultaneous high strength and good deformability. To further investigate the mechanical behavior of the nanocomposites, *in situ* pre-notched 3-point bend test was designed. As discussed in Chapter 6, significant fracture resistance was measured in the hierarchical structure, suggesting interface microstructure induced mechanisms of hindrance to crack propagation [15].

1.1 References

1. Staker, M. and D. Holt, *The dislocation cell size and dislocation density in copper deformed at temperatures between 25 and 700 C.* Acta Metallurgica, 1972. **20**(4): p. 569-579.
2. Prinz, F. and A. Argon, *Dislocation cell formation during plastic deformation of copper single crystals.* Physica status solidi (a), 1980. **57**(2): p. 741-753.
3. Gholinia, A., P. Prangnell, and M. Markushev, *The effect of strain path on the development of deformation structures in severely deformed aluminium alloys processed by ECAE.* Acta Materialia, 2000. **48**(5): p. 1115-1130.
4. Cui, Y., N. Li, and A. Misra, *An overview of interface-dominated deformation mechanisms in metallic nanocomposites elucidated using in situ straining in a TEM.* Journal of Materials Research, 2019. **34**(9): p. 1469-1478.
5. Minor, A.M., J.W.M. Jr., and E.A. Stach, *Quantitative in situ nanoindentation in an electron microscope.* Applied Physics Letters, 2001. **79**(11): p. 1625-1627.
6. Haque, M.A. and M.T.A. Saif, *In-situ tensile testing of nano-scale specimens in SEM and TEM.* Experimental mechanics, 2002. **42**(1): p. 123-128.
7. D De Hosson, J. T., Soer, W. A., Minor, A. M., Shan, Z., Stach, E. A., Asif, S. S., & Warren, O. L., *In situ TEM nanoindentation and dislocation-grain boundary interactions: a tribute to David Brandon.* Journal of materials science, 2006. **41**(23): p. 7704-7719.
8. Li, N., Wang, J., Misra, A., & Huang, J. Y., *Direct observations of confined layer slip in Cu/Nb multilayers.* Microscopy and microanalysis, 2012. **18**(5): p. 1155-1162.
9. Wang, J., Zeng, Z., Weinberger, C. R., Zhang, Z., Zhu, T., & Mao, S. X., *In situ atomic-scale observation of twinning-dominated deformation in nanoscale body-centred cubic tungsten.* Nature materials, 2015. **14**(6): p. 594-600.
10. Schneider, A. S., Clark, B. G., Frick, C. P., Gruber, P. A., & Arzt, E., *Effect of orientation and loading rate on compression behavior of small-scale Mo pillars.* Materials Science and Engineering: A, 2009. **508**(1-2): p. 241-246.
11. Li, N., Demkowicz, M., Mara, N., Wang, Y., & Misra, A. , *Hardening due to Interfacial He Bubbles in Nanolayered Composites.* Materials Research Letters, 2016. **4**(2): p. 75-82.
12. Cui, Y., Derby, B., Li, N., Mara, N. A., & Misra, A., *Suppression of shear banding in high-strength Cu/Mo nanocomposites with hierarchical bicontinuous intertwined structures.* Materials Research Letters, 2018. **6**(3): p. 184-190.
13. Cui, Y., Derby, B., Li, N., Mara, N. A., & Misra, A., *Design of bicontinuous metallic nanocomposites for high-strength and plasticity.* Materials & Design, 2019: p. 107602.
14. Beets, N., Cui, Y., Farkas, D., & Misra, A. , *Mechanical response of a bicontinuous copper–molybdenum nano-composite: Experiments and simulations.* Acta Materialia, 2019. **178**: p. 79-89.
15. Yuchi Cui, B.D., Nan Li, Amit Misra, *Fracture Resistance of Hierarchical Cu-Mo Nanocomposite Thin Film.* Submitted to Materials Science and Engineering: A, 2020.

Chapter 2 Background

2.1 Achieving high strength in metallic materials

Achieving high strength has always been a major goal for developing structural materials. With advances in nano-structured and glassy materials, the race for stronger and tougher metals has been brought up to a new level. Three popular approaches include fabricating metallic glasses, nanocrystalline metals and metallic nanocomposites (MNC). Metallic glass is also called amorphous metal, where atoms are rather randomly packed with no long-range order [1]. Crystalline defects in conventional metals like dislocations thus cannot be found in these materials. As dislocation activities control the deformation of conventional crystalline metals, metallic glasses possess distinct mechanical properties. Strength of a metallic glass is normally three to four times higher than its crystalline counterpart. For instance, the strength of an Al-based amorphous alloy can reach as high as 1.5 GPa, whereas that of a conventional Al alloy is 200 - 300 MPa [2]. The metallic glasses deform through formation of shear bands, which inherently is a strain softening process and the shear bands tend to grow unidirectionally, leading to failure of the material [3]. Therefore, amorphous metals are typically low in ductility, limiting their applications. Similar scenario applies to nanocrystalline metals, which have average grain size and range of grain sizes smaller than 100 nm [4]. Based on Hall-Petch scaling law, the strength of a polycrystalline metal increases with decreasing grain size. This trend stops when grains are too small to accommodate dislocation activities and grain boundary sliding plays the leading role in deformation[5]. Shear band formation is associated with the grain movements as the grains tend

to slide in a collective manner. The result is localized strain and compromised ductility. MNC, on the other hand, have the potential to retain ductility through structural design and thus are the focus of this study.

MNC is generally defined as a solid multi-phase metallic material where the constituent phases have dimensions smaller than 100 nm[6]. These MNCs present significant advantages over conventional bulk metals, which include exceptionally high strength[7], good fatigue and radiation resistance[8-10] and thermal stability[11, 12]. Their size- and microstructure-dependent mechanical performances have drawn much attention from both scientific and practical views. With the rapid development of nanotechnology, different approaches have been attempted to synthesize MNCs, such as mechanical alloying[13, 14], nanoparticle sintering[15, 16], severe plastic deformation[17], physical vapor deposition[18], rapid solidification[19] and liquid metal dealloying[20]. Through these methods, both amorphous/crystalline and crystalline/crystalline MNCs can be fabricated. Vast amount of research has been focused on the amorphous/crystalline systems, where the second phase can be particulates[21, 22] or dendrites[23]. Amongst the crystalline/crystalline MNCs, the composites with layered morphology, referred to as nanoscale

Figure 2.1 Schematic showing structure of a MNLC. A and B represent two different metals.

metallic multilayers or metallic nanolaminates or metallic nanolayered composites [7, 24-26] have received significant attention. Here, we adopt the nomenclature of metallic nanolayered composites (MNLC). Figure 2.1 shows schematically the structure of an MNLC, where layers of two different metals are stacked together. While exhibiting ultra-high yield strengths, MNLCs suffer from plastic flow localization [7, 25]. An overview of the length-scale dependent mechanical behavior of MNLCs is presented in the following sections.

2.2 Metallic nanolayered composites (MNLC)

MNLCs present extraordinary uniaxial strength compared to the constituent metals in bulk form [7, 27-30]. For example, bulk Cu (grain size of 80 μm) and Nb (grain size of 32 μm) have yield strengths at about 70 MPa and 200 MPa respectively [31, 32]. When the two metals were made into stacking layers with thickness of a few nanometers, the strength reached over 2.6 GPa [7]. As a simplified structure, the multilayer geometry provides a model system for studying the flow behavior of MNCs. It has been found that the high strength of MNLC is related to the interface structure between the layers.

2.2.1 Interface strengthening in MNLCs

The high strength of MNLCs results from the fact that the metal/metal interfaces are strong barriers for slip transmission. Based on the nature of the interfaces, the MNLCs can be generally categorized into two types: coherent systems and semi-coherent systems. The strengthening mechanisms in these systems are different. In **coherent systems** such as Cu(FCC)/Ni(FCC) [33], the two metals have the same crystal structure and a small lattice parameter mismatch (typically below 5%) such that epitaxy is established and the slip systems across the interface are contiguous. The coherent interfaces are thus structurally “transparent” to dislocation slip [34]. However, there is still a resistance to the dislocation to move from one layer to the next primarily due to the

interfacial coherency stress. In order to match the lattice parameters, alternating compression-to-tension elastic coherency strains develop in the multilayer structure that can lead to significant coherency stresses. For example, the coherency stress in a Cu/Ni multilayer with equal thickness of the two layers (2.7% mismatch) is calculated to be 2.2 GPa [34]. This value is comparable to the maximum strength of 1.7 GPa measured in a Cu/Ni MNLC but slightly higher because the calculation is based on the assumption of perfect coherency. Misfit dislocations exist at the interface, according to the estimates of Frank and van der Merwe [35], that relax the coherency stress.

In the case of **semi-coherent** interfaces across two metals of the same structure, misfit dislocations play an important role in affecting the dislocation transmission across interfaces. Simulation of Cu/Ag (12% mismatch) interface shows that the cores of misfit dislocations are spread in the interface plane and completely overlap.[36] As a result, the coherency stress is relieved and the interface acts as barrier to slip mainly because of the misfit dislocation network. The maximum strength of a Cu/Ag MNLC was measured at 1.5 GPa, lower than that of a Cu/Ni system [27]. For **semi-coherent interfaces in FCC/BCC systems**, e.g. Cu/Nb [37], the slip systems are not continuous across the interface because of the change in crystal structure. Therefore, even though there is no coherency stress, these interfaces pose barrier to dislocation slip due to structural discontinuity and are called “opaque” interfaces [34]. A key factor that determines the resistance to slip transmission of an “opaque” interface is its shear strength, which is defined as the critical shear stress at which one layer slides with respect to the other along the interface plane. When the interface is weak in shear, the stress field of a glide dislocation approaching the interface would locally shear the interface. In consequence the glide dislocation is attracted to the interface and absorbed by it in the form of core spreading along the interface

plane [38, 39]. Exceptionally high applied stress is required to re-nucleate a glide dislocation at the other side of the interface to complete the transmission. Cu/Nb interface was found to be weak in shear and the yield strength of a Cu/Nb MNLC under applied stress normal or parallel to the layers can be as high as 2.6 GPa [7]. In comparison, multilayer with interfaces that are stronger in shear have lower yield strength, e.g. Al/Nb at 1.8 GPa [29].

2.2.2 Length-scale-dependent deformation mechanisms of MNLCs

In general, the measured strength of an MNLC increases with decreasing individual layer thickness from micrometer to nanometer scale, until a peak strength is achieved at thicknesses down to a few nanometers. This trend is shown in Figure 2.2, where the hardness data are plotted against inverse square root of the layer thickness λ for a few metallic multilayers [34]. Three kinds of models for dislocation motion have been proposed to explain this size dependent strength for fcc/bcc semi-coherent systems such as Cu/Nb, which is summarized in Figure 2.3 [40]. The first

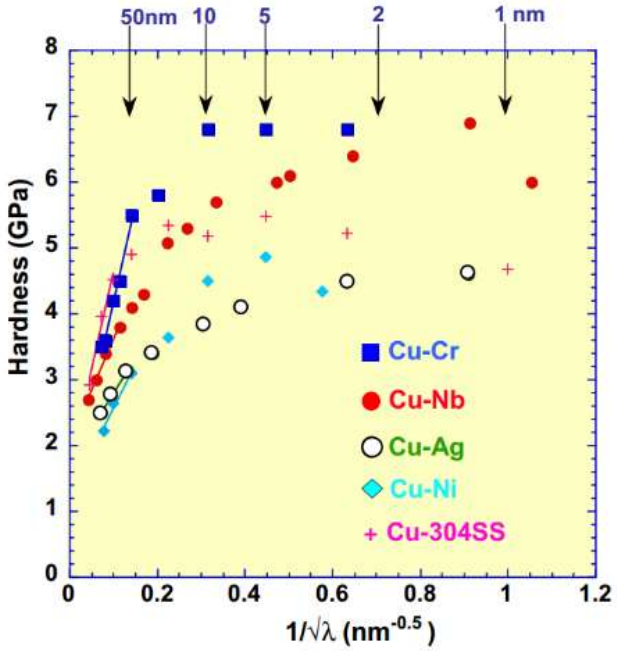

Figure 2.2 Plot of hardness as a function of inverse square root of layer thickness in several Cu-based MNLCs. [34]

model is based on the Hall-Petch scaling law, where the yield strength σ is related to the layer thickness h as $\sigma \propto h^{-1/2}$. This corresponds to the linear portion of the plots in Figure 2.2 and generally applies to systems with larger individual layer thickness, where dislocation pile-ups can be accommodated. The pile-up may lead to flow localization, when the stress concentration is large enough to shear the interface [7, 41]. The individual layer thickness for this model is typically in the sub-micrometer to micrometer regime. As h is lowered, fewer dislocations can reside in a pile-up due to the repulsion between the strain fields of dislocations, until only one dislocation is allowed when h is a few tens of nanometers. If the flow stress of this one dislocation is lower than the interface strength, the confined layer slip (CLS) deformation mechanism becomes dominant. During CLS, single dislocation loops are pinned by two interfaces and glide in individual layers [42, 43]. It has been shown that the required shear stress to propagate a glide loop in CLS regime increases with decreasing layer thickness. In a typical Cu/X system, where X is another metal, the CLS takes control at layer thickness of a few nanometers to a few tens of nanometers. When the

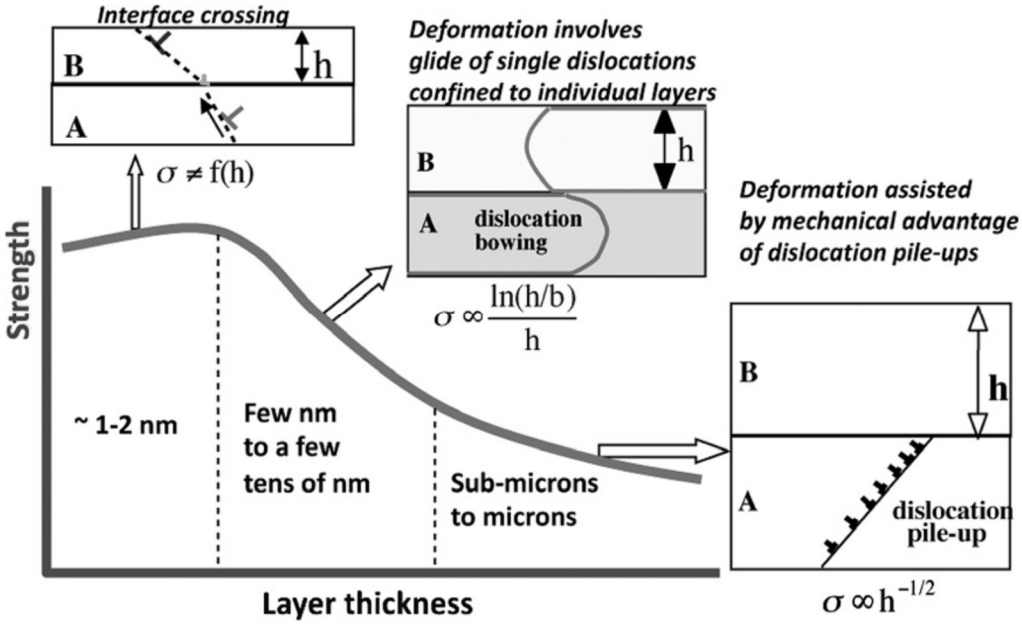

Figure 2.3 Schematic illustration of the key unit processes that determine the yield mechanism in LMC [40].

CLS stress surpasses the stress needed for a dislocation to cross the interface, glide dislocations are no longer confined by bounding interfaces. In this regime, dislocations move by transmitting through the interface and the peak strength of a MNLC as shown is Figure 2.3 is determined by the stress required for this transmission. Molecular dynamics simulations have also shown that the interface barrier to slip transmission decreases as the layer thickness approaches the dislocation core dimension [34]. This explains the drop in strength observed in some systems such as Cu-Ni as the layer thickness is reduced below approximately 1 nm.

2.2.3 Modes for shear band formation in MNLCs

Like many other materials with high hardness, MNLC suffer from low ductility due to flow localization or the formation of shear bands post yield [44]. The mechanism for shear band formation in a MNLC can be quite different according to the interface properties. For coherent systems with interfaces that are strong in shear, like Al/Al_3Sc, strain softening at small layer thickness is observed [45]. It was proposed that once the dislocation starts to shear through the layers, the stress to continue shearing on the same glide plane will be lower than initiating shear at a different location. Consequently, a shear band forms, which is demonstrated schematically in Figure 2.4a. As an edge dislocation with Burgers vector *b* glides across a coherent interface, a step would be created. As a result, after a dislocation glides through an Al_3Sc layer, two half-layers on opposite sides of the slip plane would offset by a distance of *b*. With continuous dislocation slip on the same plane, the Al_3Sc layer will eventually break off, leaving a channel of softer Al. This Al channel leads to softening of the composite. The transmission electron microscopy (TEM) image in Figure 2.4b shows the shear band in Al/Al_3Sc MNLC [46].

In a non-isostructural system, where the interface is “opaque” to dislocation slip, shear may form through two different processes, namely layer rotation and dislocation cutting. In the case of an

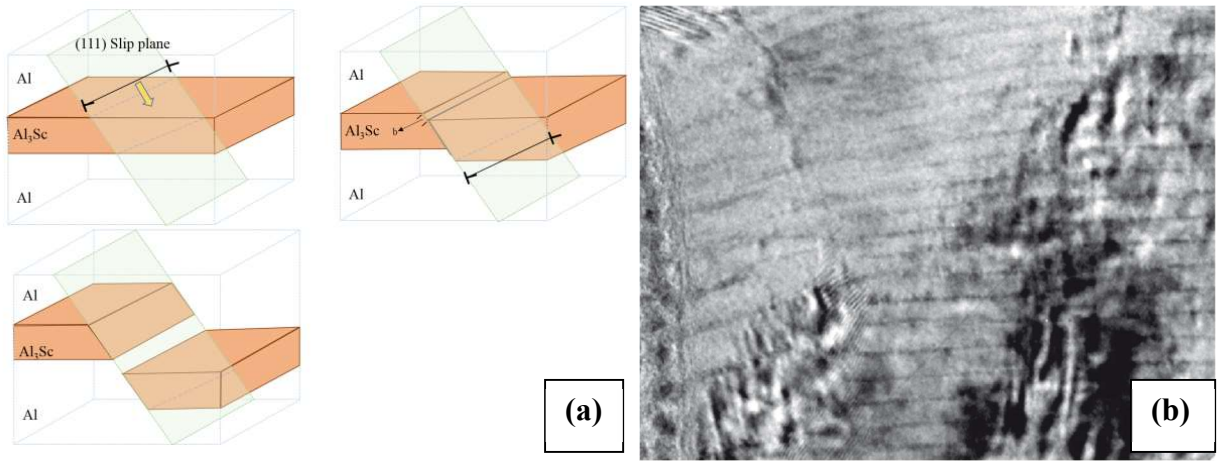

Figure 2.4 (a) Schematic illustration of shear banding in coherent MNLC, (b) TEM image showing rotation and shearing at the corner of Al/Al_3Sc pillar [46].

interface that is opaque to dislocations and weak in shear, like in Cu/Nb [37] or Cu/Zr [42], the interface acts as a dislocation sink and core spreading at the interface happens easily. When a localized stress causes unbalanced slip activity in a layer, rotation of interface plane normal occurs. The rotation will bring sufficient resolved shear stress on the interface to facilitate the relatively easier interfacial shear. In this way, the strain is localized in the inclined interface plane, resulting in shear banding and softening (Figure 2.5) [33, 37]. However, if the semi-coherent interface has limited dislocation absorption and high shear strength, it would act as a less effective barrier to slip transmission. For example, in 50 nm Al/Nb composite, the negative heat of mixing of the two metals result in an interface that is stronger in shear [29]. The localized shear as shown in Figure 2.6 is proposed to be a consequence of the dislocation transmission, similar to the case of coherent systems. However, the slip transmission in a semi-coherent system is different in a way that the slip planes in the two metals are not parallel to each other. For example, in a FCC/BCC system with Kurdjumov-Sachs (KS) orientation ($\{111\}_{FCC}//\{110\}_{BCC}$ and $<1\bar{1}0>_{FCC}//<1\bar{1}1>_{BCC}$), there exists a geometry that the intersections of the BCC and the FCC glide planes with the interface

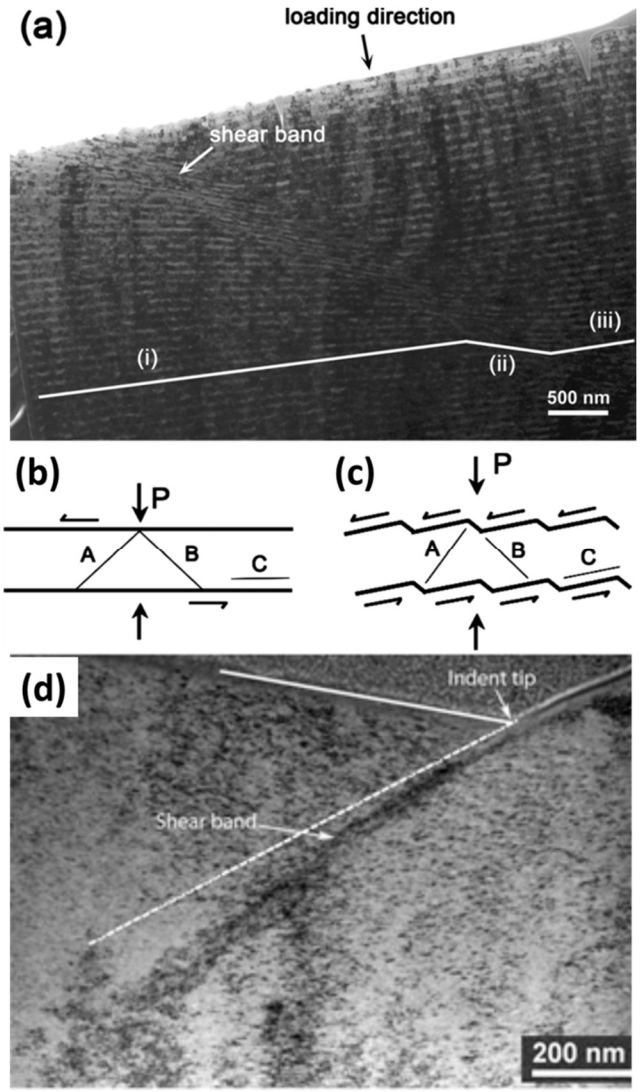

Figure 2.5 (a) TEM image showing shear band in Cu/Nb MNLC, (b) schematic illustration of dislocation movement under uniaxial loading, (c) non-uniaxial loading where interface rotate to shear orientation and (d) TEM image showing shear band in 5 nm Cu/Nb MNLC after nanoindentation [37].

coincide. Otherwise if the traces are non-parallel, dislocation climb within the interface is required to accomplish the transmission, which is unlikely to occur in the absence of thermal activation.

Through studying the Cu/X (X=Zr,Cr) systems, J.Y. Zhang *et al*. developed a deformation map that relates the two shearing mode, under applied compression normal to the interface of a semi-coherent MNLC to the thickness of individual layer [47]. Besides shear band formation, they

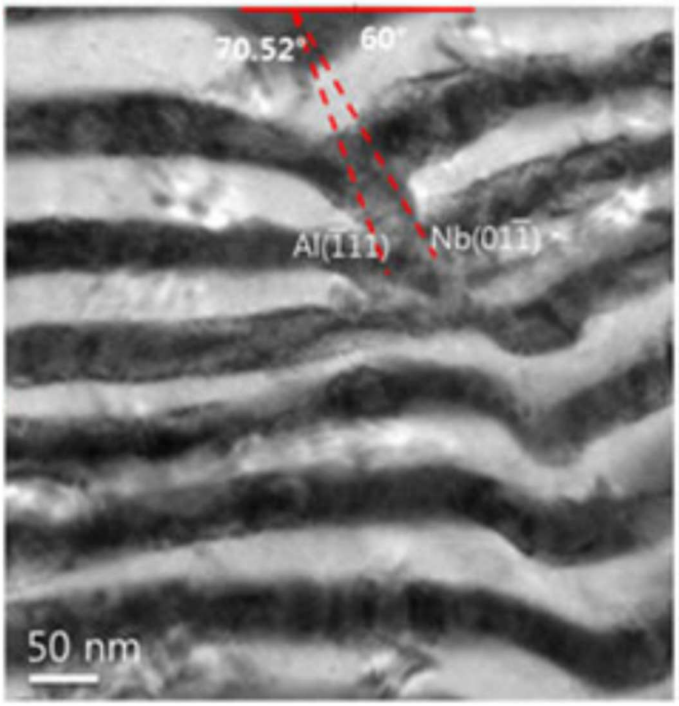

Figure 2.6 Cross-sectional bright-field TEM image showing region of macroshear in 50 nm Al/Nb MNLC [29].

also put the extrusion of the softer material (show in Figure 2.7) into consideration. Four parameters are used to describe their framework, namely the shear stress σ_{Shear}, the normal stress σ_{Normal}, the interface misfit dislocation barrier σ_{Edge} and the interfacial strength σ_{IBS}. The maps for the Cu/Zr and Cu/Cr multilayers can be found in Figure 2.8. The dislocation motion then depends on σ_{Edge} and σ_{IBS}. If $\sigma_{Edge} > \sigma_{IBS}$, dislocations will cut across the interface. Otherwise their motion will be limited in the individual layers. Besides the condition for extrusion of the softer Cu is $\sigma_{Edge} < \sigma_{Shear}$. Therefore, in RI (as shown in Figure 2.8) interface cutting by dislocations occurs and leads to localized shear. In RII where $\sigma_{Edge} > \sigma_{Shear}$ and $\sigma_{Normal} < \sigma_{IBS}$ the layers co-deform and local stress concentration promotes the rotation of the interfaces which leads to shear banding. In RIII, $\sigma_{Edge} < \sigma_{Shear}$ and $\sigma_{Normal} < \sigma_{IBS}$, which means that extrusion and layer rotation take place

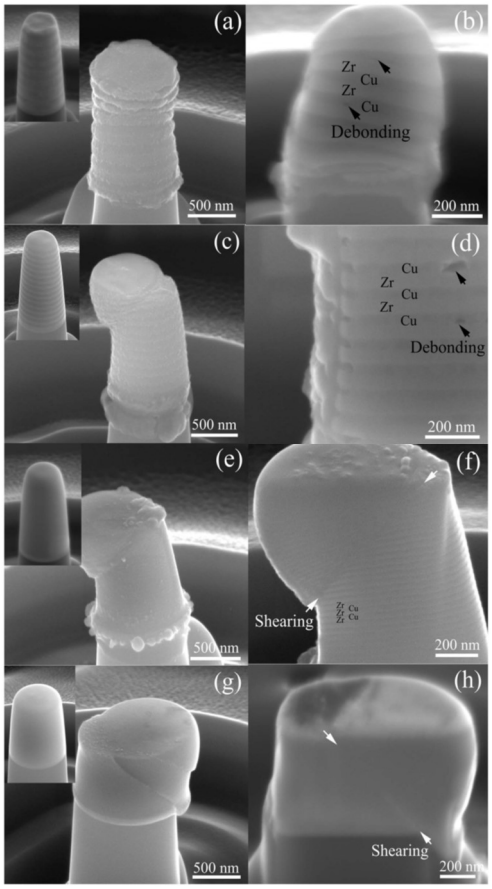

Figure 2.7 SEM image showing (a, b) h=100 nm and (c, d) h=50 nm micropillars (e, f) h=20 nm micropillars showing shear deformation and co-deformation; (g, h) h=5 nm micropillars showing highly localized shear banding by interface crossing [47].

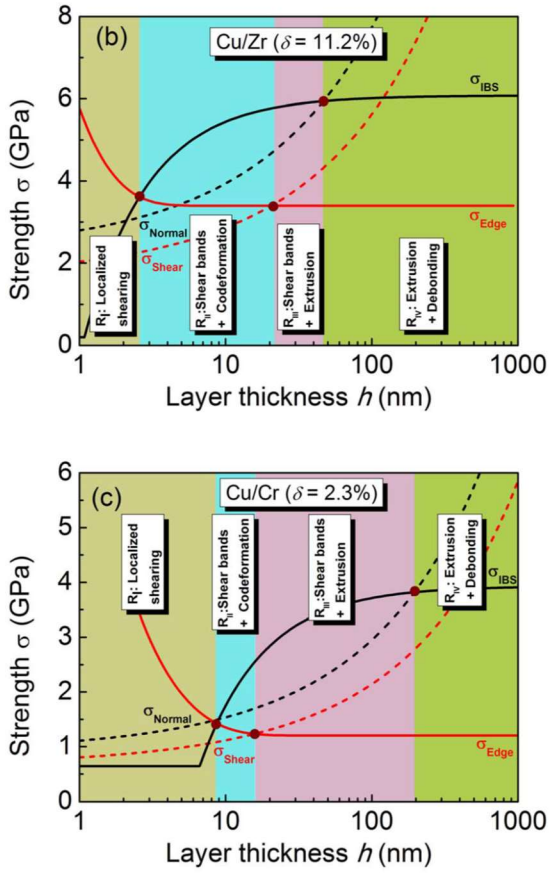

Figure 2.8 Deformation map for Cu/Zr and Cu/Cr systems [47].

simultaneously, leading to barreling of the compression sample as well as shear band. In RIV, $\sigma_{Normal} > \sigma_{IBS}$, indicating debonding at the interface (Figure 2.7). The Cu/Zr and Cu/Cr are FCC/HCP system with 11.2% misfit and FCC/BCC system with 2.3% misfit respectively. Their maps can be used as guidelines for similar MNLCs.

Apart from the dislocation-controlled deformation described above, grain boundary would also mediate the formation of shear band. Nano-indentation on 25 nm Au/Cu multilayers revealed that a buckling-assisted **grain boundary (GB) sliding** model could explain the shear band

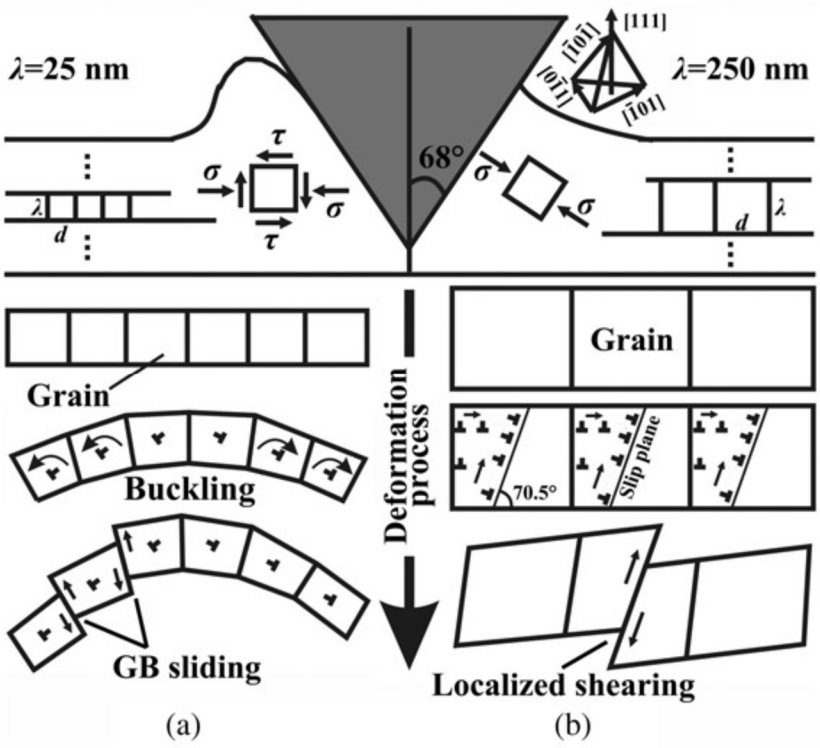

Figure 2.9 Schematic illustration of (a) buckling-assisted GB sliding of the 25 nm Au/Cu multilayer and (b) dislocation plasticity-dominated shearing of the 250 nm multilayer [28].

generation under sharp tip indentation [14, 28]. As illustrated in Figure 2.9, layers on one side of the indenter would co-deform to buckle toward the out-of-plane direction. Due to the buckling-induced lattice or grain rotation, the GBs originally parallel to the stress direction become inclined and start to bear resolved shear stress. This "soft" orientation of the grains leads to grain sliding and localized shearing (Figure 2.10). Large plastic strain is accommodated by the shear band in the soft buckling zone. Similar scenario was also found in the Al/Pb system [48]. Compression on the Al/Pb nano-pillars with 80 nm bilayer thickness showed that the pillars deformed with Al layer bending and extrusion whereas the deformed 2 nm bilayer thickness pillars had no extrusion but shearing. Both of the behaviors were observed in the 20 nm pillars. (Figure 2.10) By comparing the selected area diffraction (SAD) patterns, it was noticed that after deformation the degree of texture randomization is higher for the 20 nm pillar than that for the 80 nm pillar. This indicates

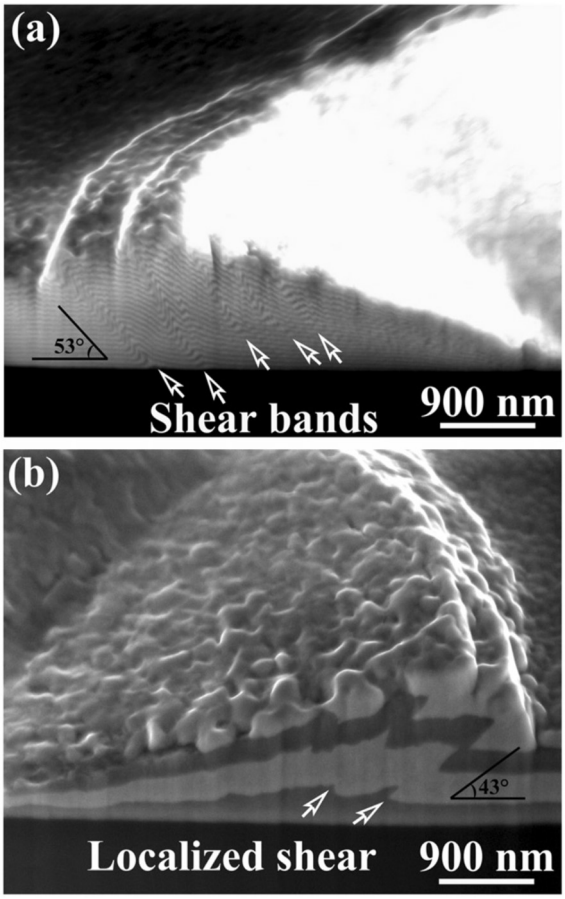

Figure 2.10 SEM images showing the deformation in (a) 25 nm Au/Cu multilayer and (b) 250 nm multilayer [28].

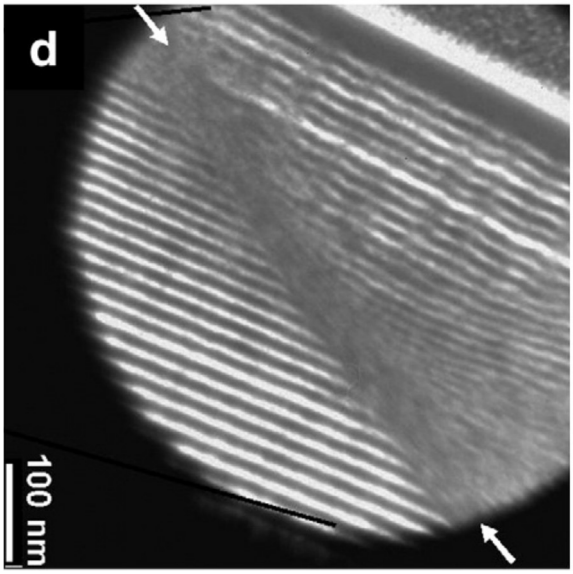

Figure 2.11 TEM images of the λ=20 nm Al/Pb pillar showing bending of individual layers and shearing [48].

that the deformation mechanism changed from dislocation activities to grain rotation as the layer thickness was reduced. This transition will occur when the stress required for dislocation motion/formation becomes larger than that for GB sliding [5]. It was proposed that the grain rotation leads to the formation of an array of coplanar GBs which cause long-rang sliding or partial shear.

2.3 Strategies to prevent flow localization

2.3.1 Increasing strain hardening rate

The Considere's criterion [49] states that the strain hardening rate should exceed the flow stress of the material to sustain uniform plastic flow in uniaxial tension, which can be written as:

$$\frac{d\sigma}{d\epsilon} > \sigma \tag{1}$$

where σ and ϵ represent the true stress and true strain respectively; and $\frac{d\sigma}{d\epsilon}$ is the strain hardening rate. Figure 2.12 plots the stress-strain curve of a typical tensile test with a superimposed strain hardening rate curve. The intersection of the two curves determines the starting point of necking and the ductility of the material. For a stronger material, the stress-strain curve would be elevated, intercepting with the hardening rate curve at lower strain. Therefore, a high strain hardening rate is required to retain ductility of a high strength MNC.

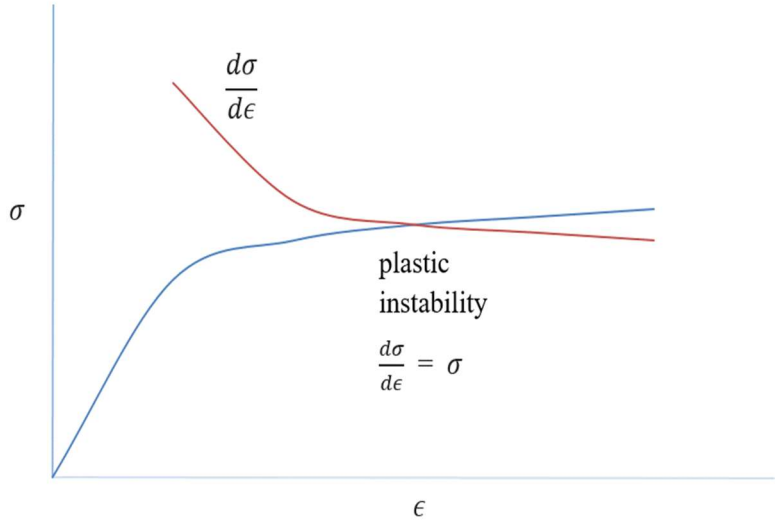

Figure 2.12 Stress-strain plot showing Considere's criterion for necking.

2.3.2 Flow delocalization in MNCs

Another strategy to prevent flow localization, which is to introduce a strain hardening phase, has been deployed in metal composites where the matrix is amorphous or nanocrystalline. Monolithic bulk metallic glasses are known to deform plastically by shear banding. Under unconstrained loading, only limited amount of shear bands can be activated at room temperature. Consequently, the plastic strain is highly localized, which leads to catastrophic failure. As a result, single phase metallic glasses typically have very limited plastic flow in compression (1-2%) and none in tension at room temperature [50]. As an approach to improve the mechanical performance of brittle metallic glasses, attempts of introducing crystalline phases into the microstructure have been made. Substantial increase in ductility has been observed in such composites [51, 52]. For example, C. C. Hays *et al*. fabricated a material with metal glass matrix and 25 vol% crystalline dendrite reinforcement phases, as shown in Figure 2.13. After a compression test over 8% total strain was achieved in the composite prior to failure, much higher than the values for monolithic

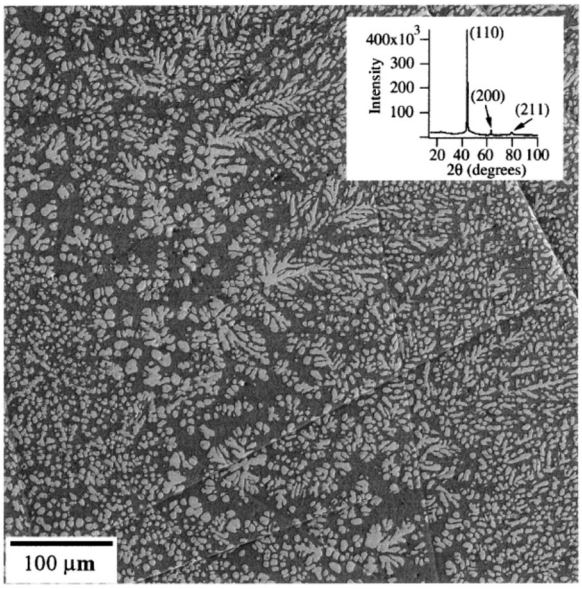

Figure 2.13 SEM backscattered electron image of *in situ* composite microstructure. (inset: X-ray diffraction pattern for the composite) [18].

metallic glass samples (<1%), where only 1 to 3 shear bands are activated. Figure 2.14 shows the shear band pattern after a bending test. The shear bands are regularly distributed throughout the region, with a spacing that coincides with the secondary arm spacing of the dendrites. It was proposed that the strain hardening crystalline phases act as seeds to the initiation of organized shear patterns and confine the propagation of individual shear bands.

Similar result was also found in nanocrystalline matrix composites. Single phase nanocrystalline metals lack strain hardening analogous to metallic glasses [53]. G. He et al. synthesized a composite that is composed of a dendrite phase dispersed in a nanocrystalline matrix [54]. The material was found to deform through shear banding in the matrix and dislocations in the dendrites. 14.5% plastic strain was recorded for one of their composites. This high ductility

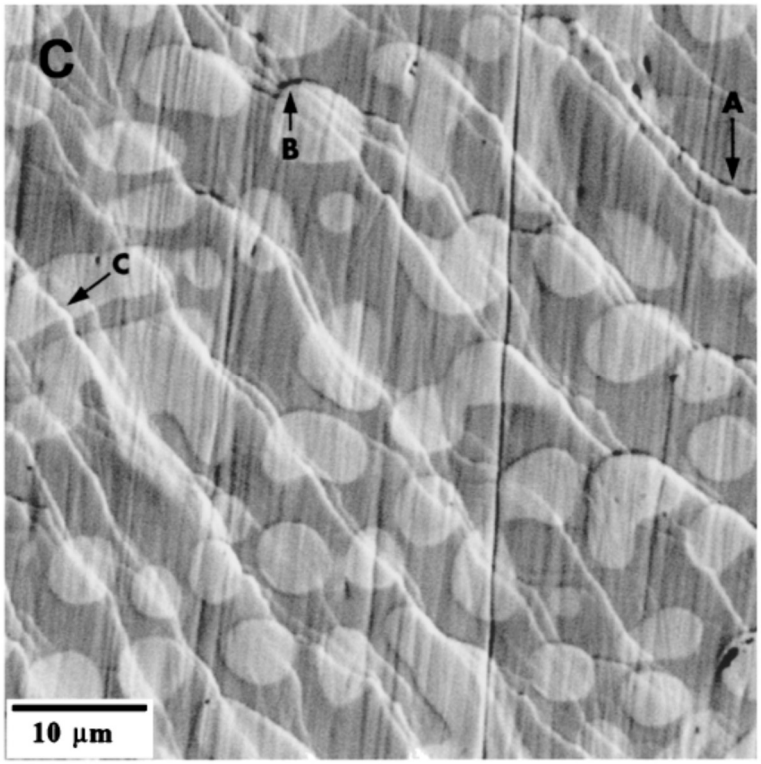

Figure 2.14 SEM image showing shear band pattern array from compressive failure region of bend test specimen [18].

was attributed to the assumption that the dispersed dendrites separate and restrict the shear banding to small regions, without propagating through the whole sample.

Retained ductility has been reported in some bicontinuous systems. McCue *et al*. succeeded in making the first bicontinuous metallic nanocomposite, as shown in Figure 2.15 [20]. Their approach was liquid metal dealloying, where one element in an alloy was dissolved by a molten metal while the other element was immiscible to the solvent metal. The ligament width can be controlled from tens of microns to approximately 70 nm. At ligament size of 70 nm, stress as high as 2.5 GPa was measured, while still retaining ductile behavior.

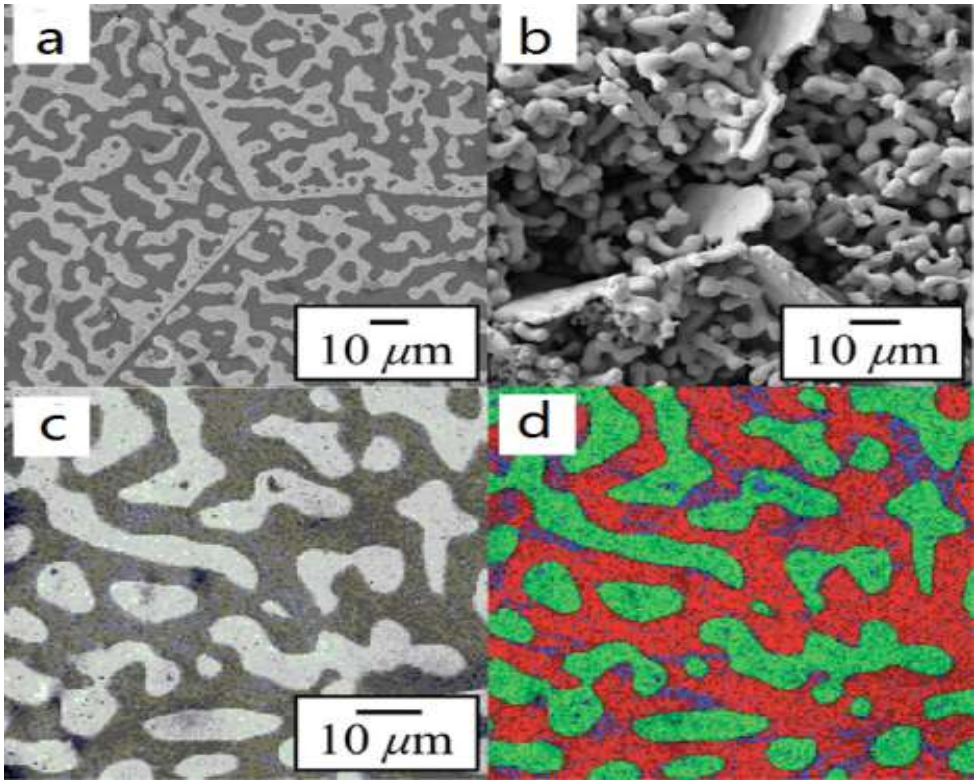

Figure 2.15 (a) SEM micrograph of a Ta–Cu composite; (b) SEM micrograph of the composite with Cu dissolved away; (c) SEM micrograph of a composite with a 5μm ligament size. (d) Elemental mapping overlay of (c): green is Ta, red is Cu, and blue is residual Ti in Cu-rich phase [20].

2.4 Measurements of hardness and elastic modulus using nanoindentation

Over the last few decades, nanoindentation has become a commonplace tool for characterizing mechanical properties in submicron scale. From the methodology developed by W.C. Oliver and G.M. Pharr, hardness and elastic modulus of a material can be obtained from load-displacement measurements, which is the goal for majority of the indentation tests [55, 56]. During the test, an indenter with tip radius of typically around 100 nm is pressed into the sample surface until the target load is reached. The load is then subtracted for the relaxation of the sample. The load and displacement data are continuously recorded during the process. The common shapes of an indenter tip include spherical, conical, Vickers and Berkovich, as illustrated in Figure 2.16 [57]. The angle θ measures the angle between the side of the indenter and the axis of loading. Figure 2.17 shows the typical surface profiles of a sample under maximum load and after indenter withdrawal. The parameters are defined as the following: P is the applied load, h is the total displacement, h_c is the contact depth, h_s is the displacement of the surface at the perimeter of the contact and a is the radius of contact. After load withdrawal the residual indentation depth is designated as h_f. Based on Oliver and Pharr's work [55], the hardness of the sample is calculated

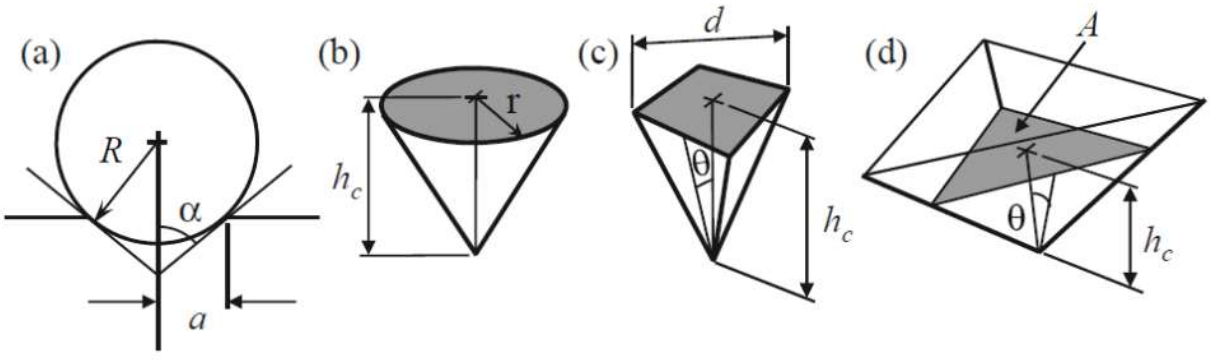

Figure 2.16 Schematics showing geometry of the indenter tips (a) spherical, (b) conical, (c) Vickers and (d) Berkovich [57].

as

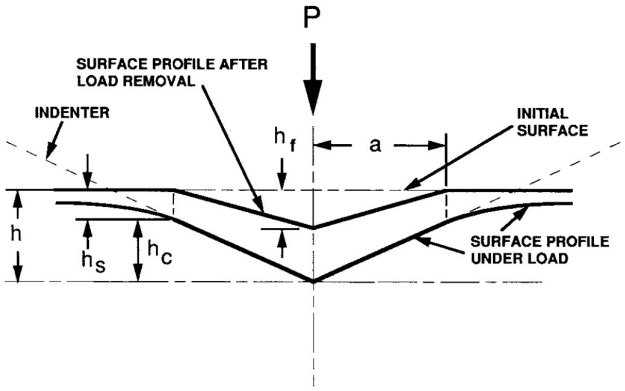

Figure 2.17 A schematic representation of a section through an indentation [56].

$$H = \frac{Pmax}{A} \tag{2}$$

where P_{max} is the peak load and A is the projected area of the hardness impression. In nanoindentation, where the impression size is below the resolution of an optical microscope, the value of A at the peak load is usually calculated from indenter geometry and the contact depth h_c. As the indenter, which is typically made of diamond, doesn't deform significantly and the indenter geometry is well defined as an area function F(h), A can be described as a function of h_c as

$$A=F(h_c) \tag{3}$$

For example, the projected area of contact for a perfect Berkovich tip is given by[57]

$$A=3\sqrt{3}h_c^2 tan^2\theta \tag{4}$$

At $\theta = 65.27^o$,

$$A = 24.5\ h_c^2 \tag{5}$$

However, the indenter tip cannot be fabricated to the exact profile and it is blunted during service, the area function needs to be calibrated before experiments. It is normally calculated from indentation data on standard samples like fused quartz. The h_c value can be calculated as

$$h_c = h_{max} - h_s \tag{6}$$

where

$$h_s = \varepsilon \frac{P_{max}}{S} \tag{7}$$

and ε is a constant dependent on the geometry of the indenter. An example of load-displacement curve is shown in Figure 2.18. The experimentally measured stiffness, S, can be calculated as the slope of the upper portion of the unloading curve. The reduced modulus E_r can then be related to S as

$$E_r = \frac{S\sqrt{\pi}}{2\sqrt{A}} \tag{8}$$

The Young's modulus of the sample is related to E_r as

$$\frac{1}{E_r} = \frac{(1-\nu^2)}{E} + \frac{(1-\nu_i^2)}{E_i} \tag{9}$$

where v is the Poisson's ratio for the sample and i denotes the parameters for the indenter. As the indenter is made from known material, the modulus of the sample can thus be derived. For a commonly used diamond tip, E_i =1140 GPa and ν_i = 0.07. During each test, a load hold period

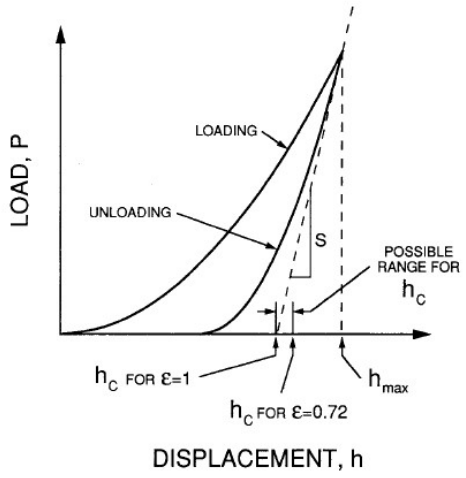

Figure 2.18 A schematic representation of load versus indenter displacement curve [56].

should be included between loading and unloading processes. Otherwise creep during the unloading would cause the slope of the upper portion of the unloading curve to be abnormally high.

2.5 *In situ* nanomechanics in transmission electron microscope (TEM)

The dynamics of dislocations, and their interactions with each other and with the grain boundaries and interfaces are difficult to discern in *post-mortem* microstructural characterization. *In situ* nanomechanics in transmission electron microscope (TEM) is an effective approach to such observations. Further, in nanostructured metallic materials, the corresponding changes under straining are sometimes best discerned using *in situ* TEM due to the small feature size. The establishment of *in situ* straining stages in TEM dates back to 1950s [58]. Over the years, *in situ* straining holders with the extended capability of load-displacement measurement (in which the load resolution can reach nanoNewton), temperature up to 1000 °C, atomic scale straining control and coupling with irradiation environments have been developed. Details on the instrumentation of the stages have been reviewed by other articles and thus will be not elaborated here.[59-61]. Using these apparatus, observation of deformation events in metals such as dislocation slip [62, 63], deformation twinning [64-69], phase transformation [70-73], dislocation and grain boundary interactions [74-77], dislocation and radiation-induced defect interactions [78, 79] and grain boundary motion [80-84] have been achieved. In this session, the focus is on the application of TEM *in situ* straining in studying the deformation mechanisms of MNCs. It will be demonstrated that dislocation activities in MNCs with different length scales of interface spacings and crack propagation across the nano-sized phases can all be observed with the help of *in situ* techniques. Further, with the option of load-displacement measurement, mechanical parameters like interface shear strength and yield strength of the nanocomposites can be determined. An emphasis is placed

on the dislocation phenomena at heterophase interfaces in crystalline metal-metal systems, therefore, studies where one phase is metallic glass will not be discussed.

2.5.1 Deformation twin vs dislocation pile-up against interface

In MNCs with interface spacings above submicron scale, dislocation pile-up against the interface, with resemblance to pile-up against the grain boundary in bulk metals, is proposed to be the major strengthening mechanism. The ability of the interface to block dislocation transmission is thus crucial in determining the mechanical properties of an MNC. To explore how interface properties affect dislocation transmission, Eftink *et al*. performed *in situ* tensile experiments on CuAg samples where the Cu/Ag interface is either cube-on-cube or incoherent twin [85]. By water quenching or directional solidification, the bi-layer thickness of CuAg was controlled at a few hundreds of nanometers. It was found that the cube-on-cube interface is a weak barrier to twinning partial dislocation, while the incoherent twin type interface effectively prevents partial transmission. As shown in Figure 2.19a, the deformation twin originated in Ag layer has propagated through the interface to the Cu layer, generating a continuous twin. With increasing strain in Figure 2.19b, the deformation twin thickens to the same extent in both phases, indicating that additional partial dislocations must have been generated at the interface. On the contrary, partial crossing the interface was not observed at the incoherent twin interface. Instead partials in Ag were absorbed by the interface, followed by emission of a perfect dislocation in Cu (Figure 2.19c-e) and dislocation pile-up in Ag followed by cross-slip of dislocations with no slip transmission, dislocation absorption into the interface and emission back into the Ag layer (Figure 2.19f-h) was observed.

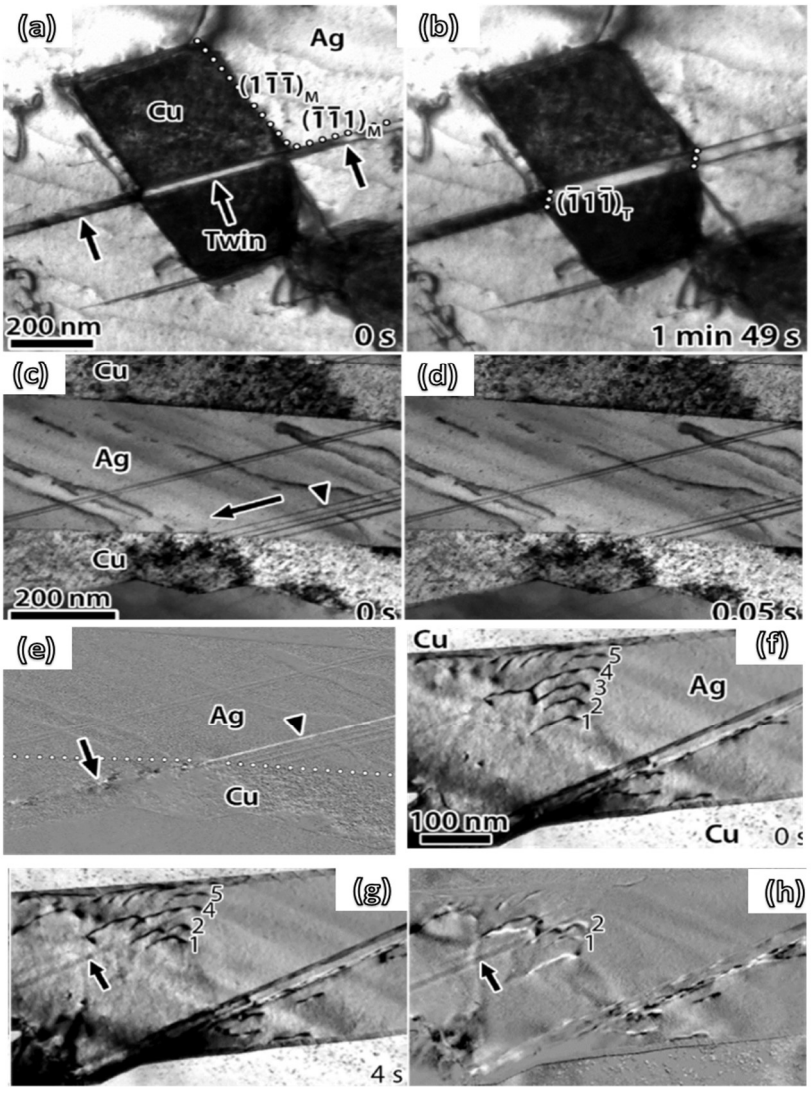

Figure 2.19 TEM images showing **(a)** continuous deformation twin across Cu/Ag interface, (**b)** thickening of the deformation twin in two phases, **(c)** generation of stacking faults in Ag with leading partials against the interface, (**d)** absorption of the leading and trailing partials by the interface, **(e)** emission of a perfect dislocation in Cu, **(f)** dislocation pile-up in Ag, **(g)** and **(h)** cross-slip of dislocations out of the pile-up and emission of dislocations back into Ag [85].

Molecular dynamics (MD) simulations were also conducted in this work to investigate dislocation-interface interactions at the two types of interfaces, which presented results in agreement with the *in situ* observation. At the cube-on-cube interface, the simulations showed transmission of twinning partial from Ag to Cu and rotation of the interface to transfer strain to the Cu layer, followed by thickening of the deformation twin by addition of mobile partial

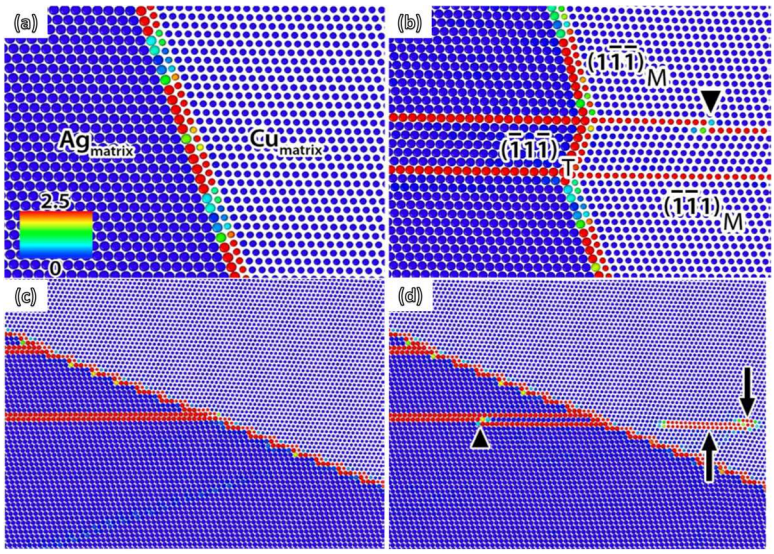

Figure 2.20**.** MD simulations showing **(a)** initial cube-on-cube AgCu interface, **(b)** partial dislocation transmitted from Ag to Cu and the twin thickened from the partial dislocation indicated by the arrowhead, **(c)** partial dislocation in Ag accommodated by the interface and **(d)** nucleation of a partial back into Ag and emission of two perfect dislocations in Cu.

dislocations (Figure 2.20a-b). When a partial dislocation in Ag encounters an incoherent twin Ag/Cu interface, it is first accommodated by the interfaces without emission of dislocation, followed by nucleation of a new partial with opposite Burgers vector back into Ag and emission of two perfect dislocations into Cu (Figure 2.20c-d).

From this work two general rules have been considered to predict dislocation-interface interaction behavior: (i) the geometric condition across the interface. This is described by the parameter $m' = \cos(\phi) \cdot \cos(\kappa)$, where ϕ is the angle between the slip plane normals and κ is the angle between the Burgers vectors of the incoming and outgoing dislocations. (ii) the magnitude of the Burgers vector of the residual interface dislocation, $|b_{res}|$. Dislocation transmission across the interfaces would be favored with a maximization of m' and a minimization of $|b_{res}|$.

2.5.2 Dislocation confined layer slip mechanism

The breakdown of dislocation pile-up based Hall Petch model is typically inferred in multilayer MNCs when the layer thickness is in a few tens of nanometers, based on plots of measured hardness (or strength) as a function of √h [86, 87]. A CLS model constructed on earlier work of a similar mechanism in plastic yielding of thin films on substrates [88] was proposed to describe such deformation as glide of single Orowan-type dislocation loops bounded by the interfaces [89]. To directly observe CLS and elucidate deformation mechanism in MNLC when the feature size is of a few tens of nanometers, Li *et al*. performed *in situ* nanoindentation in TEM on quasi-single crystal Cu/Nb nanolayer films [90]. The bilayer thickness of the film was 50 nm, with individual layer thickness of 20 nm for Nb and 30 nm for Cu and a (110) Nb // (111) Cu // interface plane texture. As shown in Figure 2.21a to c, dislocation glide via CLS within the layers and nucleation of new dislocations were observed and ascribed as the dominant deformation mechanism in the material. Nucleation of dislocations at the Cu/Nb interface and emission of dislocation into the layer has also been observed, as demonstrated in Figure 2.21d and e. Interfaces were thus proposed to be the preferred nucleation sites for glide dislocations. Co-deformation of Cu and Nb nanolayers, which means simultaneous deformation of the two phases, was also observed without cracking to large plastic strains as shown in Figure 2.21f. This behavior is considered as indicative feature of CLS, which has been discovered in various multilayer systems such as Cu/Zr [42], Cu/Au and Cu/Cr [91]. No evidence of deformation twinning and dislocation transmission across the interface was encountered during the experiments.

2.5.3 Interface mediated deformation twinning mechanism

In accumulative roll-bonded (ARB) Cu/Nb MNLC that has a Nb{112} // Cu{112} interface with the Kurdjumov-Sachs orientation relationship, deformation twinning was observed, in

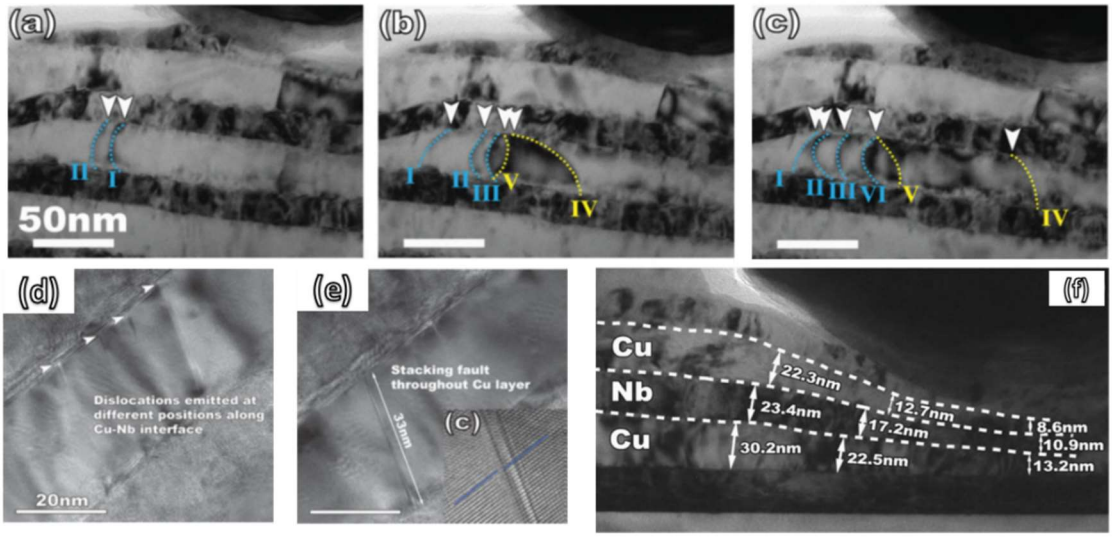

Figure 2.21 *In situ* TEM study on Cu/Nb multilayer showing (a)-(c) confined layer slip and formation of new dislocations, (d)-(e) dislocation emission from the interfaces and (f) co-deformation of the nanolayers.

contrast to the above mentioned system with {110} Nb // {111} Cu // interface plane, although the interface spacing is similar [92]. To study the dynamic process of deformation twinning, Zheng *et al*. performed *in situ* TEM nanoindentation on such a system with nominal individual layer thickness of 18 nm[93]. As shown in Figure 2.22a and b, partial dislocation 1 emitted into Cu layer after loading, forming a stacking fault, followed by emission of partial dislocation 2 approximately 10 nm apart and formation of the second stacking fault. With further loading, twin formed between the two stacking faults as shown in Figure 2.22c. The HRTEM image in Figure 2.22d further confirms the formation of twin and demonstrates the twinning relationship across the twin boundary. From the *in situ* work and atomic scale analysis of the Cu/Nb interface, deformation twinning in ARB Cu/Nb can be described as first nucleation and emission of twinning dislocations from dissociation of misfit dislocations at the interfaces, the consequent formation of stacking faults separated along the interface and the final nucleation and emission of twinning dislocations between the separated stacking faults.

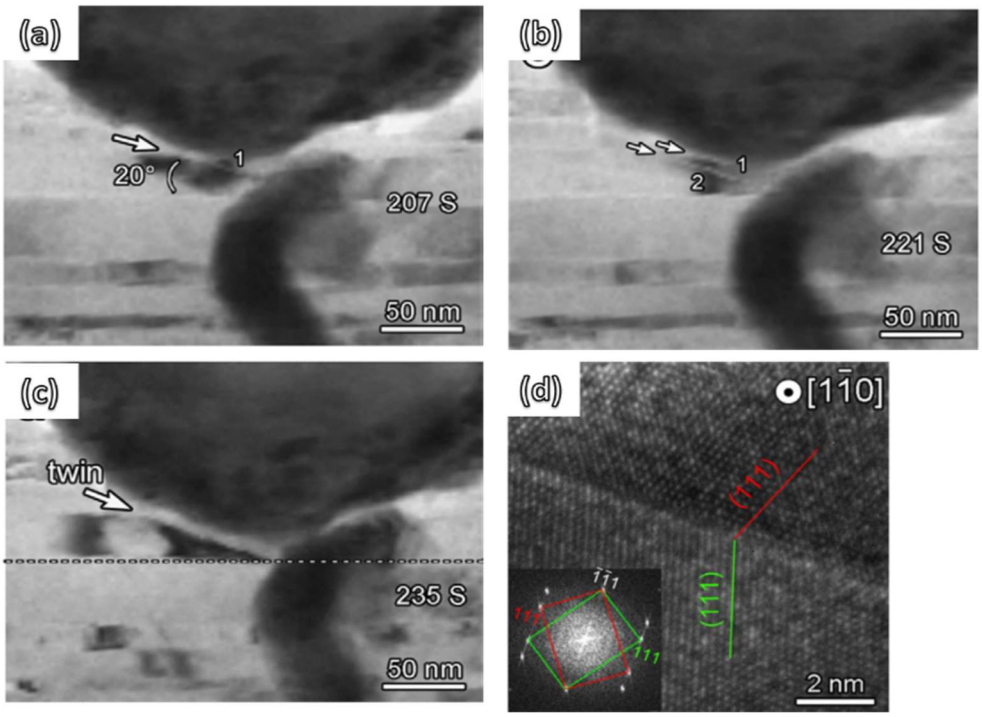

Figure 2.22(a)-(c) *In situ* TEM study on ARB process Cu/Nb multilayer showing formation of deformation twin from twin nuclei 1 and 2 and (d) HRTEM image at the twin boundary.

Nanotwinning has been shown to be an effective strengthening mechanism in metallic materials with improved ductility [94-96]. *In situ* straining in TEM gives information on the origin of twinning from interfacial misfit dislocations. With deeper understanding of the relationship between deformation twinning and the interface structure, twinning can be introduced to MNCs to improve their mechanical properties through interface design.

2.5.4 Room temperature dislocation climb at interfaces

When the interface spacing is reduced down to a few nm, dislocation transmission across the interface is proposed to be the major deformation mechanism in MNCs. At this length scale, observation of dislocation line in TEM becomes very difficult. Instead, high-resolution (HR)-TEM is a useful tool to study dislocations at atomic scale. When the indentation speed can be controlled below a few Å per second, *in situ* straining can be performed in high-resolution (HR)-TEM mode.

Li *et al*. conducted such experiments on Al/Nb multilayers with individual layer thickness of 5 nm with an indentation speed of 0.2 nm/s [97]. Snapshots at different instants during the tests in Figure 2.23 illustrate that two dislocations approached from a 2.5 nm distance to 1.7 nm and finally annihilated each other along the interface through climb, which is unexpected in bulk Al or Nb at room temperature and provides experimental support to the atomistic simulation showing that dislocations could effectively climb near and within interfaces and facilitate dislocation transmission [98]. A near perfect interface was left after the annihilation. Based on the frame rate, a lower bound of the climb velocity could be estimated at 0.4 nm/s, which is two orders of magnitude higher than the climb velocity of ~0.001 nm/s in bulk Al [99]. Enhanced diffusion of vacancies and higher vacancy concentration at the interface were proposed to attribute to the rapid climb of dislocations at the interface [98]. Through this work, dislocation trapping at the interface, pinning of partial dislocation at the interface that leads to the extension of stacking fault, and increase of dislocation density from ~10^{14} m^{-2} to ~10^{16} m^{-2} after indentation, which should account for the large magnitude of plastic deformation in crystals, were also observed. These observations

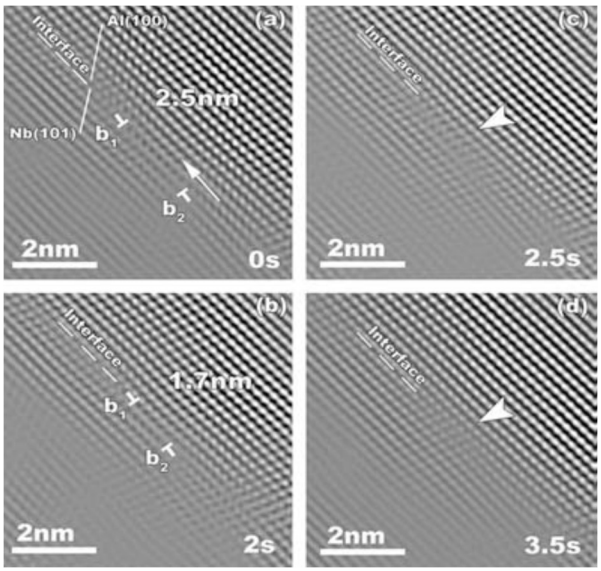

Figure 2.23 HRTEM snapshots showing dislocation climb and annihilation near Al/Nb interface.

that were not attainable from other approaches provide important insight into understanding the deformation mechanisms in MNCs at fine length scale.

2.5.5 Fracture mechanisms in multilayers

Besides tracing dislocation activities, investigation of the size and morphological evolutions of the nanosized phase is also enabled by *in situ* TEM technique. Besides the evolution in layer thickness as mentioned above, crack propagation can also be observed, which provides an opportunity to study fracture mechanisms *in situ* in MNLCs. Hattar *et al*. performed such experiment on multilayers of 65 nm Cu and 150 nm Nb by stretching the sample in TEM [100]. Four crack hindrance mechanisms were observed, namely microvoid formation (Figure 2.24a), crack deviation (Figure 2.24b), layer necking (Figure 2.24c), and crack blunting (Figure 2.24d). This work provided insight on the role of interfaces in impeding crack propagation. Coupling with the information gained from dislocation-interface interactions, deformation and fracture mechanisms of MNCs will be better understood.

In previous study, fracture mechanisms were only studied when the load is applied parallel to the interfaces. Liu *et al*. tested Cu/Nb multilayers in two loading orientations - parallel to the interfaces and also the perpendicular case.[101] Their material was prepared through ARB to achieve an average layer thickness of 63 nm. Under parallel loading, CLS in both Cu and Nb was observed, leading to nearly iso-strain co-deformation, until the onset of strain localization, which resulted in crack formation and propagation similar to Hattar's observations (Figure 2.24e). When the load is perpendicular to the interfaces, deformation rapidly localized in a thicker Cu layer, which is supposed to be softer. Failure of the specimen was followed as shown in Figure 2.24f, giving an apparent "brittle" behavior. Stress and strain values were measured during the test and showed that when the load is applied parallel to the interfaces, the Cu/Nb multilayers have both

higher strength and better deformability, owing to the ability of the interfaces to impede both dislocation glide and crack propagation.

2.5.6 Measurement of the shear strength of the interface

As mentioned in the previous example, *in situ* TEM sample holders not only serve to introduce strain to the sample, option of real-time load-displacement measurements is also

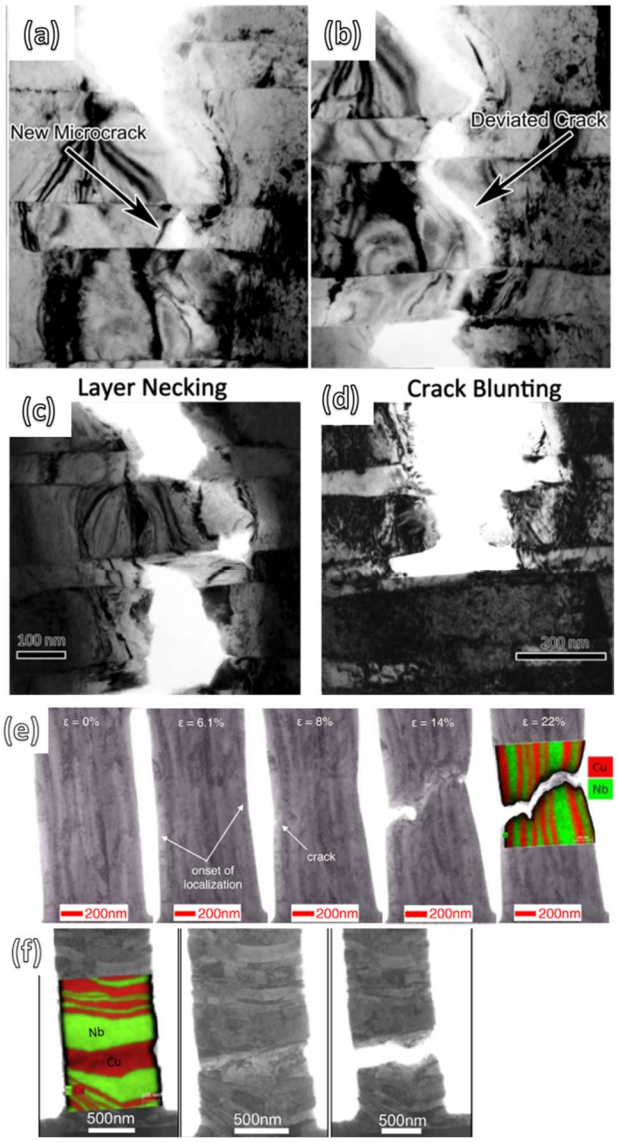

Figure 2.24 TEM images showing **(a)** formation of microcrack, **(b)** crack deviation, **(c)**layer necking and (**d)**crack blunting of 65 nm Cu/150 nm Nb MNC [100], and snapshots from the tensile test on 63 nm Cu/Nb when the load is **(e)** parallel to the interface and **(f)** perpendicular to the interfaces [101].

available. The stress and strain values can thus be calculated during a dynamic process and related to corresponding deformation events. One important mechanical parameter of an MNC is the shear strength of the interface, which can be defined as the critical shear stress at which one layer slides with respect to the other along the interface plane. Atomic simulations have shown that the ability of a semi-coherent interface to block dislocations is closely related to its shear strength.[38, 39] When the interface is weak in shear, the stress field of a glide dislocation approaching the interface would locally shear the interface. In consequence the glide dislocation is attracted to the interface and absorbed by it in the form of core spreading along the interface plane. Exceptionally high applied stress is required to re-nucleate a glide dislocation at the other side of the interface to complete the transmission. Although atomic simulations can give estimations on the interface shear strength, *in situ* nanopillar compression test offers a method to measure it directly, which is easily applicable to any metal systems. Li *et al*. fabricated nanopillars from Cu/Nb multilayers and shear loaded the pillar with the loading axis ~ 25° off the stage axis to measure the Cu/Nb interface strength [102]. Figure 2.25a presents the load/displacement data measured during the compression and Figure 2.25b to d are TEM image snapshots from the test, corresponding to points b to d in Figure 2.25a. The interfaces can be clearly resolved in the TEM images and thus sliding along the interfaces can be distinguished from shearing within the nanolayers. Interface sliding was observed from points c to d, from the load data and measured diameter of the pillar at the sliding interface, the shear strength of the interface could be measured at 0.3 GPa, which is lower than the shear strength of both metals and in good agreement with the atomistic simulations [40]. As a consequence, plastic deformation may be localized along the interfaces when there is enough

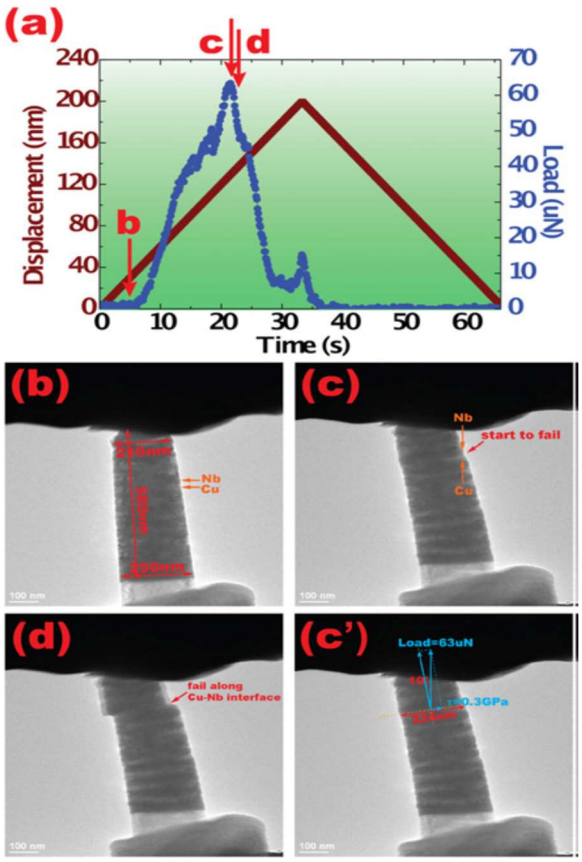

Figure 2.25 (a) Displacement and load data record during the test, point b to d correspond to images b to d, (b) to (d) *in situ* TEM study on Cu/Nb multilayer showing shearing at the interface.

resolved stress along the interface plane and leads to shear band formation and premature failure of the material [33, 37].

2.5.7 Phase transitions and grain activities

Phase transitions and grain activities can also be studied *in situ* [103-105]. As shown in Figure 2.26, J. Ye *et al*. studied compression on a nano-pillar of NiTi shape memory alloy [105]. From the diffraction patterns, it was clear that the pillar transformed from austenite cubic B2 phase to martensite B19' phase. From this *in situ* test, they confirmed the martensite transformation process and were able to measure the strain and stress required to initiate the transformation. Figure 2.27 shows gain rotation and coalescence observed in nanocrystalline Al under *in situ* indentation [106]. The appearance of the bright-contrast grain in Figure 2.27**b** indicated by the arrow implies that the grain rotates to a strong diffraction condition. In Figure 2.27**c** and **d,** it shows that the rotated grain grows as indentation proceeds. This work from M. Jin *et al*. provided strong evidence that grain boundary activity plays important role in the deformation of nanocrystalline metals.

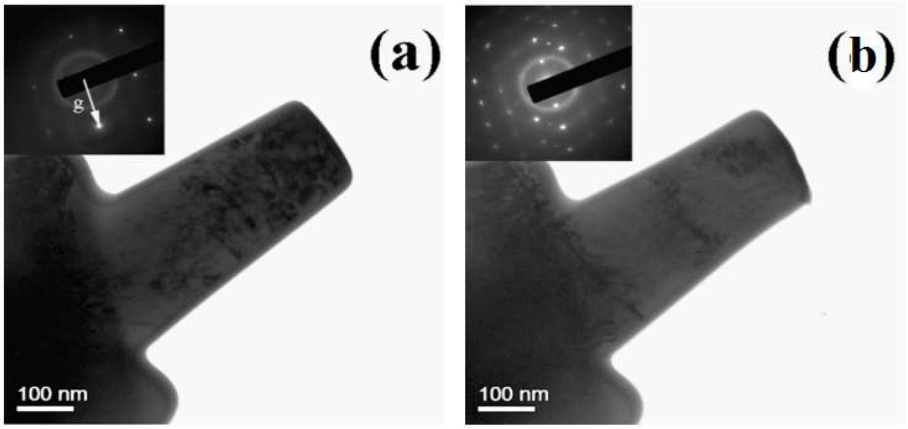

Figure 2.26 TEM image of the NiTi pillar (a) before the test. (b) after compressed for 20% engineering strain. Inset: diffraction patterns.

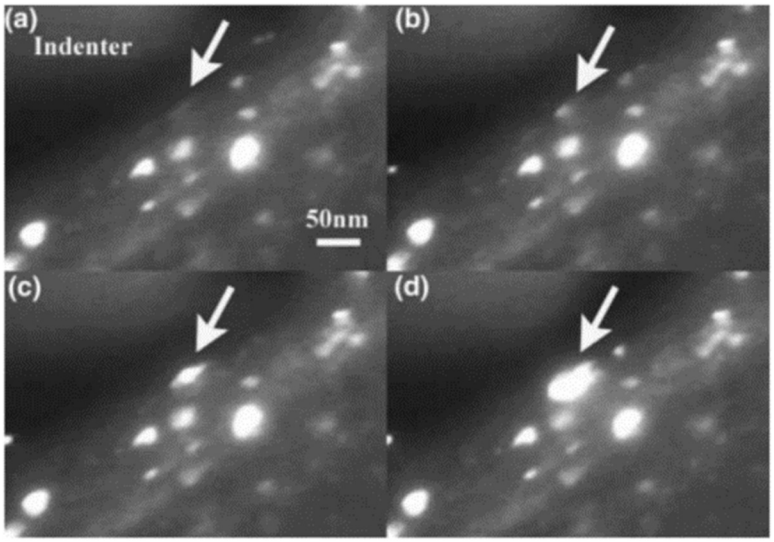

Figure 2.27 Sequential extracts from dark -filed TEM video recorded during *in situ* nanoindentation on nanocrystalline Al.

2.6 References

1. Johnson, W., *Bulk amorphous metal—An emerging engineering material.* Jom, 2002. **54**(3): p. 40-43.
2. Johnson, W.L., *Bulk amorphous metal—An emerging engineering material.* JOM. **54**(3): p. 40-43.
3. Schuh, C.A., T.C. Hufnagel, and U. Ramamurty, *Mechanical behavior of amorphous alloys.* Acta Materialia, 2007. **55**(12): p. 4067-4109.
4. Kumar, K.S., H. Van Swygenhoven, and S. Suresh, *Mechanical behavior of nanocrystalline metals and alloys1.* Acta Materialia, 2003. **51**(19): p. 5743-5774.
5. Hahn, H., P. Mondal, and K.A. Padmanabhan, *Plastic deformation of nanocrystalline materials.* Nanostructured Materials, 1997. **9**(1–8): p. 603-606.
6. Ajayan, P.M., L.S. Schadler, and P.V. Braun, *Nanocomposite science and technology*. 2006: John Wiley & Sons.
7. Misra, A., J. Hirth, and R. Hoagland, *Length-scale-dependent deformation mechanisms in incoherent metallic multilayered composites.* Acta materialia, 2005. **53**(18): p. 4817-4824.
8. Misra, A., Demkowicz, M. J., Zhang, X., & Hoagland, R. G., *The radiation damage tolerance of ultra-high strength nanolayered composites.* Jom, 2007. **59**(9): p. 62-65.
9. Hattar, K., Demkowicz, M. J., Misra, A., Robertson, I. M., & Hoagland, R. G., *Arrest of He bubble growth in Cu–Nb multilayer nanocomposites.* Scripta Materialia, 2008. **58**(7): p. 541-544.
10. Wang, Y.-C., A. Misra, and R. Hoagland, *Fatigue properties of nanoscale Cu/Nb multilayers.* Scripta materialia, 2006. **54**(9): p. 1593-1598.
11. Primorac, M. M., Abad, M. D., Hosemann, P., Kreuzeder, M., Maier, V., & Kiener, D. ., *Elevated temperature mechanical properties of novel ultra-fine grained Cu–Nb composites.* Materials Science and Engineering: A, 2015. **625**: p. 296-302.
12. Zheng, S., Beyerlein, I. J., Carpenter, J. S., Kang, K., Wang, J., Han, W., & Mara, N. A. , *High-strength and thermally stable bulk nanolayered composites due to twin-induced interfaces.* Nature communications, 2013. **4**: p. 1696.
13. Drbohlav, O. and A. Yavari, *Mechanical alloying and thermal decomposition of ferromagnetic nanocrystalline fcc-Cu 50 Fe 50.* Acta metallurgica et materialia, 1995. **43**(5): p. 1799-1809.
14. Liu, X., Zeng, M. Q., Ma, Y., & Zhu, M., *Melting behavior and the correlation of Sn distribution on hardness in a nanostructured Al–Sn alloy.* Materials Science and Engineering: A, 2009. **506**(1–2): p. 1-7.
15. Luechinger, N. A., Grass, R. N., Athanassiou, E. K., & Stark, W. J., *Bottom-up Fabrication of Metal/Metal Nanocomposites from Nanoparticles of Immiscible Metals.* Chemistry of Materials, 2010. **22**(1): p. 155-160.
16. *Sintering Behavior of Nanocrystalline Mo-Cu Composite Powders.*, *Sintering Behavior of Nanocrystalline Mo-Cu Composite Powders.* Rare Metal Materials and Engineering, 2009. **38**(10): p. 1693-1697.
17. Beyerlein, I.J., Mara, N.A., Carpenter, J.S., Nizolek, T., Mook, W.M., Wynn, T.A., McCabe, R.J., Mayeur, J.R., Kang, K., Zheng, S. and Wang, J., *Interface-driven microstructure development and ultra high strength of bulk nanostructured Cu-Nb multilayers fabricated by severe plastic deformation.* Journal of materials research, 2013. **28**(13): p. 1799-1812.
18. Vüllers, F. and R. Spolenak, *From solid solutions to fully phase separated interpenetrating networks in sputter deposited "immiscible" W–Cu thin films.* Acta Materialia, 2015. **99**: p.

213-227.
19. Chattopadhyay, K. and R. Goswami, *Melting and superheating of metals and alloys.* Progress in materials science, 1997. **42**(1): p. 287-300.
20. McCue, I., Ryan, S., Hemker, K., Xu, X., Li, N., Chen, M., & Erlebacher, J., *Size effects in the mechanical properties of bulk bicontinuous Ta/Cu nanocomposites made by liquid metal dealloying.* Advanced Engineering Materials, 2016. **18**(1): p. 46-50.
21. Hajlaoui, K., Yavari, A.R., LeMoulec, A., Botta, W.J., Vaughan, F.G., Das, J., Greer, A.L. and Kvick, Å., *Plasticity induced by nanoparticle dispersions in bulk metallic glasses.* Journal of non-crystalline solids, 2007. **353**(3): p. 327-331.
22. Saida, J., Setyawan, A. D. H., Kato, H., & Inoue, A. , *Nanoscale multistep shear band formation by deformation-induced nanocrystallization in Zr-Al-Ni-Pd bulk metallic glass.* Applied Physics Letters, 2005. **87**(15): p. 151907-151907.
23. Hays, C., C. Kim, and W.L. Johnson, *Microstructure controlled shear band pattern formation and enhanced plasticity of bulk metallic glasses containing in situ formed ductile phase dendrite dispersions.* Physical Review Letters, 2000. **84**(13): p. 2901.
24. Han, S.M., M.A. Phillips, and W.D. Nix, *Study of strain softening behavior of Al–Al 3 Sc multilayers using microcompression testing.* Acta Materialia, 2009. **57**(15): p. 4473-4490.
25. Li, Y., J. Tan, and G. Zhang, *Interface instability within shear bands in nanoscale Au/Cu multilayers.* Scripta Materialia, 2008. **59**(11): p. 1226-1229.
26. Wen, S. P., Zeng, F., Pan, F., & Nie, Z. R. , *The influence of grain morphology on indentation deformation characteristic of metallic nano-multilayers.* Materials Science and Engineering: A, 2009. **526**(1): p. 166-170.
27. McKeown, J., Misra, A., Kung, H., Hoagland, R. G., & Nastasi, M., *Microstructures and strength of nanoscale Cu–Ag multilayers.* Scripta Materialia, 2002. **46**(8): p. 593-598.
28. Li, Y. P., Zhu, X. F., Zhang, G. P., Tan, J., Wang, W., & Wu, B., *Investigation of deformation instability of Au/Cu multilayers by indentation.* Philosophical Magazine, 2010. **90**(22): p. 3049-3067.
29. Kim, Y., Budiman, A. S., Baldwin, J. K., Mara, N. A., Misra, A., & Han, S. M., *Microcompression study of Al-Nb nanoscale multilayers.* Journal of Materials Research, 2012. **27**(03): p. 592-598.
30. Li, N., Wang, J., Misra, A., & Huang, J. Y. , *Direct Observations of Confined Layer Slip in Cu/Nb Multilayers.* Microscopy and Microanalysis, 2012. **18**(05): p. 1155-1162.
31. Youssef, K. M., Scattergood, R. O., Murty, K. L., Horton, J. A., & Koch, C. C. , *Ultrahigh strength and high ductility of bulk nanocrystalline copper.* Applied Physics Letters, 2005. **87**(9): p. 091904.
32. Nemat-Nasser, S. and W. Guo, *Flow stress of commercially pure niobium over a broad range of temperatures and strain rates.* Materials Science and Engineering: A, 2000. **284**(1): p. 202-210.
33. Bhattacharyya, D., Mara, N. A., Dickerson, P., Hoagland, R. G., & Misra, A., *Transmission electron microscopy study of the deformation behavior of Cu/Nb and Cu/Ni nanoscale multilayers during nanoindentation.* Journal of Materials Research, 2009. **24**(03): p. 1291-1302.
34. Hoagland, R.G., R.J. Kurtz, and C.H. Henager Jr, *Slip resistance of interfaces and the strength of metallic multilayer composites.* Scripta Materialia, 2004. **50**(6): p. 775-779.
35. Frank, F.C. and J.H. van der Merwe, *One-Dimensional Dislocations. I. Static Theory.* Proceedings of the Royal Society of London A: Mathematical, Physical and Engineering

Sciences, 1949. **198**(1053): p. 205-216.
36. Hoagland, R. G., Mitchell, T. E., Hirth, J. P., & Kung, H. , *On the strengthening effects of interfaces in multilayer fee metallic composites.* Philosophical Magazine A, 2002. **82**(4): p. 643-664.
37. Mara, N. A., Bhattacharyya, D., Dickerson, P., Hoagland, R. G., & Misra, A., *Deformability of ultrahigh strength 5 nm Cu/Nb nanolayered composites.* Applied Physics Letters, 2008. **92**(23): p. 1901.
38. Wang, J., Misra, A., Hoagland, R. G., & Hirth, J. P., *Slip transmission across fcc/bcc interfaces with varying interface shear strengths.* Acta Materialia, 2012. **60**(4): p. 1503-1513.
39. Hoagland, R.G., J.P. Hirth, and A. Misra, *On the role of weak interfaces in blocking slip in nanoscale layered composites.* Philosophical Magazine, 2006. **86**(23): p. 3537-3558.
40. Wang, J. and A. Misra, *An overview of interface-dominated deformation mechanisms in metallic multilayers.* Current Opinion in Solid State and Materials Science, 2011. **15**(1): p. 20-28.
41. Mara, N. A., Bhattacharyya, D., Hirth, J. P., Dickerson, P., & Misra, A. , *Mechanism for shear banding in nanolayered composites.* Applied Physics Letters, 2010. **97**(2): p. 021909.
42. Zhang, J. Y., Lei, S., Liu, Y., Niu, J. J., Chen, Y., Liu, G., ... & Sun, J. , *Length scale-dependent deformation behavior of nanolayered Cu/Zr micropillars.* Acta Materialia, 2012. **60**(4): p. 1610-1622.
43. Xie, J. Y., Wang, F., Huang, P., Lu, T. J., Zhang, L. F., & Xu, K. W. , *Structure transformation and coherent interface in large lattice-mismatched nanoscale multilayers.* Journal of Nanomaterials, 2013. **2013**: p. 71.
44. Misra, A. and R.G. Hoagland, *Plastic flow stability of metallic nanolaminate composites.* Journal of Materials Science, 2007. **42**(5): p. 1765-1771.
45. Han, S.M., M.A. Phillips, and W.D. Nix, *Study of strain softening behavior of Al–Al3Sc multilayers using microcompression testing.* Acta Materialia, 2009. **57**(15): p. 4473-4490.
46. Phillips, M., B. Clemens, and W. Nix, *Microstructure and nanoindentation hardness of Al/Al 3 Sc multilayers.* Acta materialia, 2003. **51**(11): p. 3171-3184.
47. Zhang, J. Y., Li, J., Liang, X. Q., Liu, G., & Sun, J. , *Achieving optimum mechanical performance in metallic nanolayered Cu/X (X = Zr, Cr) micropillars.* Scientific Reports, 2014. **4**: p. 4205.
48. Dayal, P., Quadir, M. Z., Kong, C., Savvides, N., & Hoffman, M. , *Transition from dislocation controlled plasticity to grain boundary mediated shear in nanolayered aluminum/palladium thin films.* Thin Solid Films, 2011. **519**(10): p. 3213-3220.
49. Considre, A., *LEmploi du fer et de lacier dans les constructions.* Annales de Ponts et Chausses, 1885. **9**: p. 574775.
50. Fan, C., R.T. Ott, and T.C. Hufnagel, *Metallic glass matrix composite with precipitated ductile reinforcement.* Applied Physics Letters, 2002. **81**(6): p. 1020-1022.
51. Szuecs, F., C. Kim, and W. Johnson, *Mechanical properties of Zr 56.2 Ti 13.8 Nb 5.0 Cu 6.9 Ni 5.6 Be 12.5 ductile phase reinforced bulk metallic glass composite.* Acta Materialia, 2001. **49**(9): p. 1507-1513.
52. Kühn, U., Eckert, J., Mattern, N., & Schultz, L., *ZrNbCuNiAl bulk metallic glass matrix composites containing dendritic bcc phase precipitates.* Applied physics letters, 2002. **80**(14): p. 2478-2480.
53. Lu, Y. and P.K. Liaw, *The mechanical properties of nanostructured materials.* JOM. **53**(3):

p. 31-35.
54. He, G., Eckert, J., Löser, W., & Schultz, L. , *Novel Ti-base nanostructure–dendrite composite with enhanced plasticity.* Nature Materials, 2003. **2**(1): p. 33-37.
55. Oliver, W.C. and G.M. Pharr, *An improved technique for determining hardness and elastic modulus using load and displacement sensing indentation experiments.* Journal of materials research, 1992. **7**(06): p. 1564-1583.
56. Oliver, W.C. and G.M. Pharr, *Measurement of hardness and elastic modulus by instrumented indentation: Advances in understanding and refinements to methodology.* Journal of materials research, 2004. **19**(01): p. 3-20.
57. Fischer-Cripps, A.C., *Nanoindentation testing*, in *Nanoindentation*. 2011, Springer. p. 21-37.
58. Wilsdorf, H., *Apparatus for the deformation of foils in an electron microscope.* Review of Scientific Instruments, 1958. **29**(4): p. 323-324.
59. Yu, Q., M. Legros, and A. Minor, *In situ TEM nanomechanics.* Mrs Bulletin, 2015. **40**(1): p. 62-70.
60. Haque, M.A. and M.T.A. Saif, *In-situ tensile testing of nano-scale specimens in SEM and TEM.* Experimental Mechanics, 2002. **42**(1): p. 123-128.
61. Li, N., Wang, J., Mao, S., & Wang, H., *In situ nanomechanical testing of twinned metals in a transmission electron microscope.* MRS Bulletin, 2016. **41**(4): p. 305-313.
62. Oh, S. H., Legros, M., Kiener, D., & Dehm, G. , *In situ observation of dislocation nucleation and escape in a submicrometre aluminium single crystal.* Nature materials, 2009. **8**(2): p. 95.
63. Clouet, E., Caillard, D., Chaari, N., Onimus, F., & Rodney, D., *Dislocation locking versus easy glide in titanium and zirconium.* Nature materials, 2015. **14**(9): p. 931.
64. Wang, J., Li, N., Anderoglu, O., Zhang, X., Misra, A., Huang, J. Y., & Hirth, J. P., *Detwinning mechanisms for growth twins in face-centered cubic metals.* Acta Materialia, 2010. **58**(6): p. 2262-2270.
65. Ye, J., Mishra, R. K., Sachdev, A. K., & Minor, A. M., *In situ TEM compression testing of Mg and Mg–0.2 wt.% Ce single crystals.* Scripta Materialia, 2011. **64**(3): p. 292-295.
66. Morrow, B. M., McCabe, R. J., Cerreta, E. K., & Tomé, C. N., *In-situ TEM observation of twinning and detwinning during cyclic loading in Mg.* metallurgical and materials Transactions a, 2014. **45**(1): p. 36-40.
67. Wang, J., Zeng, Z., Weinberger, C. R., Zhang, Z., Zhu, T., & Mao, S. X. , *In situ atomic-scale observation of twinning-dominated deformation in nanoscale body-centred cubic tungsten.* Nature materials, 2015. **14**(6): p. 594.
68. Yu, Q., Shan, Z. W., Li, J., Huang, X., Xiao, L., Sun, J., & Ma, E. , *Strong crystal size effect on deformation twinning.* Nature, 2010. **463**(7279): p. 335.
69. Li, N., Wang, J., Misra, A., Zhang, X., Huang, J. Y., & Hirth, J. P., *Twinning dislocation multiplication at a coherent twin boundary.* Acta Materialia, 2011. **59**(15): p. 5989-5996.
70. Nó, M. L., Ibarra, A., Caillard, D., & San Juan, J., *Stress-induced phase transformations studied by in-situ transmission electron microscopy*. in *Journal of Physics: Conference Series*. 2010. IOP Publishing.
71. Ma, X., Guo, X., Fu, M., & Qiao, Y., *In-situ TEM observation of hcp-Ti to fcc-Ti phase transformation in Nb-Ti-Si based alloys.* Materials Characterization, 2018. **142**: p. 332-339.
72. Liu, Y., Karaman, I., Wang, H., & Zhang, X., *Two Types of Martensitic Phase Transformations in Magnetic Shape Memory Alloys by In-Situ Nanoindentation Studies.*

Advanced Materials, 2014. **26**(23): p. 3893-3898.
73. J Jiang, B., Tadaki, T., Mori, H., & TY, H. X. Z. , *In-situ TEM Observation of γ→ ε Martensitic Transformation during Tensile Straining in an Fe–Mn–Si Shape Memory Alloy.* Materials transactions, JIM, 1997. **38**(12): p. 1072-1077.
74. Ohmura, T., Minor, A. M., Stach, E. A., & Morris, J. W. , *Dislocation–grain boundary interactions in martensitic steel observed through in situ nanoindentation in a transmission electron microscope.* Journal of Materials Research, 2004. **19**(12): p. 3626-3632.
75. Lee, T., I. Robertson, and H. Birnbaum, *AnIn Situ transmission electron microscope deformation study of the slip transfer mechanisms in metals.* Metallurgical Transactions A, 1990. **21**(9): p. 2437-2447.
76. Lee, T., I. Robertson, and H. Birnbaum, *TEM in situ deformation study of the interaction of lattice dislocations with grain boundaries in metals.* Philosophical Magazine A, 1990. **62**(1): p. 131-153.
77. De Hosson, J. T., Soer, W. A., Minor, A. M., Shan, Z., Stach, E. A., Asif, S. S., & Warren, O. L., *In situ TEM nanoindentation and dislocation-grain boundary interactions: a tribute to David Brandon.* Journal of materials science, 2006. **41**(23): p. 7704-7719.
78. Kiener, D., Hosemann, P., Maloy, S. A., & Minor, A. M. , *In situ nanocompression testing of irradiated copper.* Nature materials, 2011. **10**(8): p. 608.
79. Dillon, S. J., Bufford, D. C., Jawaharram, G. S., Liu, X., Lear, C., Hattar, K., & Averback, R. S. , *Irradiation-induced creep in metallic nanolaminates characterized by In situ TEM pillar nanocompression.* Journal of Nuclear Materials, 2017. **490**: p. 59-65.
80. Jin, M., Minor, A. M., Stach, E. A., & Morris Jr, J. W. , *Direct observation of deformation-induced grain growth during the nanoindentation of ultrafine-grained Al at room temperature.* Acta Materialia, 2004. **52**(18): p. 5381-5387.
81. Gouldstone, A., Chollacoop, N., Dao, M., Li, J., Minor, A. M., & Shen, Y. L., *Indentation across size scales and disciplines: Recent developments in experimentation and modeling.* Acta Materialia, 2007. **55**(12): p. 4015-4039.
82. Minor, A. M., Lilleodden, E. T., Stach, E. A., & Morris, J. W., *Direct observations of incipient plasticity during nanoindentation of Al.* Journal of Materials Research, 2011. **19**(1): p. 176-182.
83. Legros, M., D.S. Gianola, and K.J. Hemker, *In situ TEM observations of fast grain-boundary motion in stressed nanocrystalline aluminum films.* Acta Materialia, 2008. **56**(14): p. 3380-3393.
84. Soer, W. A., De Hosson, J. T. M., Minor, A. M., Morris Jr, J. W., & Stach, E. A. , *Effects of solute Mg on grain boundary and dislocation dynamics during nanoindentation of Al–Mg thin films.* Acta materialia, 2004. **52**(20): p. 5783-5790.
85. Eftink, B. P., Li, A., Szlufarska, I., Mara, N. A., & Robertson, I. M. , *Deformation response of AgCu interfaces investigated by in situ and ex situ TEM straining and MD simulations.* Acta Materialia, 2017. **138**: p. 212-223.
86. Misra, A., J.P. Hirth, and R.G. Hoagland, *Length-scale-dependent deformation mechanisms in incoherent metallic multilayered composites.* Acta Materialia, 2005. **53**(18): p. 4817-4824.
87. Foecke, T. and D. Van Heerden, *Experimental observations of deformation mechanisms in metallic nanolaminates.* Chemistry and Physics of Nanostructures and Related Non-Equilibrium Materials, 1997: p. 193-200.
88. Freund, L., *The driving force for glide of a threading dislocation in a strained epitaxial*

layer on a substrate. Journal of the Mechanics and Physics of Solids, 1990. **38**(5): p. 657-679.
89. Misra, A., J.P. Hirth, and H. Kung, *Single-dislocation-based strengthening mechanisms in nanoscale metallic multilayers.* Philosophical Magazine A, 2002. **82**(16): p. 2935-2951.
90. Li, N., Wang, J., Misra, A., & Huang, J. Y. , *Direct Observations of Confined Layer Slip in Cu/Nb Multilayers.* Microscopy and Microanalysis, 2012. **18**(5): p. 1155-1162.
91. Li, Y. P., Zhu, X. F., Tan, J., Wu, B., Wang, W., & Zhang, G. P., *Comparative investigation of strength and plastic instability in Cu/Au and Cu/Cr multilayers by indentation.* Journal of Materials Research, 2011. **24**(3): p. 728-735.
92. Han, W. Z., Carpenter, J. S., Wang, J., Beyerlein, I. J., & Mara, N. A. , *Atomic-level study of twin nucleation from face-centered-cubic/body-centered-cubic interfaces in nanolamellar composites.* Applied Physics Letters, 2012. **100**(1): p. 011911.
93. Zheng, S. J., Beyerlein, I. J., Wang, J., Carpenter, J. S., Han, W. Z., & Mara, N. A. , *Deformation twinning mechanisms from bimetal interfaces as revealed by in situ straining in the TEM.* Acta Materialia, 2012. **60**(16): p. 5858-5866.
94. Lu, L., Shen, Y., Chen, X., Qian, L., & Lu, K. , *Ultrahigh strength and high electrical conductivity in copper.* Science, 2004. **304**(5669): p. 422-426.
95. Lu, L., Chen, X., Huang, X., & Lu, K., *Revealing the maximum strength in nanotwinned copper.* Science, 2009. **323**(5914): p. 607-610.
96. *Evading the strength–ductility trade-off dilemma in steel through gradient hierarchical nanotwin*, *Evading the strength–ductility trade-off dilemma in steel through gradient hierarchical nanotwins.* Nature communications, 2014. **5**: p. 3580.
97. Li, N., Wang, J., Huang, J. Y., Misra, A., & Zhang, X., *In situ TEM observations of room temperature dislocation climb at interfaces in nanolayered Al/Nb composites.* Scripta Materialia, 2010. **63**(4): p. 363-366.
98. Wang, J., R.G. Hoagland, and A. Misra, *Room-temperature dislocation climb in metallic interfaces.* Applied Physics Letters, 2009. **94**(13): p. 131910.
99. Liao, X.Z., Srinivasan, S.G., Zhao, Y.H., Baskes, M.I., Zhu, Y.T., Zhou, F., Lavernia, E.J. and Xu, H.F., *Formation mechanism of wide stacking faults in nanocrystalline Al.* Applied Physics Letters, 2004. **84**(18): p. 3564-3566.
100. Hattar, K., Misra, A., Dosanjh, M. R. F., Dickerson, P., Robertson, I. M., & Hoagland, R. G. , *Direct Observation of crack propagation in copper–niobium multilayers.* Journal of Engineering Materials and Technology, 2012. **134**(2): p. 021014.
101. Liu, Z., Monclús, M. A., Yang, L. W., Castillo-Rodríguez, M., Molina-Aldareguía, J. M., & LLorca, J. , *Tensile deformation and fracture mechanisms of Cu/Nb nanolaminates studied by in situ TEM mechanical tests.* Extreme Mechanics Letters, 2018. **25**: p. 60-65.
102. Li, N., Mara, N. A., Wang, J., Dickerson, P., Huang, J. Y., & Misra, A. , *Ex situ and in situ measurements of the shear strength of interfaces in metallic multilayers.* Scripta Materialia, 2012. **67**(5): p. 479-482.
103. Ge, D., V. Domnich, and Y. Gogotsi, *High-resolution transmission electron microscopy study of metastable silicon phases produced by nanoindentation.* Journal of applied physics, 2003. **93**(5): p. 2418-2423.
104. Lee, J. H., Kim, I., Hulbert, D. M., Jiang, D., Mukherjee, A. K., Zhang, X., & Wang, H. , *Grain and grain boundary activities observed in alumina–zirconia–magnesia spinel nanocomposites by in situ nanoindentation using transmission electron microscopy.* Acta Materialia, 2010. **58**(14): p. 4891-4899.

105. Ye, J., Mishra, R. K., Pelton, A. R., & Minor, A. M. (, *Direct observation of the NiTi martensitic phase transformation in nanoscale volumes.* Acta Materialia, 2010. **58**(2): p. 490-498.
106. Jin, M., Minor, A. M., Stach, E. A., & Morris Jr, J. W. , *Direct observation of deformation-induced grain growth during the nanoindentation of ultrafine-grained Al at room temperature.* Acta Materialia, 2004. **52**(18): p. 5381-5387.

Chapter 3 Experimental

3.1 Synthesis of Metallic nanocomposites through physical vapor deposition

A specific PVD process namely magnetron sputtering was used to prepare the metallic nanocomposites for my research. During the sputtering process, gas ions are energized to "knock off" atoms from the target which are then deposited onto the substrate. The main component of a sputtering equipment is a vacuum chamber that is electrically wired to single or multiple cathodes, where the target materials are connected to, and an anode, where coating of the substrate takes place. (Figure 3.1a) During a typical sputtering process, after the substrate is loaded into the sputtering chamber, the chamber is first pumped to high vacuum, reaching a base pressure, so that the background gas and potential contaminants can be depleted to minimum. The sputtering gas, which is typically Ar for metallic material deposition, is then flowed into the chamber to maintain

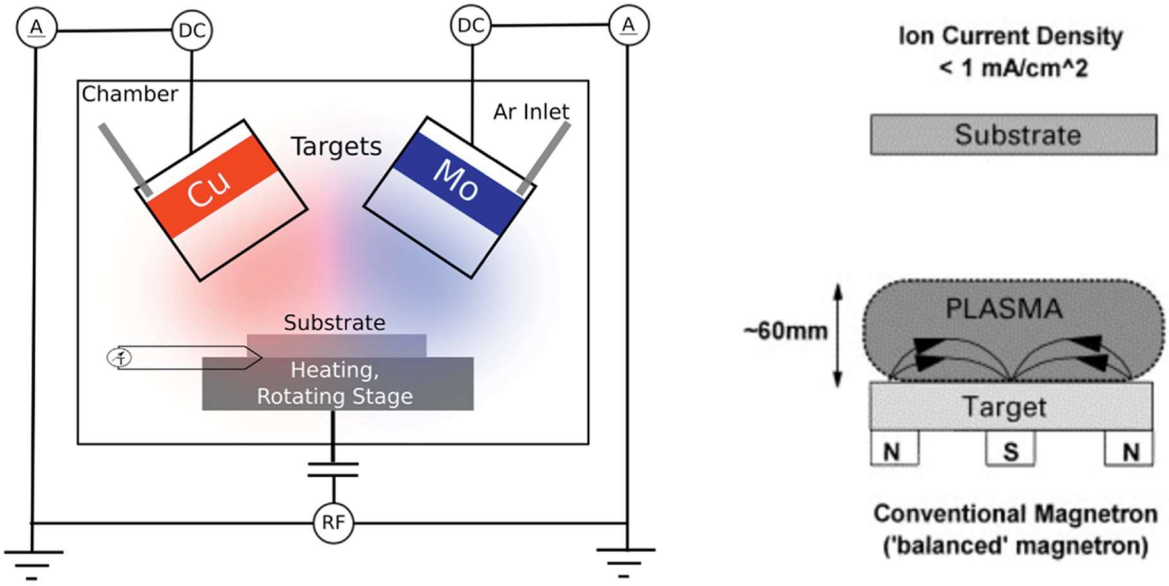

Figure 3.1 Schematics of (a) conventional sputtering chamber with two targets and (b) magnetron sputtering process.

a sputtering pressure. After that, high voltage is applied between the cathode and the anode, providing energy high enough to ionize the atoms in the sputtering gas. The positively charged gas ions are then accelerated towards the negatively charged cathode, where the target is placed.

A magnetron sputtering is variation of basic sputtering process where magnets are added adjacent to the target, a schematic of which can be found in Figure 3.1 [1]. The arrangement of the magnets keeps one pole at the central axis of the target, while the second pole is formed by a ring of magnets around the outer edge of the target. The magnetic field can thus restrain the movement of secondary electrons, trapping them to the vicinity of the target. The probability of the gas atoms ionized by electron collision is increased, which leads to a denser plasma in the target region and a consequent increase in ion bombardment of the target. As a result, the sputtering rate of the target materials and the deposition rate on the substrate are improved. Meanwhile, the operating pressure can be lowered from 1 mTorr to 10 mTorr and the operating voltages can lowered from 2-3 kV to ~ 500V.

For the purpose of my research, two targets, one made of 99.99% pure Cu and the other made of 99.95 % pure Mo are co-sputtered together at the same rate to prepare the nanocomposite thin films. Cu and Mo are selected as a model system for fcc-bcc metals because they are immiscible even at high temperatures and thus can produce nanocomposites from phase separation, due to their high heat of mixing at +19 kJ/mol. To promote phase separation during deposition, high deposition temperatures were attempted. With manipulation of two key parameters: the deposition temperature and the deposition rate, nanocomposites with various morphologies have been produced.

3.2 Morphological Characterization of nanocomposites

The morphologies of the nanocomposites were examined using transmission electron microscope (TEM) and scanning transmission electron microscope (STEM). Electron transparent samples with thickness typically below 100 nm are required for such examinations. The thin film samples were prepared in both cross-sectional view and plan view to obtain three-dimensional information. Three approaches can be used to fabricate the TEM samples. First is conventional preparation, as demonstrated in Figure 3.2, where the sample is first cut into small size (~ 2 mm x 3 mm) and ground with diamond lapping film to a thickness less than 30 μm. After gluing the sample to a TEM grid, electron transparent region (typically less than 100 nm thick) can be achieved with Ar^+ ion polishing using a Gatan precision ion polishing system (PIPS). An alternative way is to prepare an H-bar sample (Figure 3.3). The difference is that the ground sample is glued to a half grid. Electron transparent area can then be produced by milling off excess material

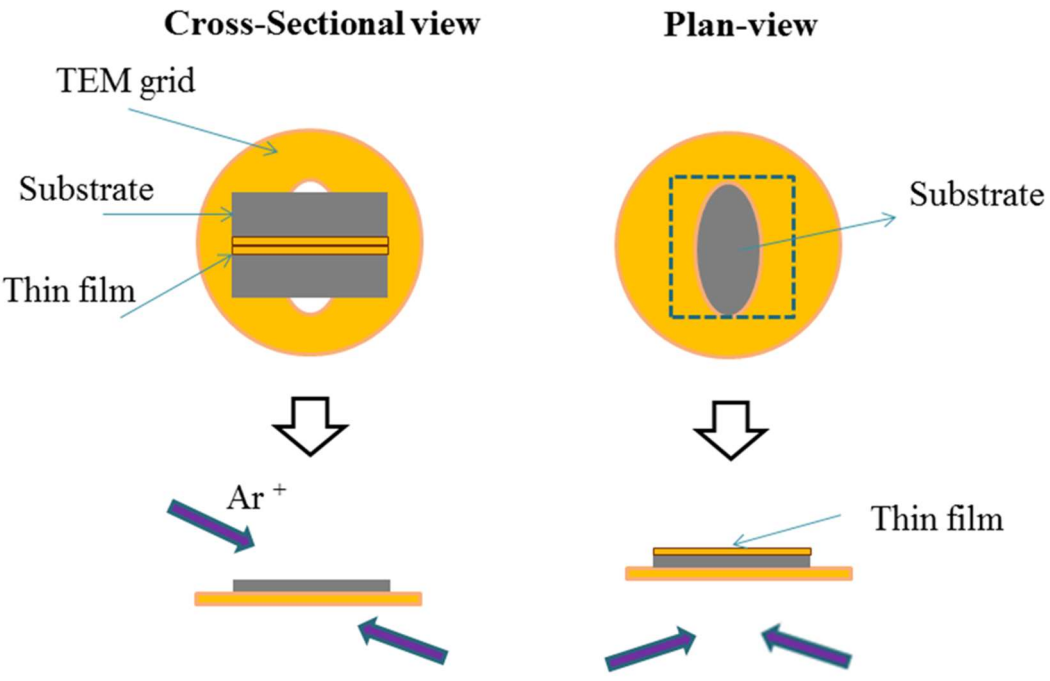

Figure 3.2 Process of conventional preparation of TEM sample.

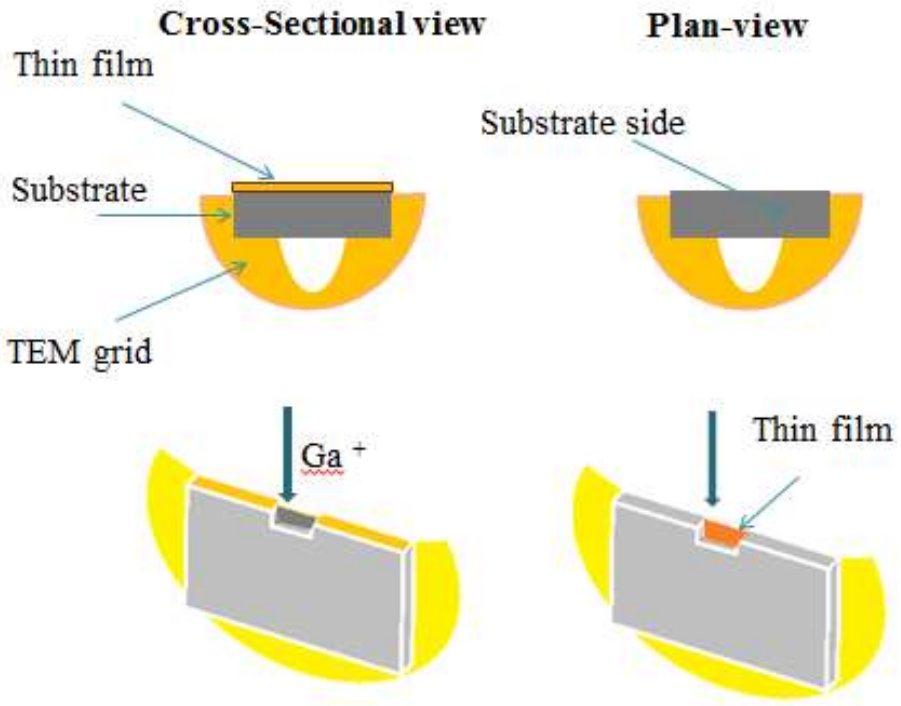

Figure 3.3 Process of preparing H-bar TEM sample.

with focused ion beam (FIB). The advantage of using H-Bar approach is that the thin area can be selectively located. For instance, a plan-view sample can be made at different depths of the thin film, providing thorough information of the material. The disadvantage of using FIB is that more ion damage will be introduced to the material because a heavier ion source (Ga^+) is used. Another method depends more heavily on the usage of FIB, which is normally named FIB lift-out method. As demonstrated in Figure 3.4, a Pt strip is first deposited on the designated sample area. Then the FIB is used to remove material from two size of the Pt strip so that the region under Pt will be exposed. The slice of material protected under the Pt can then be attached to an Omniprobe and cut out to be welded to a TEM grid using Pt. Further thinning using FIB gives a TEM ready specimen.

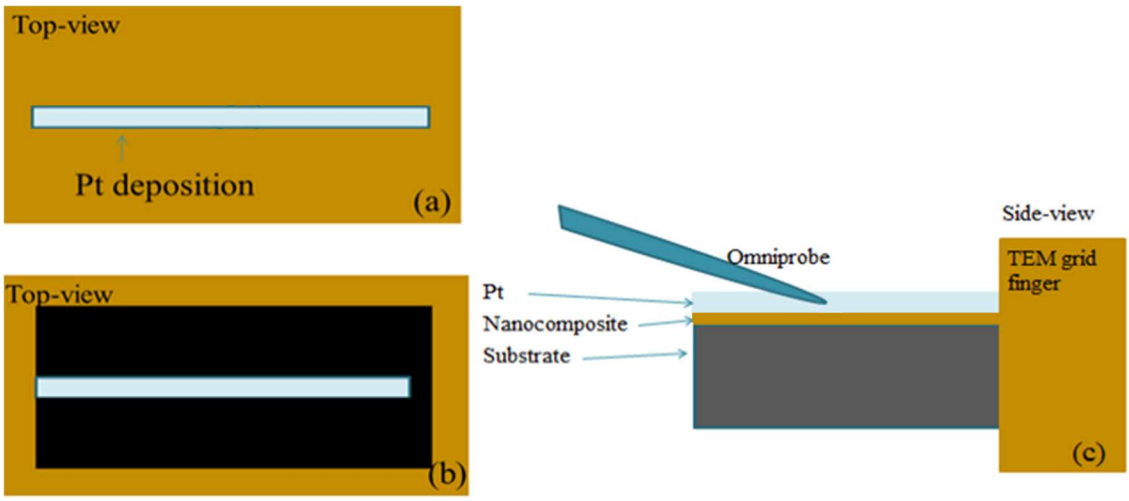

Figure 3.4 Process of preparing TEM sample using FIB lift-out technique.

With Z-contrast STEM imaging and energy dispersive spectroscopy (EDS) of electron energy loss spectroscopy (EELS) mapping, the distribution of the two constituent metals can be determined. More information about the composite like the orientation relationship between the two phases and interface structure can be obtained from high resolution atomic images, electron diffraction and diffraction contrast imaging.

3.3 Nanoindentation test

Hysitron TI-950 Triboindenter was used to perform nanoindentation on the samples and measure the hardness and elastic modulus of the nanocomposite through the previously discussed approach. The yield strength can then be approximated as one third of the hardness value.[2] Prior to the testing, surface roughness should be measured. This can be done through the scanning probe microscopy (SPM) function of the Triboindenter or more accurately using an atomic force microscope (AFM). According to ISO 14577 standard, the indentation depth must be at least three times the surface roughness to perform a valid measurement. Besides, when measuring thin films, the indentation depth should be less than tenth of the film thickness to avoid substrate effects.[3]

Besides measuring hardness and elastic modulus, the Triboindenter can be utilized to introduce plastic deformation into the sample. Surface of the indented sample was examined using AFM and scanning electron microscope (SEM) to examine the flow behavior of the material. Due to small size of the indentations, it is usually difficult to locate them on the sample surface for further examination. Pt markers which are visible under optical microscope can be deposited on the sample surface first using FIB. Indentations are then made around the marker so that they can then be easily traced using AFM or SEM. More detailed investigation in TEM can be performed via preparing TEM samples from the indented region using FIB lift-out technique (Figure 3.4).

3.4 In situ nanomechanical testing

In my research, *in situ* nano-pillar compression test, tensile test and pre-notched bend test were conducted to study different aspects of the mechanical behavior of metallic materials.

3.4.1 Platforms for in situ nanomechanical testing

Three nanoindentation platforms were used to perform *in situ* straining experiment in SEM or TEM, namely Hysitron PI95 Picoindenter, Hysitron PI85 Picoindenter and Thermo Fisher (FEI/Nanofactory) scanning tunneling microscopy (STM)-TEM holder. Figure 3.5a shows a photo of part of a Hysitron PI95 Picoindenter, which is built in a TEM sample holder. The sample to be tested is fixed on a sample stage. The indentation tip is connected to a piezo-electric scanner and a transducer. The scanner controls the movement of the tip in three directions, while the transducer drives the tip to do indentation and measures load and displacement. Fig shows a schematic of a transducer and Fig demonstrates its working mechanisms. Key components of a transducer include three conductor plates. The indentation tip is attached to the center plate, which is held in place by springs at the two sides. Alternating current (AC) signals 180^{o} out of phase are applied to the top and bottoms plates. When same amplitude signals are fed to the two plates, zero signal is received

by the center plate, and the system is at rest state. When the signals at the two plates do not cancel out each other, a maximum 1 mN electrostatic force can be exerted to the center plate, driving the

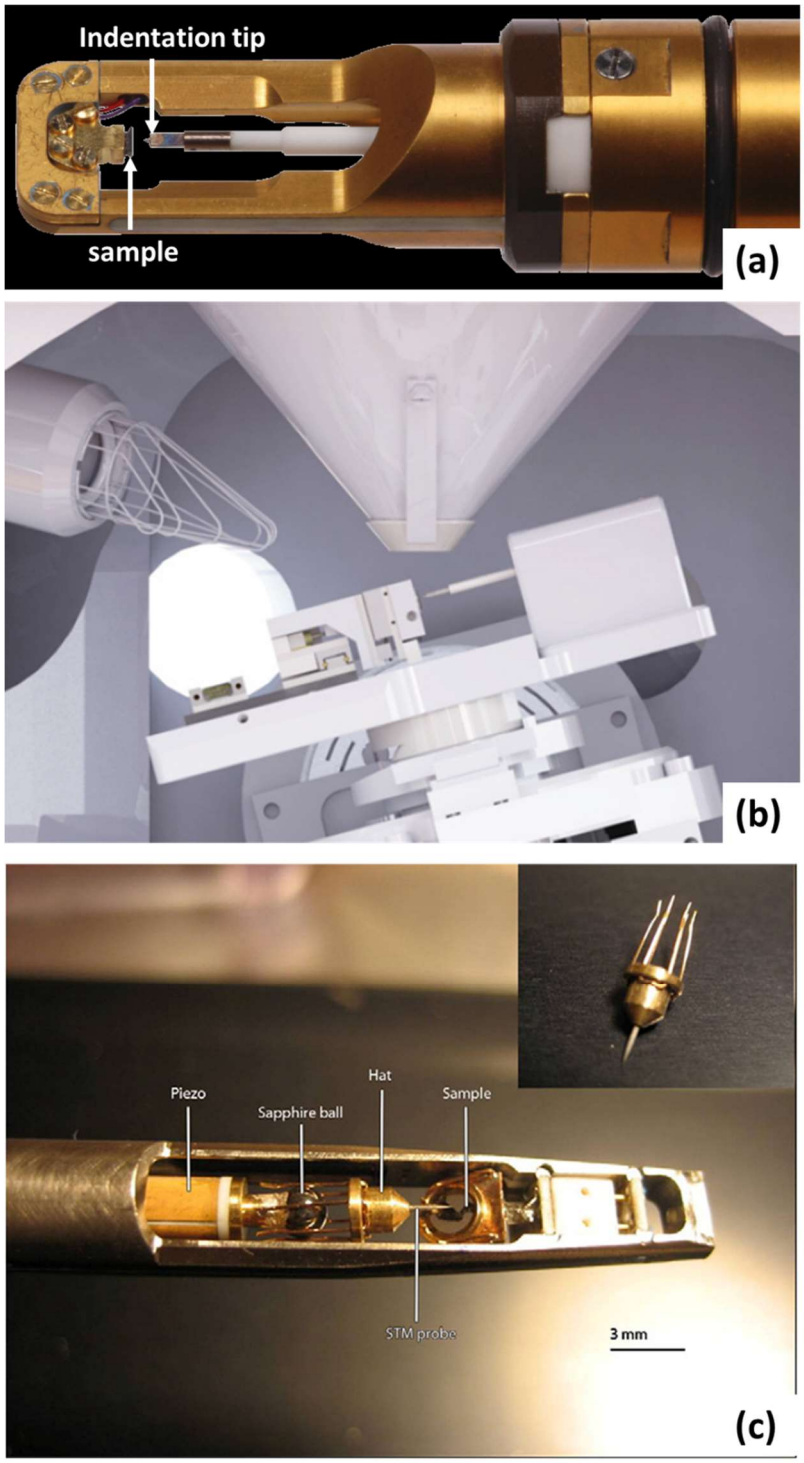

Figure 3.5 Photos of (a) Hysitron PI95 Picoindenter, (b) Hysitron PI85 Picoindenter inside an SEM chamber, and (c) Thermo Fisher STM-TEM holder

indentation process. This electrostatic actuation process provides advantages over electromagnetic actuation as less current is applied and thus less heat dissipation is evolved. Heat dissipation deteriorates the precision of nanoindentation measurements drastically because it causes thermal drift of the tip. The displacement noise floor of a PI 95 can be controlled below 1 nm. Figure 3.5b shows a photo of a Hysitron PI85 Picoindenter inside an SEM chamber. The PI85 works with a mechanism similar to that of a PI95, where the indentation tip is connected to a transducer to perform nanoindentation. The difference is that PI85 is used in SEM and maximum load of 10 mN can be applied. Figure 3.5c shows a photo of the sample mounting part of a Thermo Fisher STM-TEM holder. A W wire with an electrochemically etched tip that has a diameter of ~ 100 nm is attached to a Cu "hat" that has six fingers. The six fingers grab onto a sapphire ball which is controlled by a piezo tube. Electric pulses are generated by the piezo tube and drive the movement of the Cu "hat", so that the W tip can perform nanoindentation on the fixed sample. Because each pulse can just move the tip by a step as small as a few Å, high-res TEM images can be captured from the sample while it is deformed.

3.4.2 In situ micro-/nano pillar compression

Figure 3.6 a to c demonstrate the general process of FIB-assisted micro-/nano- pillar fabrication. Thermo Fisher Helios dual-beam SEM was used, which has a maximum ion beam voltage of 30 kV. This high voltage is used for better resolution and thus more precise control of the pillar shape. For the initial step, (Figure 3.6a) high current at 20~40 nA is used to create ring shaped trench around the designated pillar area. Followed by that, gradually reduced current values are used to reduce the diameter of the center disk step by step (Figure 3.6b), finally exposing the micro- or nano- pillar.(Figure 3.6c) Aspect of the pillar is controlled at 2:1 to 3:1 for a valid pillar compression test. One problem of this intuitive approach is that due to the convergence angle of

the ion beam, the pillars are produced with an inevitable taper angle (Figure 3.6d). Focusing of the ion beam is crucial to reduce this taper angle. When the designed diameter of the pillar is larger

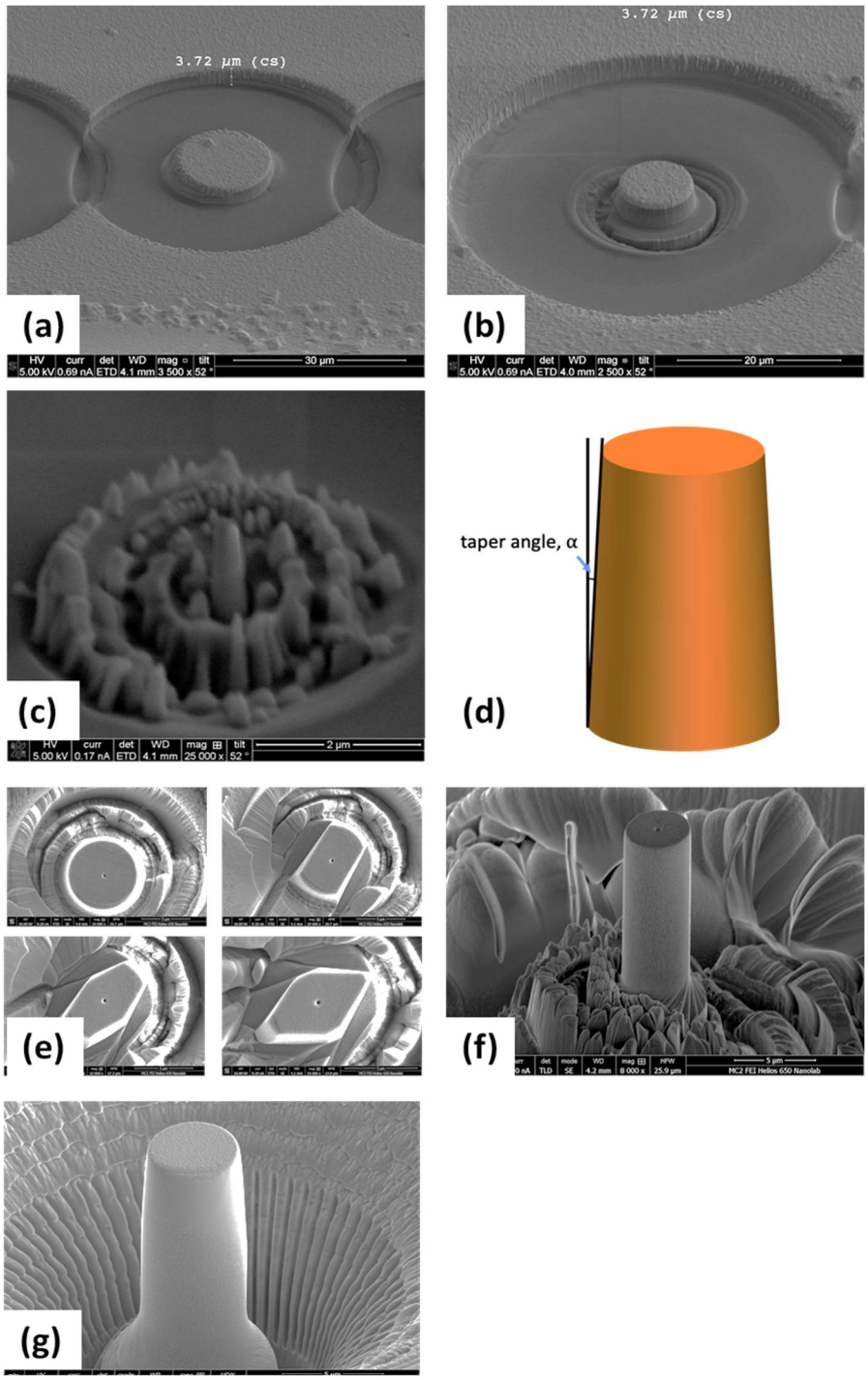

Figure 3.6 (a)-(c) SEM images taken during the fabrication of a nanopillar. (d) Schematic showing taper angle of a nanopillar. (e) Process of making taper-free pillars. (f)(g) Micro-pillar with no taper angle.

than a few microns, a method can be used to eliminate tapering of the pillar. This alternative method comes into play during the final stage of thinning, when the pillar diameter is only a few microns larger than design. As shown in Figure 3.6e, a marker is made at the center of the pillar's top surface to assist the positioning of the pillar. The axis is tilted to be 52^{o} off the ion beam direction so that two sides of the pillar can be milled off. Then the pillar is rotated 5^{o} or 10^{o} along its axis to get the two sides milled off. With this process repeated, a pillar with no taper angle can be made. (Figure 3.6f) Automated script can be created using the SEM software to reduce the human power for this process. (Figure 3.6g) For smaller pillars, due to the limitation of stage positioning and FIB resolution, this method is usually not feasible. Hysitron PI85 (in SEM) and PI95 (in TEM) are used as platform to conduct compression test on the pillars with diamond flat punch tips. The strain rate was kept at 0.2% s^{-1}.

3.4.3 In situ Tensile test in TEM

A "push-to-pull" device was used to conducted tensile test in TEM. (Figure 3.7) As show in Figure 3.7b, the core of a "push-to-pull" device is a silicon chip composed of a mobile portion and a fixed portion connected by four springs. When a sample is mounted across the "gap" between the mobile and fixed parts, tensile test can be conducted by pushing the mobile part with a Hysitron PI95 Picoindenter. As shown in Figure 3.7 c-i, the preparation of a tensile sample starts like conventional FIB TEM sample preparation. Instead of reducing the sample thickness to a few tens of nm, the thinning process stop at a sample thickness of 200-300 nm. Then a rectangular sample with dimension of ~ 5 μm x ~ 2 μm is cut out and attached to an Omniprobe. The Ominiprobe then transfers the sample to the "push-to-pull" device and glued across the "gap" using Pt deposition. Finally, "dog bone" shaped specimen can be fabricated for testing. With this approach, small specimens prepared from designated areas of a sample can be isolated tested individually.

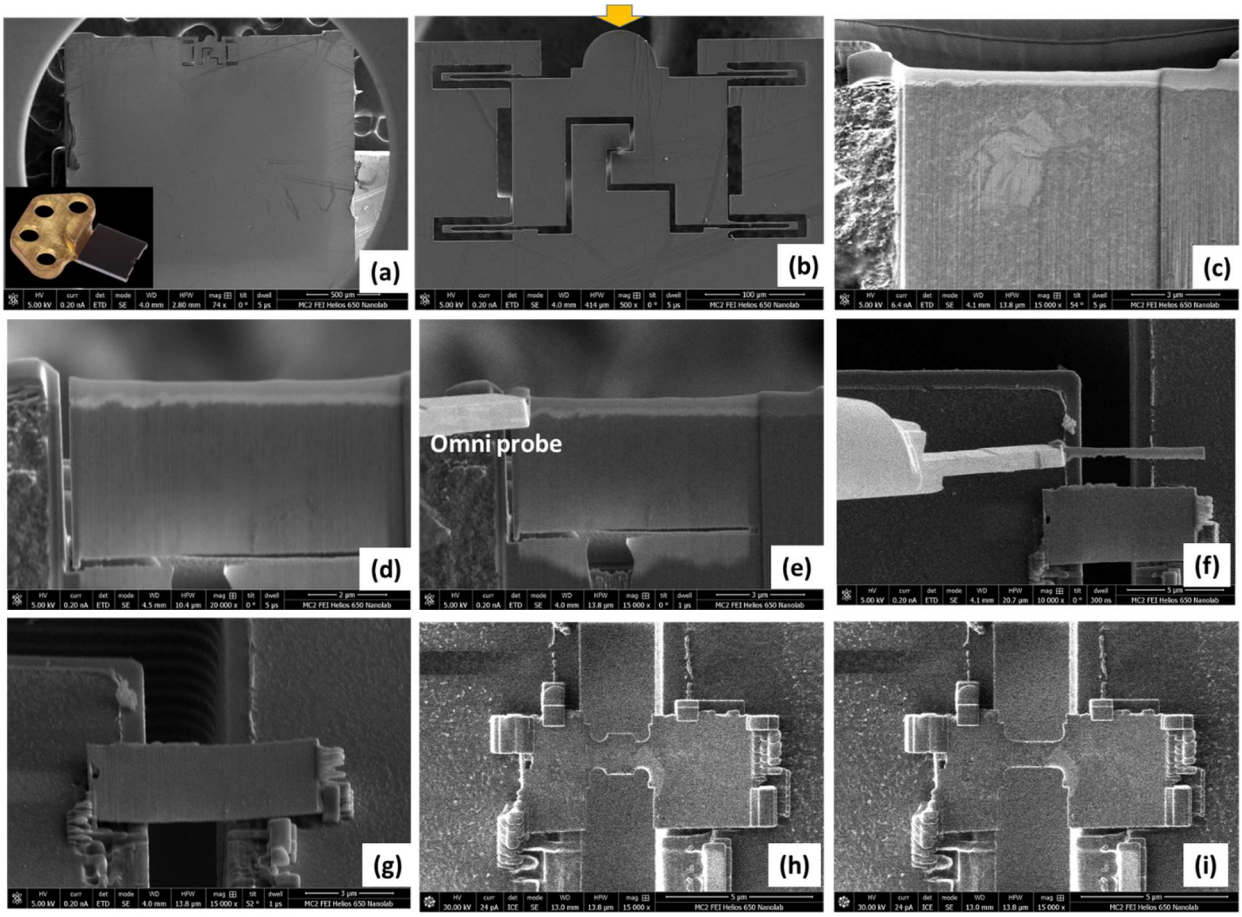

Figure 3.7 (a) SEM image of the push-to-pull device. Inset: photo of the deviced mounted on a sample state; (b) SEM image of the working part of the push-to-pull device. (c) to (i) Process of fabricating a tensile test sample using FIB lift-out technique.

For example, in Figure 3.7c, specimens can be made from the Cu-rich region (brighter) and the Mo-rich region (darker) to measure the mechanical property of each region.

3.4.4 In situ pre-notched 3-point bend test in SEM

As sample tilting of 90° is involved to expose side of the bend structure to make notch using ion beam, the bend structures need to be prepared near the edge the sample. Figure 3.8 demonstrates the process of sample preparation for 3-point bend setup, which can be generalized in four steps: (i) initial coarse milling with high current from 20 to 9 nA to create a thin brick-like structure; (ii) remount the sample to a 38° tilt stage in order to access the side of the three-point

bend structure and create the beam structure with current ~ 5 nA; (iii) milling of the notch at low current ~ 0.1 nA; (iv) remount the sample to initial configuration from step (i) in order to "polish" both back and front of the three-point bend structure with small current ~ 2 nA. An indentation tip with a round end surface that has a diameter ~ 5 μm was used to press at the middle of beam from above the notch for the bend test.

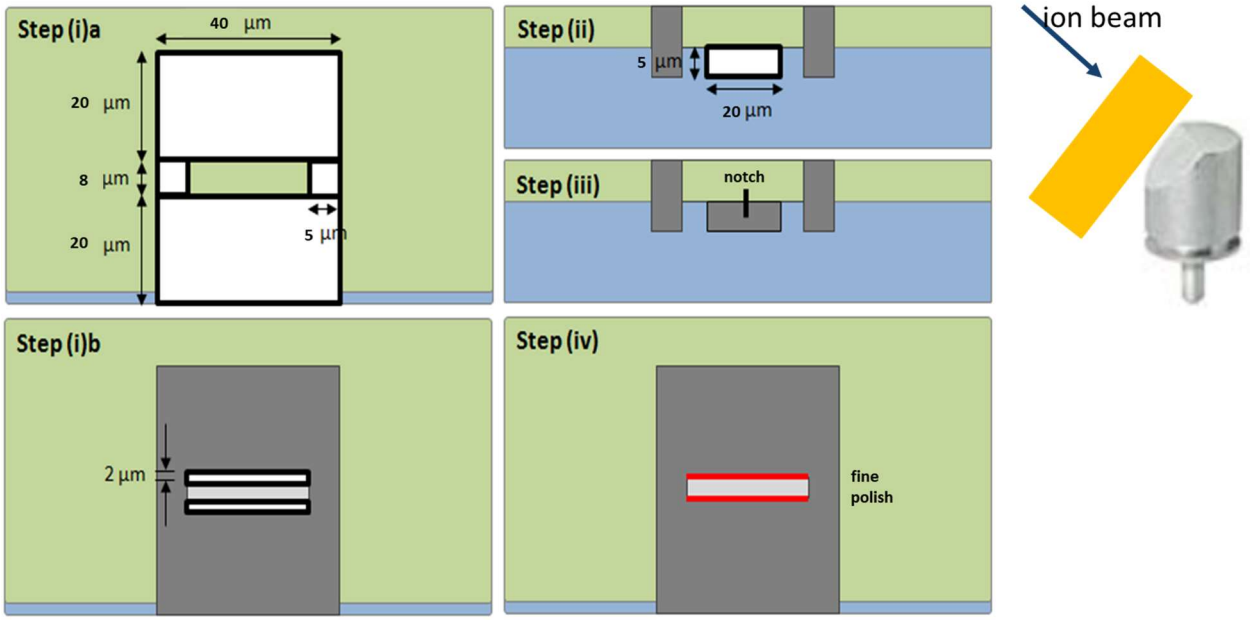

Figure 3.8 Schematics showing the process of making pre-notched bean for *in situ* bend test.

3.5 References

1. Kelly, P.J. and R.D. Arnell, *Magnetron sputtering: a review of recent developments and applications.* Vacuum, 2000. **56**(3): p. 159-172.
2. Zhang, P., S.X. Li, and Z.F. Zhang, *General relationship between strength and hardness.* Materials Science and Engineering: A, 2011. **529**: p. 62-73.
3. Fischer-Cripps, A.C., *Nanoindentation Test Standards*, in *Nanoindentation*. 2011, Springer. p. 181-198.

Chapter 4 Deformation Mechanisms of Monolithic Cu/Mo Nanocomposites

4.1 Introduction

This chapter discusses the deformation mechanisms of Cu-Mo nanocomposite with different monolithic morphologies based on experimental results from nano-pillar compression tests. Monolithic means that the microstructure can be described by one representative length, which can be the layer thickness or ligament width. Multilayer Cu-Mo nanocomposite was prepared by sequentially depositing 3 nm layers of each of the two metals at room temperature. Limited deformability was observed in the sample where localized shear was observed after compression. Through co-sputtering Cu and Mo at different temperatures, nanocomposites with lateral and random concentration modulations (LCMs and RCMs) were fabricated. Ligament size and coherency of the Cu/Mo interfaces was also controlled via the deposition conditions. It was discovered that nanocomposites with LCM structure and coherent interfaces have high strength but limited deformability. Enhanced deformability was achieved when the interface was altered to semi-coherent, although plasticity was localized in kink bands. The RCM structure design with semi-coherent interfaces showed an excellent combination of high flow strength and plastic deformability due to suppression of shear and kink bands.

Structural manipulation at the nanoscale has proven to be an effective approach to achieve improved strength while still preserving plastic deformability. Reported methods include

introducing nanotwin substructures into the grains [1-3], generating a bimodal grain size distribution with micrometer-sized grains embedded in a nanocrystalline grain matrix [4, 5], or a gradient nano-grained structure [6], creating a hierarchical structure with nanometer grains and solute structures[7] and reducing the size of a metallic glass to sub-micrometer scale [8]. These studies have improved the understanding of mechanical behavior of single-phase nanostructured metals. In this work, we attempt to achieve both strength and deformability by structural design of metallic composites at nanoscale, the outcome of which will be applicable to a broad range of multi-phase material systems.

Metallic nanocomposites (MNC) have been studied to exhibit high uniaxial strengths approaching 1/2 to 1/3 of the theoretical limit (of the order of $\mu/30$ where μ is the shear modulus) in the form of multilayers [9, 10]. A general "smaller is stronger" trend has been observed, where dislocations pile up against the interfaces and Hall-Petch law is followed when the layer thickness, t, is above sub-micron scale, single dislocation glide confined by the adjacent interfaces dominates when t is in order of a few tens of nanometers, and dislocation transmit through the interfaces when t is further reduced to a few nm [11, 12]. Similar to many other high strength materials, uniform plastic deformability of the nano-multilayers is very limited. Localized deformation in the form of shear bands results in strain softening and even premature failure of the material [13, 14]. A new design in morphology other than the multilayers is needed to promote a less detrimental mode of deformation and improve the plasticity of MNCs.

In terms of the distribution of the constituents, the multilayered structure can also be categorized as vertical concentration modulations (VCMs), as depicted in Figure 1.1a. Keeping away from VCM that is prone to shear banding, our design targets other morphologies: lateral concentration modulation (LCM), where the phases separate in the lateral direction, giving a

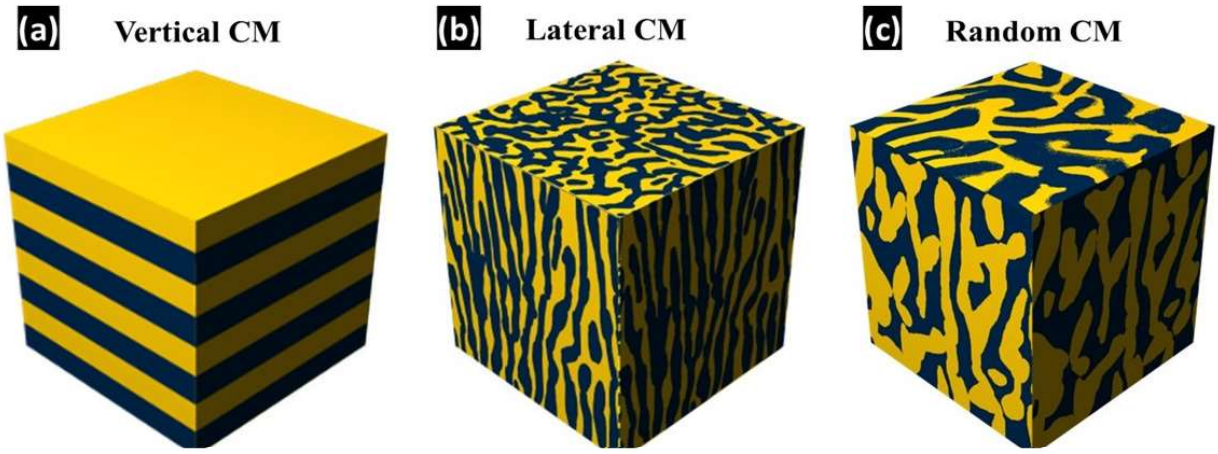

Figure 1.1 Schematics of nanocomposites with a vertical concentration modulation, b lateral concentration modulation and c random concentration modulation.

vertical laminate-like structure (Figure 1.1b), and random concentration modulation (RCM) with a bicontinuous intertwined 3-dimensional network (Figure 1.1c). Post annealing of co-deposited immiscible metals and liquid metal dealloying have been reported to generate MNC with such morphologies [15, 16]. However, the control of the nanostructure is very limited in these synthesis techniques and they both require complex processing steps. A one-step synthesis route to prepare nanocomposite by co-sputtering Cu and Mo at elevated temperatures to induce phase separation during deposition has been developed in our group [17]. To our knowledge, this is the first reported method that has the capability to produce any of the VCM, LCM or RCM structures and control the morphology down to a few nm. Each of the three CM configuration can be formed as a result of a competition between the rate of phase separation and material flux rate during deposition. The LCM structure is a result of the phase separation rate being much faster than the rate of material being added to the substrate. The first atoms to arrive on the surface fully separate and form concentration modulations only in the vertical direction before the next "layer" of material arrives, developing a template for the rest of the deposition. The later deposited adatoms of Cu and Mo atoms then diffuse along the surface to their respective domains on the template. Because of the slower deposition rate, newly deposited Cu and Mo atoms are always in contact with terminal

domains of Cu and Mo and so these lateral domains continue until deposition ceases. When the rate of phase separation is similar to the rate of deposition, VCM structure will form. The first layer of Cu and Mo added to the surface has not fully phase separated before the next layer arrives. Thus, as the Cu and Mo domains try to vertically develop as was the case for LCM, the fresh layer is absorbed into the first few deposited layers because these domains are not yet at terminal composition. The fresh layer just deposited then becomes depleted in Cu atoms in regions above initially formed Cu domains and vice-versa for Mo atoms (i.e. regions above initially formed Mo domains become Mo-lean). This consequently forms a checkerboard structure. Eventually, the checkerboard domains interconnect forming wave-like domains. Finally, complete Cu and Mo bands form into a VCM structure. This pattern can continue because if there is a Cu band on top that has yet to reach its terminal composition, fresh Cu atoms in the next layer deposited will be absorbed and thus become Cu-lean, or Mo-rich. The RCM case is the situation where bulk diffusion is non-negligible which can lead to interconnected domains.

Cu and Mo were selected as the model system because they have positive heat of mixing and thus high immiscibility even at elevated temperatures. Hence, the co-sputtering process produces phase-separated morphologies with no intermetallic or compound involved. Besides, Cu and Mo have a large disparity in mechanical properties, providing an adequate platform to study the effect of composite structures. By changing the deposition temperature and rate, ligament size, interface coherency and structural anisotropy of the nanocomposites can be tailored. In our design process, an LCM structure with coherent Cu/Mo interfaces was first tested and observed to have high strength but limited deformability. Then the Cu/Mo interface was changed to semi-coherent by raising the deposition temperature and thus the ligament size while keeping the LCM structure. Both high strength and appreciable deformability were achieved. However, the deformation was

localized through kink banding. With no substantial success from the LCM samples, RCM sample were made by further increasing the deposition temperature, in which a desirable combination of strength and deformability was obtained, which is unprecedented in similar material systems

4.2 Experimental

The multilayer nanocomposite was prepared by sequential deposition of 3 nm Cu and 3 nm Mo at room temperature until a film thickness of 1 μm. To make the LCM and RCM nanocomposite, Cu and Mo with nominally equiatomic composition were co-deposited onto thermally oxidized Si substrates by direct-current (DC) magnetron sputtering at 500 ^{o}C, 600^{o}C and 800 ^{o}C. The Si substrate was chosen because of its high hardness. Therefore, the substrate effect during the mechanical testing can be neglected. Confocally oriented 99.999% pure Cu and 99.95% pure Mo targets were used during deposition. The pressure prior to deposition was maintained below 2.7×10^{-7} Pa. The nominal deposition rate was held at 1.2 nm/s for each of the constituents until a final film thickness of approximately 1 μm was achieved. Scanning electron microscopy (SEM) characterization was conducted in a FEI Magellan 400 SEM. A double Cs-corrected JEOL3100R05 was used to perform transmission electron microscopy (TEM) and scanning TEM (STEM) characterization of the samples. Elastic moduli of the nanocomposites were measured from nanoindentation tests conducted using Hysitron TI 950 Triboindenter. Diamond Berkovich tip was used to make indentations to a depth of 150 nm. The average value from 25 indents was reported. Hysitron PI 85 and PI 95 Picoindenters were used as platforms to conduct nanopillar compression tests in the SEM and TEM respectively. The compression tests were performed using diamond flat-punch indenters in the displacement control mode to maintain a fixed strain rate of 2×10^{-3}/s. The TEM and nanopillar samples were prepared using focused ion beam (FIB) in FEI Helios Nanolab DualBeam SEM. To minimize FIB damage, the final beam current was used as 50

pA. At this current, minimal surface amorphization was detected in the TEM foils fabricated by FIB. Ion softening of the nanopillars was thus considered negligible in our study. During nanopillar fabrication process, the final thinning step was done within 300 ms to reduce 20 nm of the pillar diameter, minimizing the taper angle of the pillar to ~ 2.2^{o}. This small extent of tapering is inevitable in nanopillars fabricated by FIB and generally not considered a problem for crystalline materials [18]. Strain hardening would offset the effect of tapering that causes higher stress state at the top of the pillar. For each nanocomposite, at least four pillar compression tests were performed to ensure the reproducibility of the data. Representative stress-strain curves are reported in this article.

4.3 Results

4.3.1 Multilayer nanocomposite with mixed interfaces

The cross-sectional TEM image of the sample is shown in Figure 1.2a with the SADP in the inset indicating a Mo(110)//Cu(111)//interface fiber texture. Through fitting the electron diffraction intensity around Mo(110) and Cu(111) spots into Gaussian profiles, it could be estimated that more than 60% of Cu atoms take BCC structure, assuming the same texture effect for Cu and Mo. Figure 1.2b shows high-resolution-TEM image (left) and annular bright field atomic image (right) at two Cu/Mo interfaces. They indicate that Cu may exist as an FCC structure with Cu(111)//Mo(110)//interface or be coherent with the BCC Mo. The energy difference between BCC and FCC Cu is quite small, in a range of 7- 48 meV/atom based on first principles calculations [19, 20]. Therefore BCC Cu can be energetically favorable when it provides a better fit to the substrate lattice, until a critical thickness is reached where the energy gained from lattice fit becomes smaller than the increase of volume energy of the strained film [21]. The STEM image of the multilayer after 200 nm indentation is shown in Figure 1.2c. Mo appears brighter because

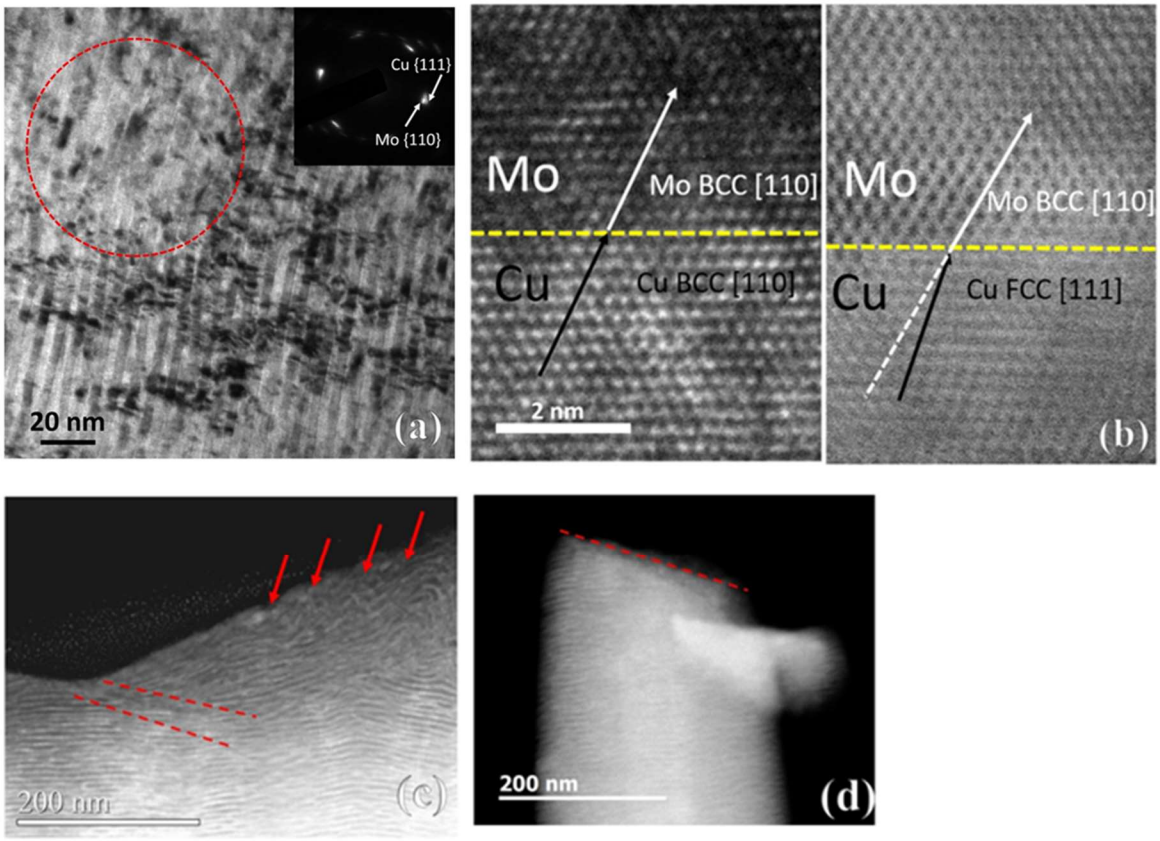

Figure 1.2 (a) TEM image of the Cu/Mo multilayer; inset: SADP of the circled area. (b) Atomic images showing Cu layer having BCC (left) and FCC (right) structures. (c) STEM image of indented multilayer. (d) STEM images of the top region of a multilayer nanopillar after the compression test.

of its higher z-number. A shear band is visibly emanating from near the tip of the indent, indicated by the dashed lines. Significant instability is observed, which can be traced down from the red arrows. The lack of deformability was also observed during nanopillar compression testing, the result of which is shown as the green curve in Figure 1.3. Only 2.5 % of plastic strain was recorded before the load drop, after a maximum flow stress of 2.8 GPa was reached. The STEM image of the pillar after the test in Figure 1.2d suggests that the load drop was due to the shearing of top region of the pillar along the dashed line.

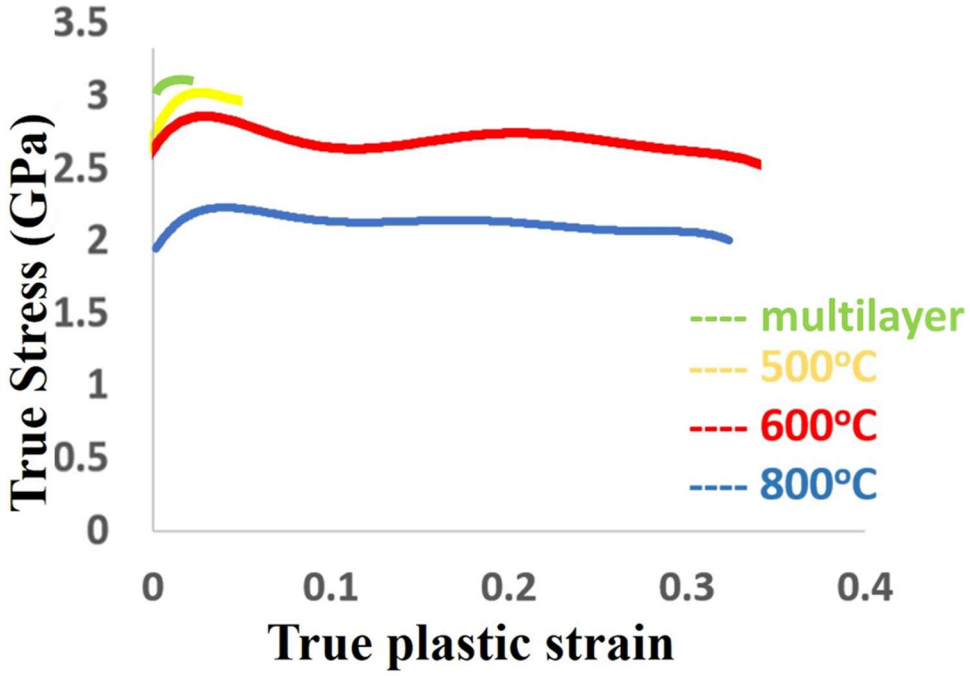

Figure 1.3 True stress-strain curved obtained from the nanopillar compression test.

4.3.2 LCM nanocomposite with coherent interfaces

To obtain a nanocomposite with an LCM structure and coherent interfaces, Cu and Mo were co-sputtered at 500°C with a rate of 1.2 nm for each material. Figure 1.4a shows the cross-sectional view annular dark-field STEM image of the sample, where the darker contrast shows Cu rich regions and brighter contrast shows Mo rich regions due to their difference in atomic number. Lateral concentration modulation can be observed with an average ligament width of ~ 2.5 nm, giving vertical laminate-like features. The inset is a corresponding selected area diffraction pattern (SADP). Diffraction spots only appear at Mo body-centered-cubic (BCC) positions, indicating that Cu takes the Mo BCC crystal structure. This is further confirmed in Figure 1.4b, which is an

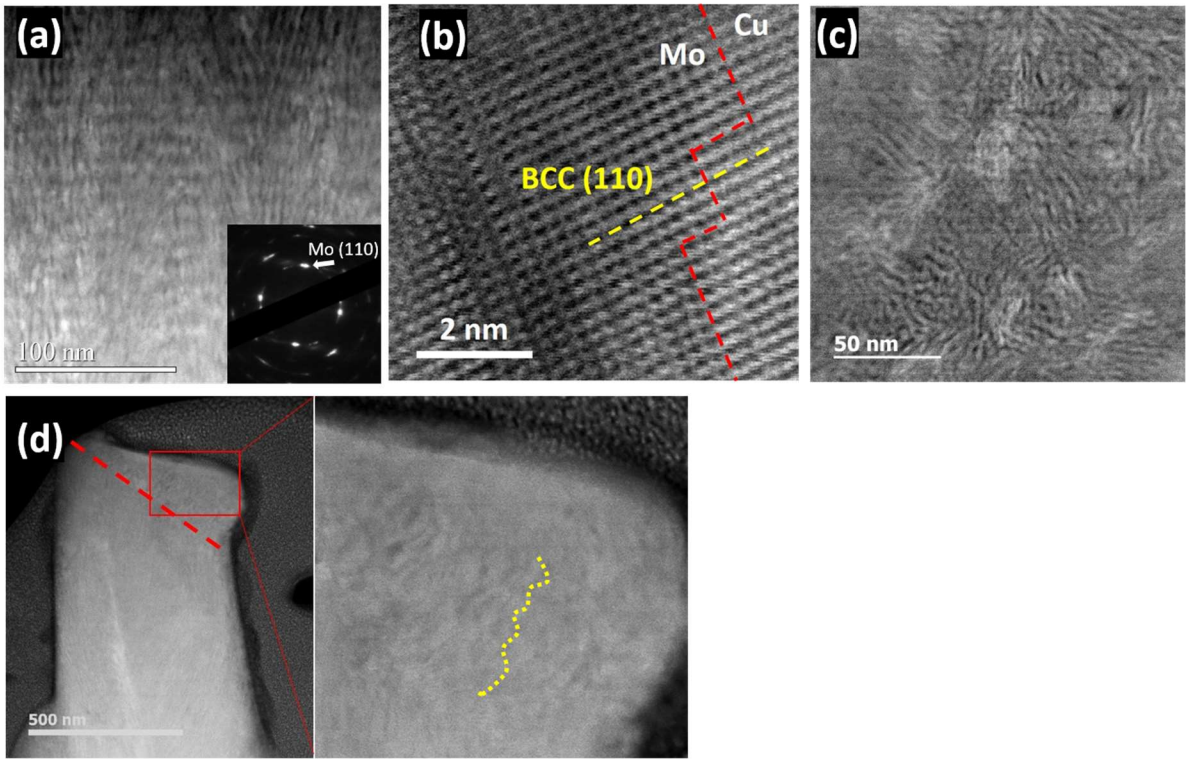

Figure 1.4 (a) cross-sectional STEM image of the coherent LCM nanocomposite, inset: SADP of the region; (b) atomic image across a coherent Cu/Mo interface; (c) plan-view STEM image of the sample; (d) STEM image of the nanopillar after compression test.

annular bright-field atomic image showing coherent Cu/Mo interfaces in the sample. From the spread of spots in the SADP, it can be deduced that the coherency only extends over a few to a few 10s of nm. When local strain energy is considered, BCC Cu is energetically preferable because it provides a better fit to the BCC Mo and the correlated formation energy only differs from that of face-centered-cubic (FCC) Cu by a small amount [20, 22]. With larger width of Cu ligaments, the volume free energy of the strained crystal increases and eventually surpasses the energy gained from the lattice fit, to a point where Cu will retain its FCC structure. Figure 1.4c is a plan-view STEM image of the sample, a bicontinuous interpenetrating morphology is present. Incorporating the cross-sectional and plan-view images, a 3-dimensional reconstruction of the morphology of the samples is similar to the schematic in Figure 1.1b.

The thin film nanocomposites were deposited to a thickness of 1 μm. The elastic modulus was measured as 202±14.7 GPa from the nanoindentation test. This value is slightly lower than the average modulus of bulk Cu and Mo at 230 GPa, which is expected because Cu is in BCC structure. To measure the stress-strain response, cylindrical nanopillars with an aspect ratio of approximately 2:1 were fabricated using FIB for compression tests. Using the load and displacement values recorded during the tests and assuming constant volume, true plastic stress-plastic strain data for the coherent LCM sample were calculated and plotted as the yellow curve in Figure 1.3a. The constant volume assumption for calculating true stress and strain only holds true during the initial strain hardening stage, before any localized deformation occurs. Nevertheless, the trend of the curves can be used to interpret deformation mechanism of the nanocomposites and the stress-strain values are useful to compare the mechanical performance of three nanocomposites, among themselves and with other nanocomposites in literature tested with similar methodology. Maximum flow stress of 3.2 GPa was measured in coherent LCM sample, followed by a sudden load drop. Localized deformation at top corner of the pillar was observed after the load drop and the test was then aborted. Figure 2d shows STEM image of the cross-section of the pillars after compression test. FIB was used to expose a thin slice in the middle of the pillars along the loading axis for following STEM characterization. The image shows that deformation in the coherent LCM sample was concentrated at the top corner of the pillars where the original vertical continuous layers became undulating in profile. A clear boundary can be identified between the deformed and undeformed regions, marked by the dotted line.

4.3.3 LCM nanocomposite with semi-coherent interfaces

Although the coherent LCM structure provides high strength, it is not ideal for promoting deformability. To change the interface coherency, the ligament size should be increased so that the

strained BCC Cu lattice would no longer be energetically favored. This was achieved by increasing the deposition temperature to 600ºC to bring up the phase separation rate while keeping the same deposition rate. Figure 1.5a shows a cross-sectional STEM image of the as-synthesized sample. LCM features were preserved while the ligament size increased to ~ 4 nm. The inset SADP shows both signals from FCC Cu and BCC Mo, indicating that Cu retained the FCC structure. Atomic image in Figure 1.5b shows a Kurdjumov-Sachs orientation relationship across the interface (indicated by the red dotted line), where Cu $(111)_{FCC}$//Mo$(110)_{BCC}$ and Cu $[10\bar{1}]_{FCC}$//Mo $[11\bar{1}]_{BCC}$.

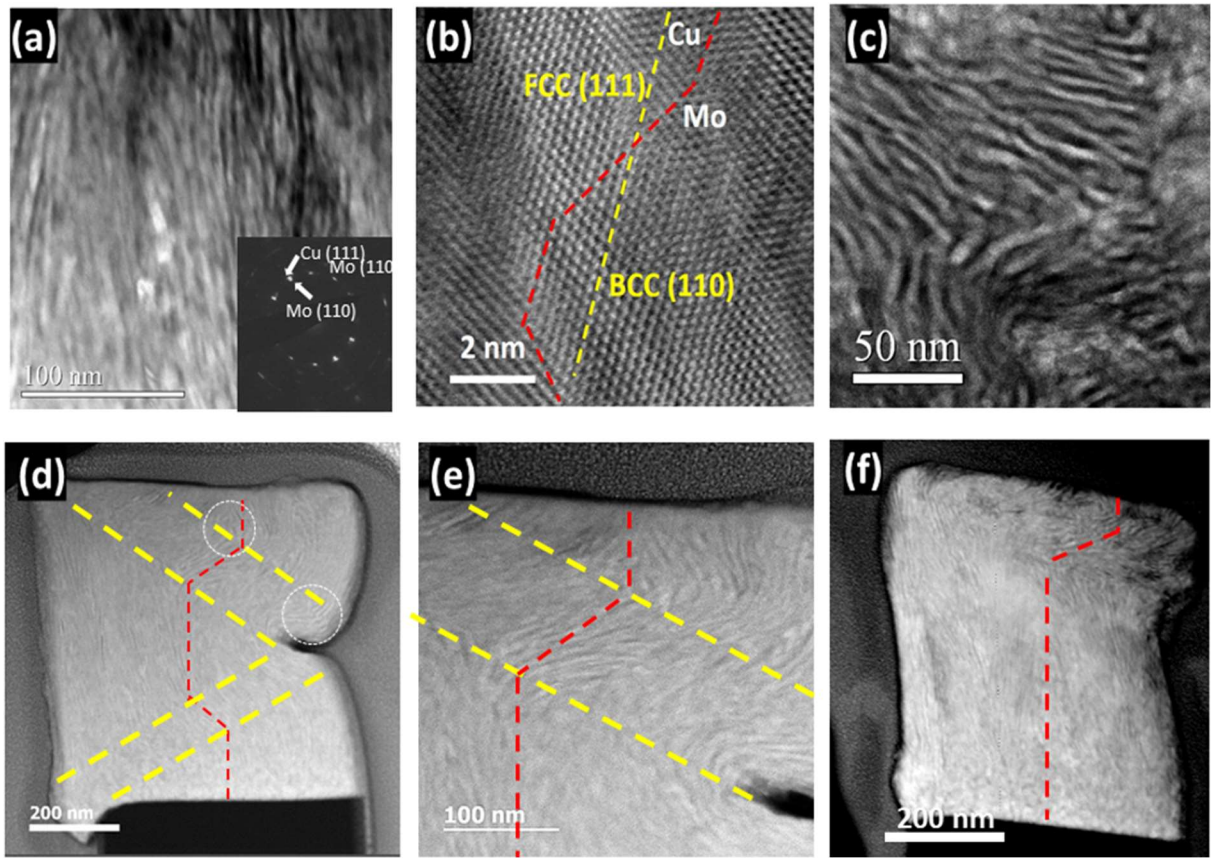

Figure 1.5 (a) cross-sectional STEM images of the semi-coherent LCM nanocomposite, inset: SADP of the region; (b) atomic image across a semi-coherent Cu/Mo interface; c plan-view STEM image of the sample; (d) STEM images of the nanopillar after 33% compression; (e) high magnification image showing the kink band at the top of the pillar and (f) STEM image of the nanopillar after 10 % compression.

Because of this crystallographic correlation, the Cu/Mo interfaces are semi-coherent rather than totally incoherent.

The Young's modulus of this nanocomposite was measured at 223 ± 15 GPa, in agreement with the rule of mixture which gives the average modulus of bulk Cu and Mo. The red curve in Figure 1.3 is measured from semi-coherent LCM sample. Two local maxima can be observed, where the first maximum is at stress of 2.9 GPa and the second at 2.7 GPa. The stress level maintained above 2.3 GPa till the end of the test where a total compression of 33% was achieved. Figure 1.5d shows an image of the sample after the compression test. The orientation of the ligaments can be traced by the red line. Indicated by the yellow lines, two bands are present within which the layer orientation changed cooperatively, which is symbolic for the formation of kink bands. A magnified image of the first band near the top surface of the sample can be found in Figure 1.5e, showing more clearly the change in orientation of the ligaments. The band width was measured at 195 nm and the layers rotated by 65°. The band width and layer rotation angle are 172 nm and 60° respectively for the lower band. The strain from the kinking can thus be calculated at 20%. Figure 3e shows a semi-coherent LCM pillar after 10% compression, the strain immediately passing the first maximum of the stress-strain curve. A single kink band emanating from the top corner of the pillar is observed.

4.3.4 RCM nanocomposite with semi-coherent interfaces

It has been shown that the deformation in either of the LCM nanocomposites is localized, although the semi-coherent sample demonstrated appreciable deformability. Our final answer might lie within the RCM structure, which is achieved by further increasing the deposition temperature to 800°C. Promoted bulk diffusion which could be neglected at lower temperatures connects the Cu/Mo ligaments, producing a bicontinuous interpenetrating structure. The

bicontinuous phases with ligament size ~ 15 nm can be observed in Figure 1.6a, which is a cross-sectional STEM image of the sample. The inset SADP and Figure 1.6b, an atomic image of the interface, show the semi-coherent nature of the interfaces, also with a Kurdjumov-Sachs orientation relationship. Incorporating the cross-sectional image and the plan-view image in Figure 1.6c, 3-dimensional reconstruction of the structure of the nanocomposite can be found to be the same as Figure 1.1c. Nanoindentation on this sample gives an elastic modulus at 204±19 GPa,

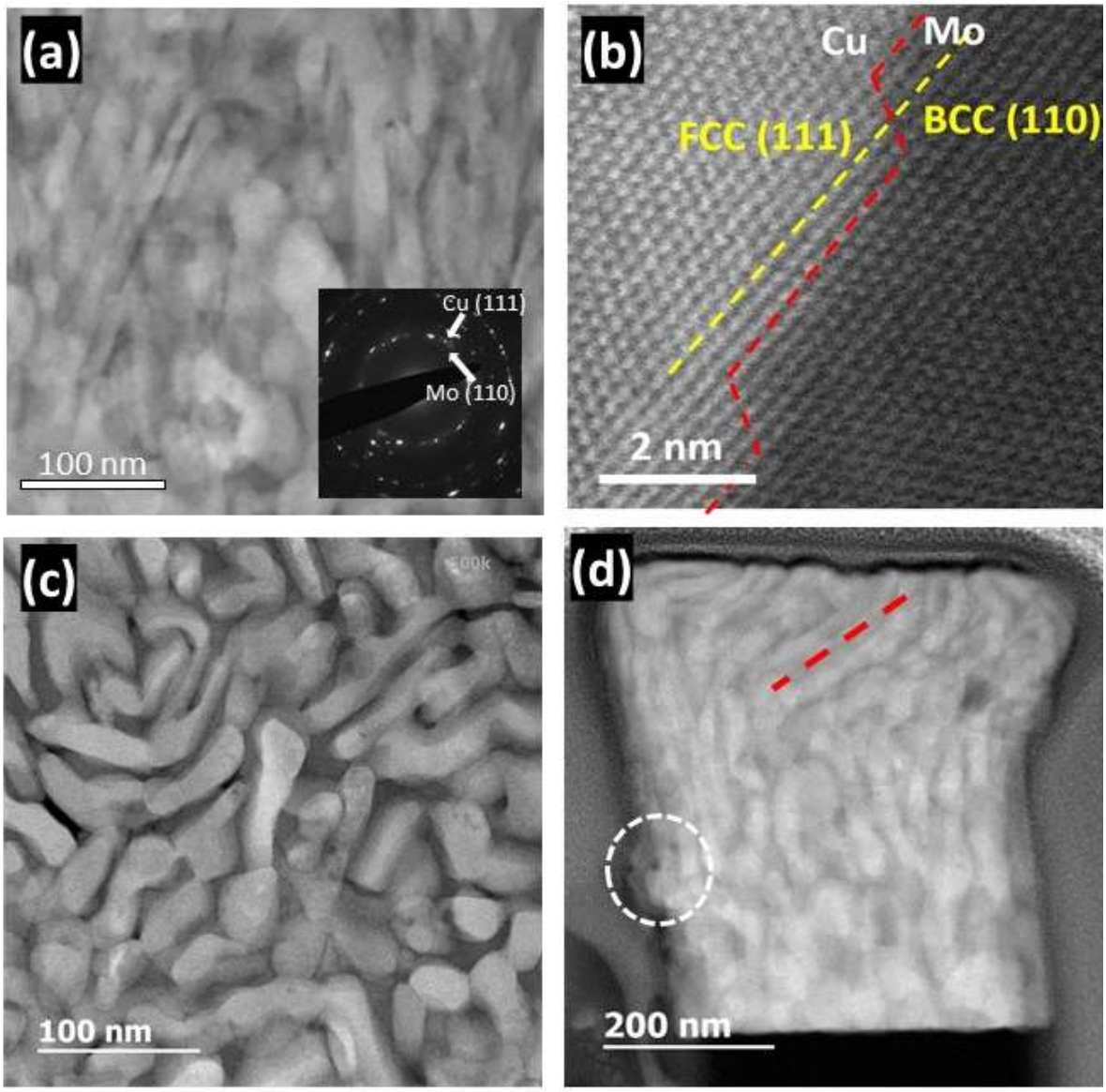

Figure 1.6 STEM images (a) cross-sectional view of the semi-coherent RCM nanocomposite, inset: SADP of the region; (b) atomic image across a semi-coherent Cu/Mo interface; (c) plan-view of the sample; (d) nanopillar compression test.

which is slightly lower than the average modulus of Cu and Mo. One reason is that the surface roughness of this nanocomposite is measured at 39 nm, higher than that measured for the other two nanocomposites, which affects the accuracy of the modulus measurement. The blue curve in Figure 1.3a corresponds to the stress-strain response of the RCM sample, where the peak flow stress was measured at 2.4 GPa. A slight decrease in stress follows and then a stable near-flat curve above 2.2 GPa is observed till the end of the test at 31% plastic strain. STEM image of the RCM sample after nanopillar compression test can be found in Figure 1.6d. A rather uniform deformation can be observed at the bottom ¾ of the pillar, where a 15% increase in diameter was measured. At top of the pillar, where some LCM feature can be probed, strain localization in a kink-like form indicated by the red dotted lines gives a mushroom-like shape of the pillar. From the above iterative process, the bicontinuous interpenetrating structure and semi-coherent interfaces is found to be the optimal design of MNC with high strength and enhanced deformability.

4.4 Discussion

4.4.1 Shear banding in the multilayer

An extremely high strength is recorded for the multilayer, which can be explained by the length-scale-dependent deformation discussed previously. At 3 nm layer thickness, dislocations cutting through the interface is supposed to be the dominant deformation event. As demonstrated in Figure 1.7a (left), once the critical stress is reached, multiple dislocation would glide across the interfaces especially for the coherent interfaces, forming shear bands like the ones indicated by red arrows in Figure 1.2c. The other type of shear band shown between the dotted lines in Figure 1.2c can be explained by a process depicted in Figure 1.7a (right), which has been discussed in the Cu/Nb system.[23] Because the FCC Cu/BCC Mo interface is weak in shear, the interface is susceptible to slip when there is a load component along the interface. When the indenter is pressed

into the multilayer, it causes stress concentration and rotation of the layers. Hence the rotated interface is loaded in shear and slip on the interface plane will be favoured over intralayer slip. Continued shear along the interface leads to the onset of shear banding.

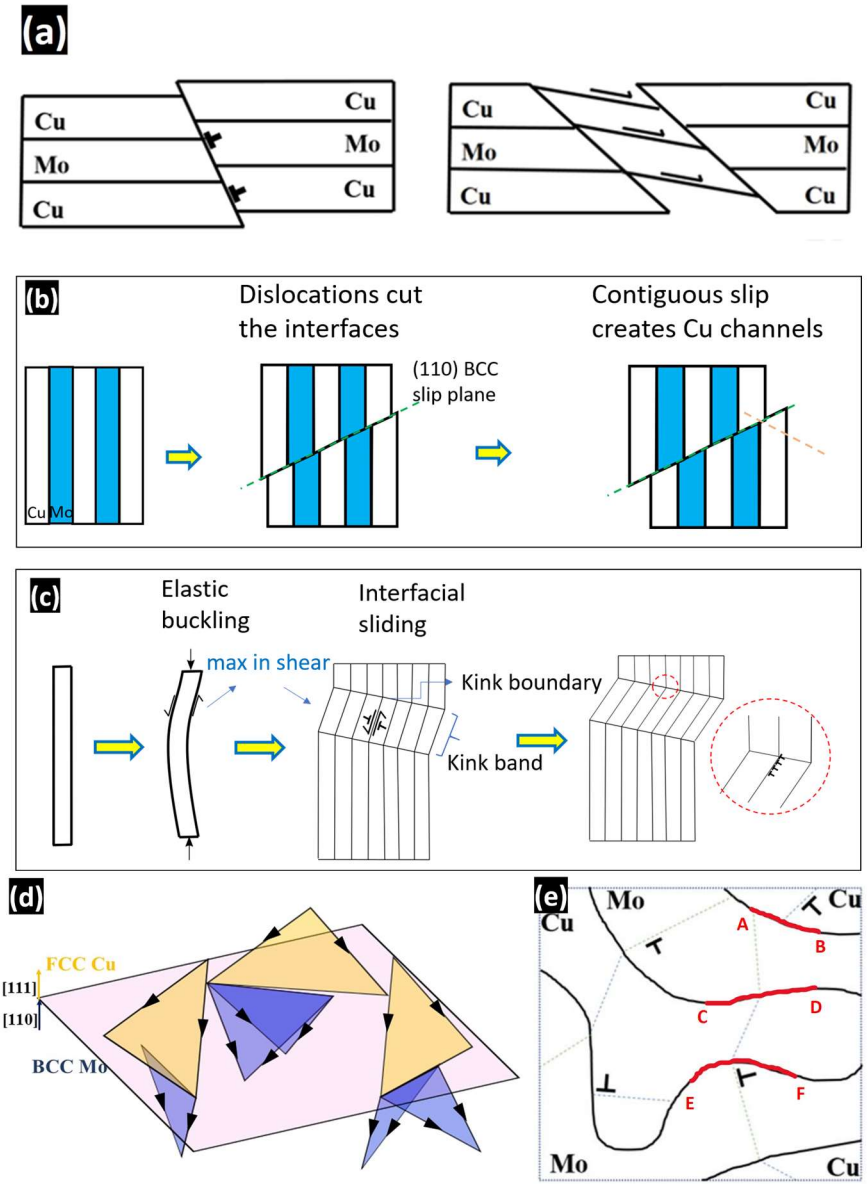

Figure 1.7 Schematics showing (a) formation of shear band in the multilayer from dislocations cutting the interface, (b) localized shearing semi-coherent LCM structure, (c) kink band formation in semi-coherent LCM structure, (d) slip systems in two metals have K-S OR and (e) deformation events in a semi-coherent RCM structure.

4.4.2 Strain localization in the coherent LCM nanocomposite

The LCM nanocomposite with coherent interfaces has high strength but limited deformability due to shear localization. The maximum flow stress measured is comparable to the 2.8 GPa value measured in Cu/Mo multilayer with similar feature size (3 nm) [24]. Although deformation is highly localized in the coherent nanocomposites, the load drop is more gradual than the catastrophic fracture in the 3 nm multilayer. Apart from the layered structure, another contributing factor to the failure proneness of the 3 nm Cu/Mo multilayer is the presence of both coherent and semi-coherent interfaces in the system [24]. In the coherent LCM sample, due to the local coherency of BCC Cu and BCC Mo, continuity of slip system exists across interfaces. As depicted in Figure 1.7b, the dislocations can move along the common (110) slip plane across two layers without structural hindrance. The coherency stress between Cu and Mo, however, sets barrier for the transmission of dislocations across the interfaces. With each dislocation cutting through the interface, a step will be created. Multiple transmission of dislocations along the same plane will lead to the undulating structure observed in Figure 1.4b. The offset of Cu ligament will effectively double the ligament size and thus provide easy channels for dislocation movement. Consequently, strain softening and strain localization will take place, similar to the situation in the coherent Al/Al_3Sc system [25]. Through theoretical studies, the equilibrium lattice parameter of BCC Cu has been estimated to be ~ 2.9 Å [22, 26]. The lattice mismatch between BCC Mo and BCC Cu can be calculated as 8.5%. Misfit dislocations are expected to be present at the interface, similar to the situation of Cu/Ag system where the lattice mismatch is 12% [27]. While releasing part of the coherency stress, the misfit dislocations may form a network, blocking the slip transmission across the interfaces. As evidence of misfit dislocations was not encountered during our TEM characterizations, the nomenclature “coherent interface” was kept throughout this article.

4.4.3 Kink banding in the semi-coherent LCM nanocomposite

The LCM nanocomposite with semi-coherent interfaces exhibits high strength and extended plasticity during the compression test. However, the deformation is localized in kink bands. Similar kink band formation has also been reported in uniaxial fiber composites, nanolaminates and ceramic ternary carbide “MAX" phases, which all have strong anisotropy in structure and plasticity. [28-30] More specifically, shear along one set of slip planes in these materials requires lower stress than along the others. For example, MAX phases have layered atomic structure with alternating $M_{n+1}X_n$ and A, where M is a transition metal, A is a Group IIIA or IVA element and X is C or N. The MX/A interfaces are parallel to the basal plane, which is the slip plane in the MAX phases. Collective slip of dislocation along the parallel basal planes accounts for the kink band formation when a compressive load is parallel to the layers [31]. A similar process explains the kink bands observed in the semi-coherent LCM sample.

Atomistic modeling of a FCC/BCC system with K-S OR revealed that while keeping the lattice misfit strain constant, the critical stress for interface shear decreases with increasing heat of mixing [32]. Cu/Mo has a positive heat of mixing of +19 kJ/mol, which is significantly higher than that of Cu/Nb (+3 kJ/mol), the interface of which is known to be weak in shear. Therefore, it is reasonable to assume that slip along the Cu/Mo interface requires lower shear stress than slip in Cu and Mo nanophases confined by interfaces, although Cu/Mo has a lower lattice misfit of 6.4% compared to that of Cu/Nb at 11.2% [33]. (The lattice misfit in this case is measured along <110>FCC//<111>BCC in the parallel (111)FCC/(110)BCC plane.) In other words, when there is a non-zero resolved stress at the interface, dislocation glide along the interfaces can be activated. As a load is applied parallel to the interfaces during the compression test, elastic buckling induces shear stress to part of the interfaces, as demonstrated in Figure 1.7c. Under this shear stress,

dislocation slip along the interfaces will be triggered, leading to sliding between layers. Interfacial sliding results in rotation of a band of layers to the same orientation. The dislocations stop at the boundaries of the kink bands where the tilted layers meet the vertical layers, marked by the yellow lines in Figure 1.5d. Rotation of the layers increases the Schmid factor along the interfaces, facilitating interfacial sliding, which accounts for the drop of stress level in Figure 1.3 after the first maximum. Meanwhile, increase in dislocation density at the kink band boundaries poses difficulty to further interfacial slip. With more dislocations pile up against the KB boundary, higher stress is thus required for further kinking, which explains the second rise in stress level until another KB is triggered after the second maximum on the stress-strain curve. Although KB is a form of strain localization, this self-lockup mechanism renders it a non-catastrophic deformation behavior. In contrast, once a shear band is formed, further deformation will all be localized in the band.

Based on the geometry of the kink bands, about 20% change in pillar height can be attributed to the kinking. The other 13% of the total 33% compression can be ascribed to two sources. First is the dislocation glide along the Cu/Mo ligaments. Confined layer slip within the the 4 nm thick layers gives rise to uniform thickening of the ligaments and an initial strain hardening of the material. Due to the relative large variance in ligament width in the co-sputtered nanocomposite compared to a well-defined multilayer system, the measured ligament width cannot provide statistically valid support of ligament thickening during the test. Another contributing factor to the strain is that at the kink boundary, unlike a sharp change in laminate orientation observed in nanolaminate structures, wavy traces can be found in our nanocomposites, circled in Figure 1.6d [34]. This can be explained by the planar discontinuity of the nanocomposite. The irregularity at the cross section of the nanopillar pose geometric hindrance to the cooperative layer

sliding. Therefore, ligaments around the kink boundaries must re-arrange themselves to accommodate the kinking, resulting in the wavy structure. Due to the waviness of the layers, the 20 % strain from kinking is undervalued. Limited by the size of the nanopillars used for testing, intersection of kink bands was not observed. Instead the two kink bands in Figure 4.5d rendered a morphology very similar to creasing, which is normally observed in elastomeric materials [35]. Although the formation mechanisms are distinctly different, it is remarkable that a representative phenomenon of soft materials can be discovered in a metallic material.

4.4.4 Enhanced deformability in the semi-coherent RCM nanocomposite

The RCM nanocomposites with semi-coherent interfaces shows a better combination of high strength and plastic deformability, which is implied by the near flat stress-strain curve after peak stress. Figure 1.7d shows the slip systems in FCC Cu and BCC Mo with K-S OR when the interface plane is Cu (111) // Mo (110). It can be seen that one set of Cu (111) plane and Mo (110) plane intercept with the interface along the same trace. This provides a path for the dislocations to move between Cu and Mo when the interface is the slip plane for both phases. Because of the slight change in the angle of the slip planes and the difference in Burgers vectors of Cu and Mo, a dislocation will be left at the interface after a glide dislocation passes the interface [36]. As discussed previously, the Cu/Mo interface is weak in shear and thus serves as a sink to approaching dislocations and high stress is required to produce a dislocation at the other side of the interface [37]. Transmission of dislocation across a Cu/Mo interface is thus very difficult, requiring very high stress level. Therefore, the Cu/Mo interfaces serve as effective barrier to dislocation movement, giving high strength to the nanocomposite. The 2.4 GPa maximum flow stress in the semi-coherent RCM nanocomposite is only slightly lower than the 2.8 GPa measured in 5 nm Cu(FCC)/Mo(BCC) multilayer [38]. This difference in stress level is expected as the ligament size

of the nanocomposite is larger than the 5 nm layer thickness. Previous studies on multilayer structures show that at 15 nm length scale, confined layer slip (CLS) accounts for the major deformation mechanism. Using CLS model, the applied shear stress to propagate a glide loop, τ_{cls}, can be calculated as

$$\tau_{cls} = \frac{\mu b^2}{8\pi h}\left(\frac{4-\nu}{1-\nu}\right)\left[ln\frac{\alpha h}{b}\right] \quad (1)$$

where μ is the shear modulus, b is the length of the Burgers vector, h is the individual layer thickness, ν is the Poisson's ratio and α represents the dislocation core cutoff parameter [39]. Low value of α would imply a wide dislocation core. Substituting μ = 48 GPa, b = 0.25 nm, b = 0.147 nm, (as calculated for 1/6<112> vectors with lattice parameter 0.361 nm) ν = 0.3 for Cu and using α = 1 for compact core, τ_{cls-Cu} can be calculated as 0.69 GPa for h_{Cu} = 15 nm. The yield strength of Cu ligaments, σ_{cls-} can be estimated by multiplying τ_{cls-Cu} with the Taylor factor of 3.1, which gives 2.14 GPa. Using μ = 120 GPa, b = 0.273 nm (1/2<111>) and ν = 0.32 for Mo, σ_{cls-Mo} is estimated at 5.65 GPa, which far exceeds the measured yield strength of the nanocomposite. From these calculations, it can be postulated that, plastic deformation of Cu ligaments takes account for most of the yielding of the nanocomposite, while the higher-strength Mo ligaments constrain the deformation of Cu and strengthen the nanocomposite.

A relatively uniform distribution of deformation is observed in the lower portion of the nanopillar in Figure 1.6e. The interpenetrating phases provide geometric advantages on preventing strain localization for several reasons. Previous research on Cu/Nb multilayer nanocomposites has shown that, when a compressive load is applied along an axis perpendicular to the interfaces, shear banding in such systems stems from collective rotation of the interfaces [23]. Due to the regulated multilayer structure, rotation of the interfaces could be easily passed on to adjacent layers.

Preferred slip along the interfaces that are weak in shear then causes strain localization. In our Cu/Mo system, which is similar to Cu/Nb as both material systems have FCC/BCC semi-coherent interfaces and positive heat of mixing, presumably shear band is also initiated from interfacial slip. Due to the tortuous topography of the interfaces, slip along interface plane would only advance short distances before it encounters the Cu or Mo phases, where the Burgers vector must change in magnitude and oftentimes in direction. Accordingly, the shear cannot propagate along the same direction for extended distance, which is the source of strain localization. Shear localization caused by interfacial slip can explain the abnormality circled in Figure 1.6e. At the surface of the nanopillar, where the Cu/Mo ligaments have access to free space, interfacial sliding occurred in an unconstrained manner, causing a small amount of local extrusion. Another effect from the tortuosity of the interfaces is that, interface segments parted by Cu/Mo ligaments are not in the same geometric environment, such as segment AB, CD and EF in Figure 1.7e. These segments would not affect each other like the parallel interfaces in multilayer systems do, where the rotation of one interface segment would trigger the rotation of the segment beneath it. Therefore, the cooperative rotation of interfaces observed in multilayers is not likely to take place in the bicontinuous structure. The abundance of interface segments in various orientations also contributes to the strain de-localization of the materials by providing a profusion of sites prone to shear band formation. Experience from metallic glass, which deform through localized shear band and normally lacks deformability, has revealed that, with a low shear modulus, or in other words, ease of shear band formation, large-scale plasticity can be achieved through the generation of multiple shear bands [40]. The metallic glass systems have also demonstrated effectiveness of a bicontinuous structure to suppress shear band propagation. It has been reported that a Mg based metallic glass, which fails easily under compression, achieved significant improvement in strength

and deformability when it forms an interpenetrating phase composite with Ti. The interpenetrating structure was proposed to contain shear bands and promote homogeneous distribution of shear in the glass phase.

To better understand the deformation of the semi-coherent RCM structure, my collaborator, Nathan Beets and Prof. Diana Farkas from Virginia Polytechnic Institute and State University helped to conduct atomistic simulation on compression of a Cu-Mo RCM nanocompsite. The LAMMPS software package developed by Steve Plimpton [41] was used to carry out all the molecular dynamics simulations. The EAM (Embedded Atom Method) potential developed by Gong *et al*. was used to model the atomic interaction in the copper-molybdenum system [42, 43]. Visualization, dislocation analysis, and stress analysis were performed through the use of OVITO, developed by Alex Stukowski [44-48] [49]. A phase field scheme based on the Cahn-Hilliard formalism to create an interconnected two phase structure to generate the RCM structure, which is shown in Figure 1.8a [50]. The samples were deformed uniaxially in compression using the isothermal–isobaric (NPT) ensemble, while trans-axial sides were allowed to expand to account for the elastic and plastic Poisson effect. Visualization of defects was performed using OVITO [41], which included the analysis of dislocations by the DXA dislocation extraction formalism [41] and analysis of volume and surface area relationships via the surface mesh formalism [51].

The simulated stress-strain curve is shown in Figure 1.8b, which gives a yield strength of 2.53 GPa for 15 nm ligaments, agreeing with the experimentally measured value of 2.2 GPa. Figure 1.8c plots the simulated stress evolution separated by atom type for Cu and Mo. From these curves, the deformation of the composite can be broken up into three stages, defined by yielding of the separated components. In stage I, from the start of the deformation, both components deform

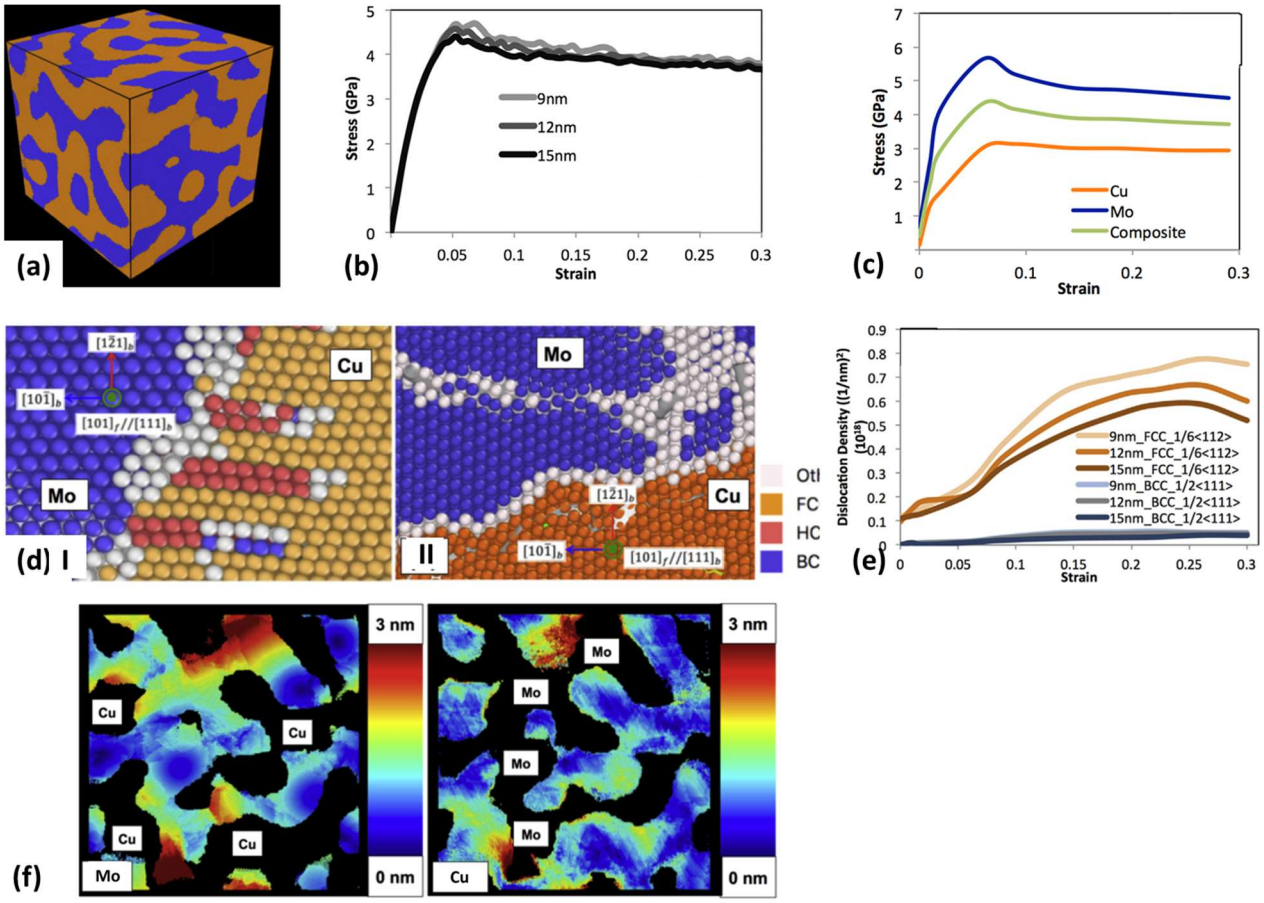

Figure 1.8 (a) Image of the computational sample with 15 nm ligament diameter, (b) stress-strain curves obtained from simulations, (c) stress evolution in each phase, (d) emission of dislocation into the Cu phase during simulation, (e) evolution of residual dislocation density during the compression test, (f) non-uniform displacement maps obtained from the Mo and Cu phases respectively.

elastically, up to 0.03 strain. The ratio of the load in the two phases (σ_{Mo}/σ_{Cu}) is 2.24, close to the ratio of directional elastic moduli of the phases at 2.12. In stage II, the copper starts to yield at a strain of approximately 0.023, while the molybdenum still deforms elastically. Finally, in stage III, beginning at a strain of around 0.05, both components deform plastically.

Dislocations nucleating from the interfaces are found to be the main mechanism of plastic deformation in both the Cu and Mo phases. As depicted in Figure 1.8d, the dislocations in the Cu phase were identified to be Shockley partials that create stacking faults in the Cu lattice. While trailing partials are seen to come out in some cases, they often occur later in the deformation,

leaving a stacking fault behind for much of the deformation. Trailing partials often emerge at about 0.03 additional strain after nucleation of the leading partial. Due to entanglement and the interaction with other stacking faults, they often do not completely eliminate the stacking faults created by the leading partials. These dislocations travel through the Cu up to the neighboring interface, and are not transmitted to the Mo. Figure 1.8e is a plot of residual dislocation density in Cu and Mo phase separately. It can be observed that after yielding, the residual dislocation density in Cu phase increases drastically while there are only modest dislocation activities in Mo. This is expected as Mo has higher yield strength compared to Cu. When Cu starts to yield, Mo is still deforming elastically. A situation of mechanical incompatibility between the constituent phases of the composite is created. Because of the constraint from the Mo phase, Cu cannot plastically deform freely. Strain gradient would then be generated near the Cu/Mo interface. Geometrically necessary dislocations need be generated in Cu to accommodate this strain gradient, making Cu appear stronger. As a result, a synergetic strengthening of the intertwined phases takes place and increases the overall yield strength of the nanocomposite.

The atom-by atom non-uniform displacement, defined as the atomic displacements minus the uniform deformation of the lattice, was also analyzed, generating a non-uniform displacement map in Figure 1.8f. In the FCC phase, dislocations tangle and encounter stacking faults, causing them to change direction, or be stopped in the interior of the ligaments; whereas in the BCC phase, displacement gradients are gradual, and dislocation paths can be seen in the displacement map. Dislocations glide freely from one interface to another within the ligament. No shear band across the whole sample is observed, agreeing with the experimental result. Any shear bands that may try to form in the lattice under strain are arrested by the interface, and the complex morphology ensures that any observed shearing behavior is kept as ligament-by-ligament phenomena localized

to the ligament on which they occur, and uncoordinated with other shear events in other ligaments. In fact both parts of the lattice deform together, with total atomic non-uniform displacements rarely going above 3 nm, even after a 30% compressive deformation, without comprising the overall morphology of the sample and generating voids at the interfaces.

Cooperating the experimental and simulation results, improved plasticity of the RCM, or bicontinuous intertwined nanostructure can be explained by the following factors. First of all, the Cu/Mo interface acts as a strong barrier to dislocations. Dislocation slip in Cu would not cross the interface and enter the Mo phase, and vice versa. Therefore, there is little probability for a single slip event to transmit through the whole sample and lead to strain localization. As shown in Figure 4.8f, discrete regions where a number of dislocations have passed through can be observed in Mo phase. These regions can be between 2 and 5 lattice parameters wide, and span the width of a ligament. These are only seen in the Mo lattice, creating discrete segments that are more deformed than the lattice around them. However, as the slip is not continuous across the interface, this phenomenon of localized strain is not observed in Cu. As a result, shear band across multiple ligaments are not generated. Another factor is the large disparity in the mechanical properties of Cu and Mo, especially elastic modulus and yield strength. This is the reason the strain gradient is created and promotes high strain hardening in Cu, evidenced by the entanglement of stacking faults. An analogy can be drawn between our system to a heterogeneous material, e.g., dual phase steels, which have been shown to have extraordinary work hardening and high ductility [52]. Last and probably most important factor is the bicontinuous intertwined morphology, which provides geometric constraint between the two phases. Further, the abundance of interface dislocation sources and their tortuous shape provide multiple sites for dislocation nucleation and arrestment.

This promotes the wide spread of dislocation activities in Cu and less probability of shear band propagation.

4.5 Conclusions

Our work has shown that the stress-strain response of a metallic nanocomposite can be tailored by manipulating its structure at nanoscale. With the aim to design a structure for metallic nanocomposites that will achieve both high strength and plastic deformability, a 3 nm Cu/ 3 nm Mo multilayer and three nanocomposites with bicontinuous morphologies have been examined. The nanocomposites were fabricated with our newly developed co-sputtering at elevated temperatures approach, which provides control of morphology with feature size down to a few nm. The three nanocomposites all have high strength above 2 GPa. However, the one with coherent Cu_{BCC}/Mo_{BCC} interfaces lacks deformability due to localized shearing, whereas the one with lateral modulated Cu_{FCC}/Mo_{BCC} shows enhanced plasticity under compression via a proposed "self-locked" kinking mechanism. A three-dimensional nanoscale bicontinuous morphology with semi-coherent interfaces exhibits high plastic deformability due to the ability of the structure to de-localize deformation. Our work could provide insights on morphological design of high-strength nanocomposites that have enhanced deformability.

4.6 References

1. Lu, L., Shen, Y., Chen, X., Qian, L., & Lu, K., *Ultrahigh strength and high electrical conductivity in copper.* Science, 2004. **304**(5669): p. 422-426.
2. Lu, L., Chen, X., Huang, X., & Lu, K., *Revealing the maximum strength in nanotwinned copper.* Science, 2009. **323**(5914): p. 607-610.
3. Wei, Y., Li, Y., Zhu, L., Liu, Y., Lei, X., Wang, G., Wu, Y., Mi, Z., Liu, J., Wang, H. and Gao, H., *Evading the strength–ductility trade-off dilemma in steel through gradient hierarchical nanotwins.* Nature communications, 2014. **5**: p. 3580.
4. Wang, Y., Chen, M., Zhou, F., & Ma, E. , *High tensile ductility in a nanostructured metal.* Nature, 2002. **419**: p. 912.
5. Zhao, Y., Topping, T., Bingert, J.F., Thornton, J.J., Dangelewicz, A.M., Li, Y., Liu, W., Zhu, Y., Zhou, Y. and Lavernia, E.J., *High Tensile Ductility and Strength in Bulk Nanostructured Nickel.* Advanced Materials, 2008. **20**(16): p. 3028-3033.
6. Fang, T. H., Li, W. L., Tao, N. R., & Lu, K. , *Revealing extraordinary intrinsic tensile plasticity in gradient nano-grained copper.* Science, 2011. **331**(6024): p. 1587-1590.
7. Liddicoat, P.V., Liao, X.Z., Zhao, Y., Zhu, Y., Murashkin, M.Y., Lavernia, E.J., Valiev, R.Z. and Ringer, S.P., *Nanostructural hierarchy increases the strength of aluminium alloys.* Nature Communications, 2010. **1**: p. 63.
8. Jang, D. and J.R. Greer, *Transition from a strong-yet-brittle to a stronger-and-ductile state by size reduction of metallic glasses.* Nature Materials, 2010. **9**: p. 215.
9. Clemens, B.M., H. Kung, and S.A. Barnett, *Structure and Strength of Multilayers.* MRS Bulletin, 1999. **24**(2): p. 20-26.
10. Anderson, P.M., T. Foecke, and P.M. Hazzledine, *Dislocation-Based Deformation Mechanisms in Metallic Nanolaminates.* MRS Bulletin, 1999. **24**(2): p. 27-33.
11. Misra, A., J.P. Hirth, and H. Kung, *Single-dislocation-based strengthening mechanisms in nanoscale metallic multilayers.* Philosophical Magazine A, 2002. **82**(16): p. 2935-2951.
12. Misra, A., J. Hirth, and R. Hoagland, *Length-scale-dependent deformation mechanisms in incoherent metallic multilayered composites.* Acta materialia, 2005. **53**(18): p. 4817-4824.
13. Li, Y. P., Zhu, X. F., Zhang, G. P., Tan, J., Wang, W., & Wu, B., *Investigation of deformation instability of Au/Cu multilayers by indentation.* Philosophical Magazine, 2010. **90**(22): p. 3049-3067.
14. Han, S.M., M.A. Phillips, and W.D. Nix, *Study of strain softening behavior of Al–Al 3 Sc multilayers using microcompression testing.* Acta Materialia, 2009. **57**(15): p. 4473-4490.
15. Geslin, P. A., McCue, I., Gaskey, B., Erlebacher, J., & Karma, A. , *Topology-generating interfacial pattern formation during liquid metal dealloying.* Nature communications, 2015. **6**: p. 8887.
16. Vüllers, F.T.N. and R. Spolenak, *From solid solutions to fully phase separated interpenetrating networks in sputter deposited "immiscible" W–Cu thin films.* Acta Materialia, 2015. **99**: p. 213-227.
17. Derby, B., Cui, Y., Baldwin, J. K., & Misra, A. , *Effects of substrate temperature and deposition rate on the phase separated morphology of co-sputtered, Cu-Mo thin films.* Thin Solid Films, 2018. **647**: p. 50-56.
18. Chen, C.Q., Y.T. Pei, and J.T.M. De Hosson, *Effects of size on the mechanical response of metallic glasses investigated through in situ TEM bending and compression experiments.*

Acta Materialia, 2010. **58**(1): p. 189-200.
19. Lu, Z.W., S.H. Wei, and A. Zunger, *Absence of volume metastability in bcc copper.* Physical Review B, 1990. **41**(5): p. 2699-2703.
20. Kraft, T., Marcus, P. M., Methfessel, M., & Scheffler, M., *Elastic constants of Cu and the instability of its bcc structure.* Physical Review B, 1993. **48**(9): p. 5886-5890.
21. Wormeester, H., E. Hüger, and E. Bauer, *hcp and bcc Cu and Pd Films.* Physical Review Letters, 1996. **77**(8): p. 1540-1543.
22. Lu, Z., S.-H. Wei, and A. Zunger, *Absence of volume metastability in bcc copper.* Physical Review B, 1990. **41**(5): p. 2699.
23. Mara, N. A., Bhattacharyya, D., Hirth, J. P., Dickerson, P., & Misra, A. , *Mechanism for shear banding in nanolayered composites.* Applied Physics Letters, 2010. **97**(2): p. 021909.
24. Cui, Y., Derby, B., Li, N., Mara, N. A., & Misra, A., *Suppression of shear banding in high-strength Cu/Mo nanocomposites with hierarchical bicontinuous intertwined structures.* Materials Research Letters, 2018. **6**(3): p. 184-190.
25. Han, S.M., M.A. Phillips, and W.D. Nix, *Study of strain softening behavior of Al–Al3Sc multilayers using microcompression testing.* Acta Materialia, 2009. **57**(15): p. 4473-4490.
26. Tang, Z., Hasegawa, M., Nagai, Y. and Saito, M., *Density functional study on metastable bcc copper: Electronic structure and momentum density of positron-electron pairs.* Physical Review B, 2002. **65**(19): p. 195108.
27. Hoagland, R. G., Mitchell, T. E., Hirth, J. P., & Kung, H., *On the strengthening effects of interfaces in multilayer fcc metallic composites.* Philosophical Magazine A, 2002. **82**(4): p. 643-664.
28. Moran, P.M., X.H. Liu, and C.F. Shih, *Kink band formation and band broadening in fiber composites under compressive loading.* Acta Metallurgica et Materialia, 1995. **43**(8): p. 2943-2958.
29. Barsoum, M.W. and M. Radovic, *Elastic and mechanical properties of the MAX phases.* Annual review of materials research, 2011. **41**: p. 195-227.
30. Nizolek, T. J., Begley, M. R., McCabe, R. J., Avallone, J. T., Mara, N. A., Beyerlein, I. J., & Pollock, T. M. , *Strain fields induced by kink band propagation in cu-nb nanolaminate composites.* Acta Materialia, 2017. **133**: p. 303-315.
31. Barsoum, M.W. and T. El-Raghy, *The MAX phases: unique new carbide and nitride materials: ternary ceramics turn out to be surprisingly soft and machinable, yet also heat-tolerant, strong and lightweight.* American Scientist, 2001. **89**(4): p. 334-343.
32. Liu, X. Y., Hoagland, R. G., Wang, J., Germann, T. C., & Misra, A., *The influence of dilute heats of mixing on the atomic structures, defect energetics and mechanical properties of fcc–bcc interfaces.* Acta Materialia, 2010. **58**(13): p. 4549-4557.
33. Li, N., Carter, J. J., Misra, A., Shao, L., Wang, H., & Zhang, X., *The influence of interfaces on the formation of bubbles in He-ion-irradiated Cu/Mo nanolayers.* Philosophical Magazine Letters, 2011. **91**(1): p. 18-28.
34. Nizolek, T., Mara, N. A., Beyerlein, I. J., Avallone, J. T., & Pollock, T. M. , *Enhanced plasticity via kinking in cubic metallic nanolaminates.* Advanced Engineering Materials, 2015. **17**(6): p. 781-785.
35. Cai, S., Chen, D., Suo, Z., & Hayward, R. C. , *Creasing instability of elastomer films.* Soft Matter, 2012. **8**(5): p. 1301-1304.
36. Wang, J., Misra, A., Hoagland, R. G., & Hirth, J. P., *Slip transmission across fcc/bcc interfaces with varying interface shear strengths.* Acta Materialia, 2012. **60**(4): p. 1503-

1513.
37. Hoagland, R.G., J.P. Hirth, and A. Misra, *On the role of weak interfaces in blocking slip in nanoscale layered composites.* Philosophical Magazine, 2006. **86**(23): p. 3537-3558.
38. Li, N., Demkowicz, M., Mara, N., Wang, Y., & Misra, A., *Hardening due to Interfacial He Bubbles in Nanolayered Composites.* Materials Research Letters, 2016. **4**(2): p. 75-82.
39. Asta, M., S.M. Foiles, and A.A. Quong, *First-principles calculations of bulk and interfacial thermodynamic properties for fcc-based Al-Sc alloys.* Physical Review B, 1998. **57**(18): p. 11265-11275.
40. Demetriou, M. D., Launey, M. E., Garrett, G., Schramm, J. P., Hofmann, D. C., Johnson, W. L., & Ritchie, R. O., *A damage-tolerant glass.* Nature materials, 2011. **10**(2): p. 123.
41. Crowson, D.A., D. Farkas, and S.G. Corcoran, *Mechanical stability of nanoporous metals with small ligament sizes.* Scripta materialia. **61**(5): p. 497-499.
42. Li, Q. J., Xu, B., Hara, S., Li, J., & Ma, E., *Sample-size-dependent surface dislocation nucleation in nanoscale crystals.* Acta Materialia, 2018. **145**: p. 19-29.
43. Zhou, J., R.S. Averback, and P. Bellon, *Stability and amorphization of Cu-Nb interfaces during severe plastic deformation: Molecular dynamics simulations of simple shear.* Acta Materialia, 2014. **73**: p. 116-127.
44. Wu, K., Zhang, J. Y., Zhang, P., Wang, Y. Q., Liu, G., Zhang, G. J., & Sun, J. , *Fracture behavior and adhesion energy of nanostructured Cu/Mo multilayer films.* Materials Science and Engineering: A, 2014. **613**: p. 130-135.
45. Huang, C.X., Wang, Y.F., Ma, X.L., Yin, S., Höppel, H.W., Göken, M., Wu, X.L., Gao, H.J. and Zhu, Y.T., *Interface affected zone for optimal strength and ductility in heterogeneous laminate.* Materials Today, 2018. **21**(7): p. 713-719.
46. Damadam, M., Shao, S., Ayoub, G., & Zbib, H. M., *Recent advances in modeling of interfaces and mechanical behavior of multilayer metallic/ceramic composites.* Journal of Materials Science, 2018. **53**(8): p. 5604-5617.
47. Buehler, M.J. and A. Misra, *Mechanical behavior of nanocomposites.* MRS Bulletin, 2019. **44**(1): p. 19-24.
48. Chen, J., M.A. Tschopp, and A.M. Dongare, *Role of nanoscale Cu/Ta interfaces on the shock compression and spall failure of nanocrystalline Cu/Ta systems at the atomic scales.* Journal of Materials Science, 2018. **53**(8): p. 5745-5765.
49. Ma, G.C., J.L. Fan, and H.R. Gong, *Mechanical behavior of Cu-W interface systems upon tensile loading from molecular dynamics simulations.* Computational Materials Science, 2018. **152**: p. 165-168.
50. Plimpton, S., *Fast Parallel Algorithms for Short-Range Molecular Dynamics.* Journal of Computational Physics, 1995. **117**(1).
51. Stuckner, J., Frei, K., McCue, I., Demkowicz, M. J., & Murayama, M. , *AQUAMI: An open source Python package and GUI for the automatic quantitative analysis of morphologically complex multiphase materials.* Computational Materials Science, 2017. **139**: p. 320-329.

Chapter 5 Suppression of Shear Band in Hierarchical Cu-Mo Nanocomposites

5.1 Introduction

In this chapter, the microstructures and mechanical behaviour of Cu/Mo nanocomposites with hierarchical architectures are described. When co-sputtering Cu and Mo at high temperatures and relatively lower deposition rates, hierarchical structures or "composites of composites" are produced. They are composed of a matrix of an LCM structure and Cu-rich phases that contain Mo nano-precipitates. Two hierarchical structures are discussed in this chapter. One is named nanocomposite with coarse-length-scale bicontinuous zones, where the feature size in the LCM phase is over 35 nm, whereas in the other nanocomposite with fine-length-scale bicontinuous zones, the feature size in the LCM matrix is only ~ 3 nm. After indentation, shear bands and kink bands found in the monolithic VCM or LCM structures as discussed in Chapter 4 were not observed in the hierarchical nanocomposites. *In situ* nanopillar compression tests in TEM showed that the hierarchical nanocomposite containing fine-length-scale intertwined Cu/Mo phases has very high strength. The hierarchical structure is proposed to play an important role in suppressing shear band formation.

Results on the synthesis and nanomechanical characterization of hierarchical nanocomposites with bicontinuous intertwined Cu and Mo phases will be presented. After significant plastic deformation, shear bands were not observed. Very high flow stresses were

measured in the nanocomposite with fine-length-scale Cu/Mo phases during *in situ* nanocompression test. The results provide insight on producing materials with high strength and good deformability through morphological design.

5.2 Experimental

Cu/Mo nanocomposite with a nominal 50/50 atomic ratio were deposited at high temperatures by DC magnetron sputtering. Transmission electron microscopy (TEM) and scanning TEM (STEM) characterizations were performed on a JEOL2010 and a Cs-corrected JEOL3100. The TEM samples were prepared by focused ion beam (FIB) in FEI Nova200 scanning electron microscope (SEM). The nanocomposites were indented using a Berkovich tip in a Hysitron PI950 Triboindenter with indentation depth up to 350 nm. *In situ* nanocompression experiments in TEM were conducted using a Hysitron PI95 Picoindenter. Load and displacement were measured during the experiments to estimate stress-strain curves assuming uniform cylindrical cross-section of the nanopillars.

5.3 Microstructure and mechanical behavior

5.3.1 Nanocomposite with coarse-length-scale bicontinuous zones

Figure 1.1a shows the cross-sectional STEM images of the 550 nm thin film prepared by depositing both Cu and Mo at 0.3 nm/s on a MgO substrate at 750 ºC. Due to their positive heat of mixing (+19 kJ/mol), Cu and Mo phase separated during deposition [1]. This is further confirmed by the EDS maps on top of the image. The SADP in the inset indicates a BCC Mo(110)//FCC Cu(111) texture. It can be observed that the composite spontaneously formed a hierarchical modulated structure with alternating 100-200 nm thick Mo-rich and Cu-rich layers. The top Mo-rich layer is bicontinuous with interpenetrating Mo and Cu nano-scale phases. Figure

5.1b shows a plan-view STEM image confirming the bicontinuous intertwined morphology. The Mo grains have average size of 35 nm x 110 nm, with interpenetrating copper phase having a ligament size of ~ 10 nm. Figure 1.1c shows that there are nano-scale Mo particles (5.2 ± 2.6 nm in diameter) in the Cu-rich layers. The inset is an atomic image of a Mo particle. It shows that the smaller Mo particles are coherent with the surrounding Cu, presenting an FCC structure. A schematic showing this hierarchical architecture can be found in Figure 1.1d. Because of the high temperature and long deposition duration, extended bulk diffusion could produce this coarse structure with length scale over 100 nm. At the top of the thin film, the bicontinuous structure was conserved because the material here was exposed to high temperature for shorter time.

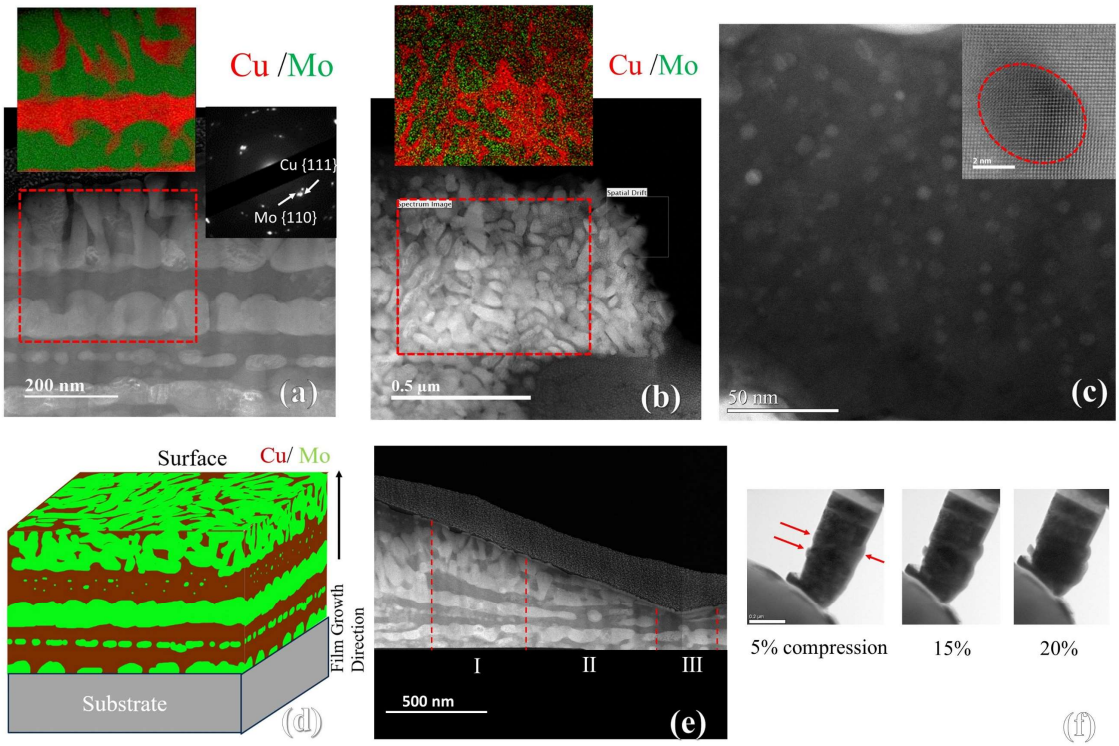

Figure 1.1 (a) Cross-sectional view STEM image of the nanocomposite with coarse-length-scale bicontinuous zones; inset: SADP of the region. (b) plan-view STEM image of the bicontinuous layer. (c) STEM image of the Cu layer showing Mo particles; inset: atomic image of a Mo particle showing FCC structure. (d) Schematics showing the 3D structure of the nanocomposite. (e) STEM image of the deformed sample. (f) TEM images of the nanopillars at different plastic strains during the *in situ* nanocompression test.

Figure 1.1e shows a STEM image of the sample after indentation. After a total indentation depth of 350 nm, shear band formation was not observed. In region I, the Cu layers deformed first at lower strain. In region II, the thickness of the Mo-rich layer also reduced, indicating co-deformation of the Mo-rich and Cu-rich zones. In region III, where the material encounters the largest strains, the Mo grains are flattened in the horizontal direction and a Mo/Cu layered structure can be observed. The vertical dimension of the Mo grains was reduced by 73%.

Nanopillars with a diameter of 250 nm were FIBed to conduct *in situ* compression tests in the TEM. An engineering stress-strain curve is shown as the red curve in Figure 1.2. Figure 1.1f shows TEM images of the pillar at different plastic strains. The maximum flow stress was measured as 1.6 GPa and softening started at 15% plastic strain. During the compression, the thickness of the Cu layers was reduced with Cu extruding out, as indicated by the red arrows. The thickness of the Mo layers did not have a measurable change.

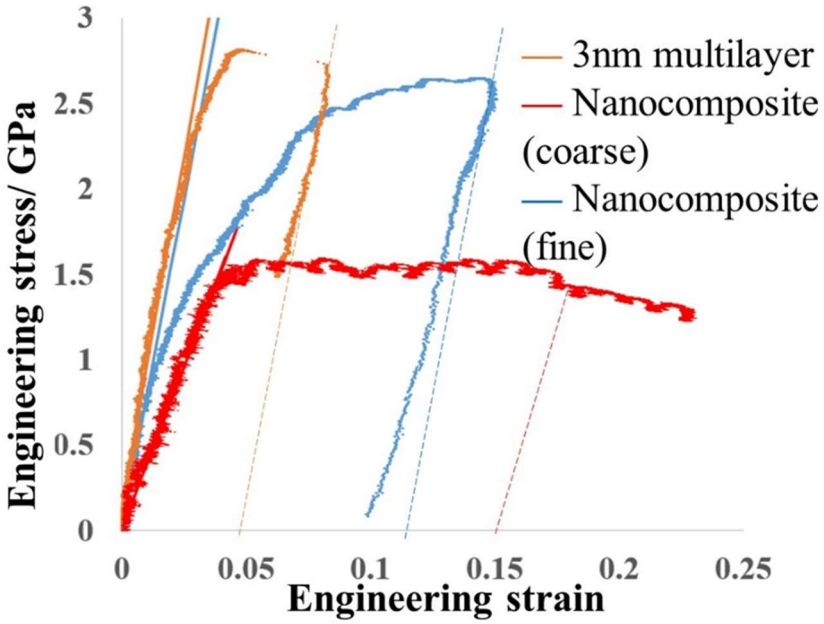

Figure 1.2 Engineering stress-strain curves obtained from the nanopillar compression tests.

The layered structure offers a platform to estimate the shear strength of the semi-coherent fcc Cu/ bcc Mo interface if shear stress can be applied along the interface. Figure 1.3 shows snapshot from a compression test performed when the axis of the indentation tip is 14° off the axis of the pillar. Interface sliding at the lower region of the nanopillar can be observed along the dashed line. The effective shear strength of the interface calculated based on this plane is 0.14 GPa, lower than the shear strength of the Cu/Nb interface (0.4 GPa) [2]. As this is not a standard approach to measure shear strength of an interface, where the interface plane should be 45° off the loading axis, this value cannot be taken as the definitive shear strength of Cu/Mo interface. Its still provides a measure of the relative weakness of the interface under shear as compared to normal loading.

5.3.2 Nanocomposite with fine-length-scale bicontinuous zones

Figure 1.4a shows cross-sectional STEM images of the 1 μm thin film synthesized by depositing both Cu and Mo at 0.63 nm/s on a 650~700 °C Si substrate. Large islands of Cu-rich regions with width ~ 500 nm are distributed in a Mo-rich matrix. Figure 1.4b shows that the Mo-rich matrix has a fan-like appearance, where the alternating Cu/Mo layers stretch in the direction

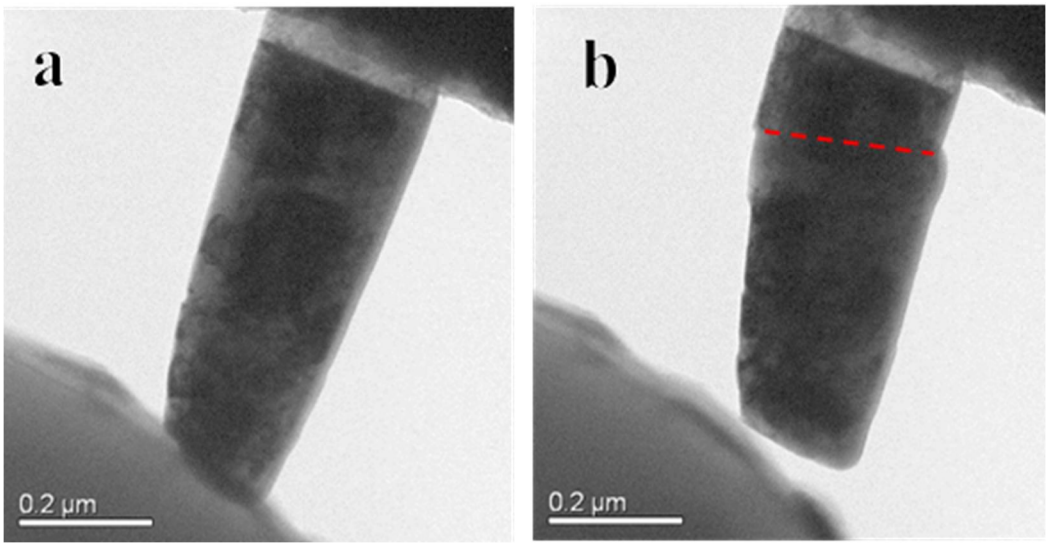

Figure 1.3 TEM images showing interface shearing during an off-axis compression test.

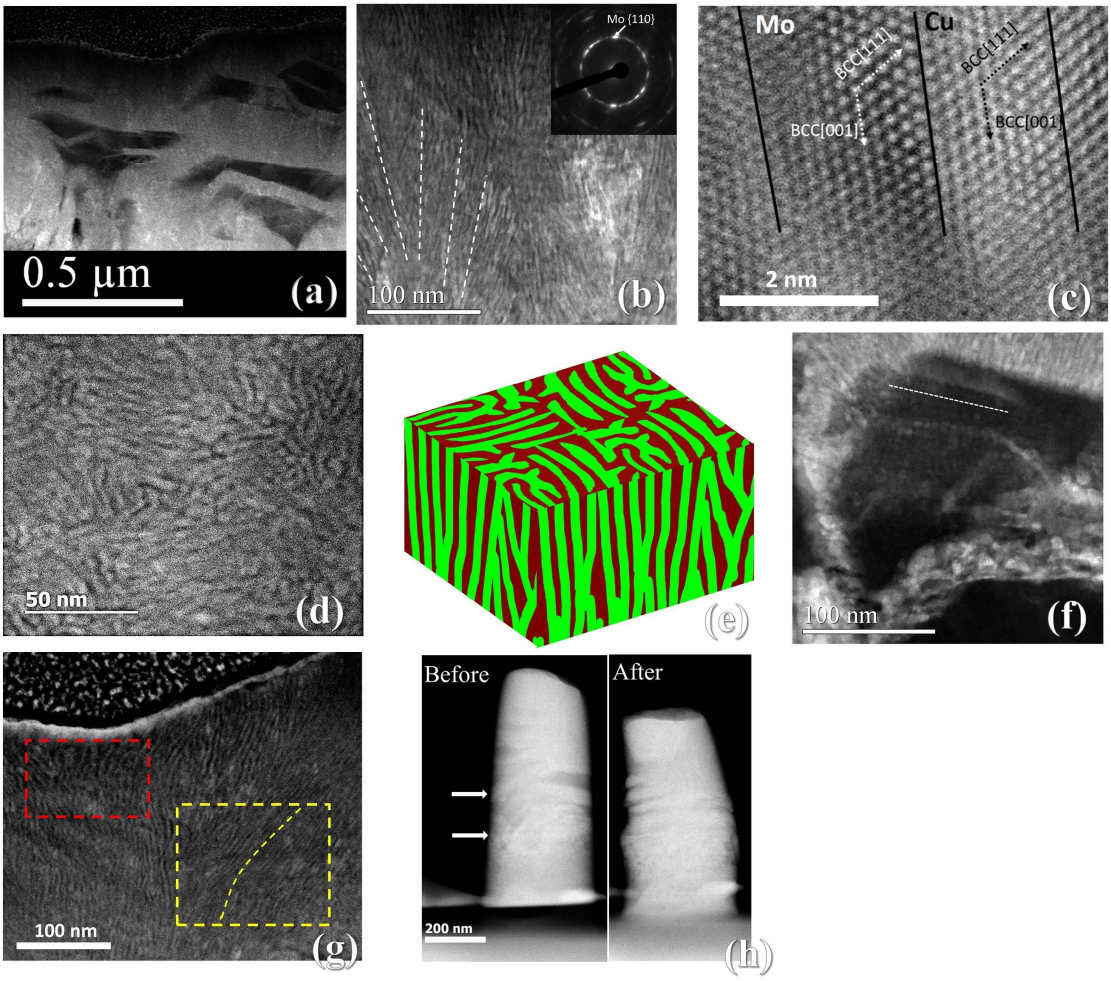

Figure 1.4 (a) Cross-sectional view STEM image of the nanocomposite with fine-length-scale bicontinuous zones. (b) STEM image showing the fine layered structure; inset: SAPD of the region. (c) Atomic image of a few Cu/Mo layers. (d) Plan-view STEM image of the Mo-rich matrix. (e) 3D schematics of the bicontinuous zone. (f) STEM image of the Cu islands. (g) STEM images of the indented area. (h) STEM image of the nanopillar before and after compression test.

perpendicular to the growth front of the composite. The average thickness of Mo layer is measured to be ~ 4 nm while that of Cu is ~ 3 nm. The inset shows a SADP of this region. Clear BCC rings of Mo can be observed, with some weak intensity spots of Cu (111) and Cu (200). Figure 1.4c is an atomic image of a few Cu/Mo layers, showing coherent interfaces with Cu taking the Mo BCC structure. This coherency of metals is typical during the early stage of spinodal decomposition [3]. The continuous (110) ring in the SADP indicates that Cu and Mo in this region across a few tens

of layers are in various orientations. Therefore, the coherency only exists in short range order, across one to a few interfaces. A plan-view sample of the Mo-rich matrix exhibits a bicontinuous morphology as shown in Figure 1.4d. This morphology is expected when the phase separation outruns the deposition process [4]. As a fresh layer is deposited, the existing layer has already decomposed, which serves as a template for the decomposition of the fresh layer, resulting in a structure as shown in Figure 3e. The large Cu-rich islands contain Mo particles with diameters of ~ 2 nm, which tend to align parallel to the upper contour of the island as indicated by the dashed lines in Figure 1.4f. The formation of these Cu islands can be attributed to the higher mobility of Cu than that of Mo. Since the films were naturally cooled after deposition, they were exposed to above-ambient temperatures for a few hours. As such, Cu atoms could have sufficient mobility and time to aggregate into large clusters.

Figure 1.4g shows the STEM image of a deformed region, where the indentation proceeded into 30 % of film and the formation of a shear band was not observed. Immediately under the indent tip, highlighted in the red rectangle, the thickness of both Cu and Mo laminates increased to 5 nm. Slightly away from the tip, as indicated by the yellow rectangle, the laminate thickness was reduced to ~ 1.5 nm. The direction of the lamellae was also shifted towards the shape of the indent tip, as indicated by the dashed line.

The blue curve in Figure 1.2 shows the result of a nanopillar compression test, from which the maximum flow stress was measured to be 2.6 GPa. The nanocomposite began to exhibit non-linear behaviour at 1 GPa while strain softening was not observed up to 12 % plastic strain. Figure 1.4h includes the STEM images of the pillar before and after the test. The diameter of the middle region as indicated by the arrows increased by 16 %, while at the top where there is no Cu island, the diameter only increased by 4.6%. The thickening is uniform throughout the top 200 nm of the

pillar, indicating that the smaller change in diameter is not a consequence of the constraint imposed by indenter friction.

5.4 Discussion

5.4.1 Low-strength hierarchical nanocomposite without shear banding

The absence of shear banding in the nanocomposite with coarse-length-scale bicontinuous zones is expected because the layers are thicker than 100 nm At this length scale, dislocation pile-up against the interfaces (Figure 1.5a) is expected to be the key unit mechanism resulting in intra-layer slip events. In Region I of Figure 1.1e, the Cu-rich zone deforms first because Cu has lower yield strength than Mo. With greater indentation depth, Cu strengthens due to increased dislocation density and reduced layer thickness. In Region II, the strength of Cu reaches that of Mo and co-deformation begins. Under the indent tip (region III), the thickness of both Cu and Mo was reduced to ~20 nm. CLS is expected to occur and accounts for further thinning of the layers. *In situ* testing further confirms the individual deformation behaviour of Cu and Mo. In the nanopillar, Cu layers

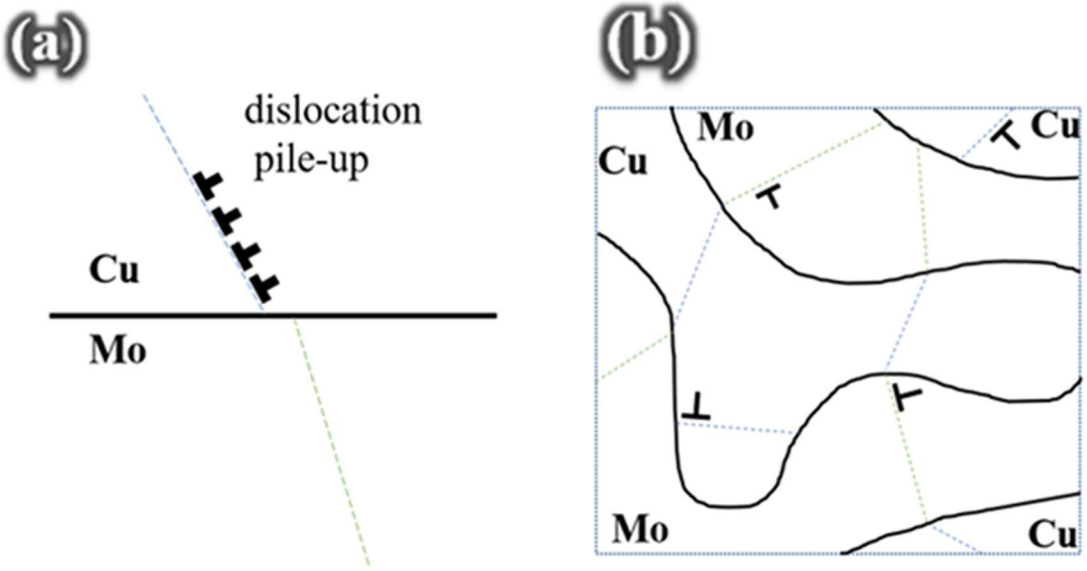

Figure 1.5 (a) dislocation pile-up in submicron scale Cu and Mo and (b) slip systems in a bicontinuous intertwined morphology.

have free surfaces, where they could extrude out during compression. Most deformation thus occurred in Cu layers until the final failure of the nanopillar before Mo-rich layers start to yield. As a result, the maximum stress is relatively low as it measures the stress required to deform the Cu grains, rather than both phases in the composite. The 1.6 GPa flow stress is still considered high for Cu. It accounts for the deformation of highly deformed thin Cu layers constrained by Mo layers.

5.4.2 High-strength hierarchical nanocomposite without shear banding

Figure 1.4g shows the deformed region of the bicontinuous intertwined Cu/Mo phases with fine-length-scale. Immediately under the indent tip as indicated in the red rectangle, the thickness of the alternating layers increases and there are no obvious steps along the interface. CLS is the most probable mechanism to explain this deformation, where the stress is nearly all compressive. As crossing of the interface by dislocations is not involved, continuity of the laminates is preserved. In the area indicated by the yellow rectangle, the thickness of the layers was reduced and the orientation of the layers changed. In this region, the load direction is not parallel to the interface, resulting in both resolved shear and compressive stresses. The compressive stress causes CLS, reducing the layer thickness. The shear stress parallel to the interface activates interfacial slip and thus rotation of the layers. The *post-mortem* characterization did not give information on the deformation of Cu islands because of the irregularity of their shapes. From the *in situ* test, it is shown that the Cu islands exhibited significant plastic deformation. The plasticity starts in the lower-strength Cu islands, which account for the low yield strength of the composite. The Mo particles in Cu islands increase the composite's strength by precipitate hardening. As the Cu is compressed, vertical distance between the Mo particles reduces, further increase the strength of Cu islands. With strain hardening of the Cu islands, plastic deformation of the bicontinuous Cu/Mo

phases begins. The bicontinuous region is expected to have comparable strength with the 3 nm multilayers due to their similar length scale. This explains the high stress measured during the compression test.

The absence of shear banding can be explained by two factors. First, the Cu islands contain large grains of Cu with grain size of a few 100 nm. The progression of shear band would be diverted once it encounters a strain hardening Cu grain. The other factor is the bicontinuous intertwined morphology of the Cu/Mo phases. In the bicontinuous region, the interfaces follow a tortuous path. Therefore, interface slip would not sustainably occur in a localized region as shown in Figure 4b. In addition, the slip systems in the bicontinuous structure are not aligned across multiple ligaments, as depicted in Figure 1.5b. The glide of a dislocation across multiple ligaments is thus very difficult, which involves changing slip plane and Burgers vector. Flow localization in multilayers where slip systems are aligned as shown in Figure 4a is hence not expected to occur for the bicontinuous morphology.

5.5 Conclusions

Two hierarchical structures are investigated in this study: one is a stack of alternating sub-micro layers of Cu-rich phase containing Mo nano-precipitates and Mo-rich phase composed of 10nm Cu and 35 nm Mo ligaments; the other is composed of a matrix of phase-separated Cu-Mo with nanoscale ligaments dispersed with sub-micron scale Cu-rich islands containing Mo nano-precipitates. Due to the layered structure, the former nanocomposite deformed via extrusion of the softer Cu-rich layer, resulting in a relatively soft material. The latter one possesses very high strength as well as good deformability. After large deformation, shear band formation was not observed in the nanocomposite, as opposed to localized shear bands in the multilayers. The

hierarchical structure is proposed to suppress shear banding, where the Cu-rich islands promote deformability and the bicontinuous matrix provides high strength.

5.6 References

1. Li, N., Carter, J. J., Misra, A., Shao, L., Wang, H., & Zhang, X., *The influence of interfaces on the formation of bubbles in He-ion-irradiated Cu/Mo nanolayers.* Philosophical Magazine Letters, 2011. **91**(1): p. 18-28.
2. Li, N., Mara, N. A., Wang, J., Dickerson, P., Huang, J. Y., & Misra, A., *Ex situ and in situ measurements of the shear strength of interfaces in metallic multilayers.* Scripta Materialia, 2012. **67**(5): p. 479-482.
3. Balluffi, R.W., S. Allen, and W.C. Carter, *Kinetics of materials*. 2005: John Wiley & Sons.
4. Lu, Y., Wang, C., Gao, Y., Shi, R., Liu, X., & Wang, Y., *Microstructure map for self-organized phase separation during film deposition.* Physical review letters, 2012. **109**(8): p. 086101.

Chapter 6 Fracture Resistance of Hierarchical Cu-Mo Nanocomposite Thin Film

6.1 Introduction

This chapter describes the investigation on the fracture behavior of high-temperature co-sputtered Cu/Mo nanocomposite through *in situ* 3-point bend test of pre-notched microbeams in SEM. The as-synthesized nanocomposites present hierarchical microstructures composed of a matrix of phase-separated Cu-Mo with nanoscale ligaments dispersed with sub-micron scale Cu-rich islands containing Mo nano-precipitates. Results show a significant crack growth resistance in the hierarchical nanocomposite, several times higher than that measured in Cu-based nanoscale multilayers. Based on electron microscopy characterization, three mechanisms of crack growth resistance in the hierarchical structures are proposed: crack bridging by the Cu-rich layer, crack deflection via shear along the Cu/Mo interface, and multiple cracking. This work demonstrates an approach to increase toughness in high strength nanocomposites through interface micro-structure design.

Metallic nanocomposites (MNCs) are engineered materials composed to two or more metallic phases that have structural features down to nanoscale [1]. They possess unique mechanical behavior owing to the inherent high density of interfaces. Earlier work on MNCs focused on the simplistic multilayer form and size-effect on strength was explored. A “smaller is stronger” trend was observed, where the strength of an MNC can reach one order of magnitude

higher than that of the constituents in the bulk form when the layer thickness is reduced to nanometer regime [2-4]. Recent studies have also shown that, shape of the interfaces play important role in determining the deformation of the MNCs [5]. A hierarchical structure in particular has been shown to possess unique combination of high strength and uniform plastic deformability [6, 7]. What has been lack in the literature is the fracture behavior of these nanocomposites and how would the interface properties affect crack propagation. One challenge lies in designing proper experimental setup to test the fracture toughness of MNCs, which are typically synthesized as thin films that are only a few microns thick. In recent years, several micro-scale mechanical testing approaches have been attempted, including nanoindentation with sharp tips either directly on films or on manufactured pillars [8-13], cantilever beam bending [14-21], and stretching of film/polymer systems [22, 23]. With these approaches, several Cu/X (X being another metal constituent) nano-multilayers prepared via room temperature sequential magnetron sputtering have reported relatively low K_I values ranging from 2 to 7.5 MPa·m$^{1/2}$, with no report of crack growth resistance [21, 24-26]. Nevertheless, some inherent issues prevent these approaches from being universally applied. In nanoindentation based methods, the fracture toughness can be determined from measurements of the lengths of cracks. The calculation of indentation fracture toughness is closely dependent on the type of cracking and can be further complicated by influences of the substrate and sample surface roughness. The specimen geometries used in cantilever beam setup include single cantilever beams [18], clamped beams [19, 20], and double cantilever beams [14, 16]. During the beam bend tests, a pre-notched beam is indented in bending until crack propagates. The sample geometry and the location of the notch have presented a substantial effect on the measurement of fracture toughness. In addition, complicated calibration procedure may be required to obtain the friction coefficient between the indenter and the specimen

[16]. Upon stretching the film/polymer systems, the metal film will first develop cracks perpendicular to the stretching direction, and then delaminate the polymer substrate to buckle transversely. Tedious characterization is then needed across the deformed films on each buckle to estimate the fracture toughness. Besides, the choice of the substrate polymers can complicate the correlated calculation. It has been shown that fracture resistance of micro-scale samples can be size-dependent [27]. Therefore, there is a need for a standardized and facile setup to characterize the fracture resistance of nano-multilayer thin films.

In this work, a technique for measuring the fracture toughness of thin films has been demonstrated. As shown in **Figure 1a**, a micro-scale pre-notched 3-point bend beam was fabricated with focused ion beam (FIB) milling and pressed using an *in situ* mechanical testing stage. The crack propagation and corresponding loading values were recorded. Incorporating the yield strength measured by pillar compression (shown in **Figure 1b**) and the crack opening displacement (*COD*) measured from *in situ* snapshots, the *J*-integral and K_I values could be estimated. As the setup is not a standardized 3-point test, where the beam was connected on two ends, the reported *J* and K_I are not to be taken as definite material properties. However, they can be used to compare samples prepared through similar approaches and with similar dimensions. In this article, the results from bend tests performed on a 5 nm Cu/5 nm Mo multilayer and a Cu-Mo hierarchical nanocomposite, which is composed of a matrix of phase separated Cu-Mo nano-ligaments dispersed with sub-micrometer scale Cu-rich islands containing Mo nano-precipitates, are reported. The results showed that the hierarchical nanocomposite has significantly better fracture resistance compared to the Cu/Mo nano-multilayers and he mechanisms of interface microstructure-induced fracture toughness enhancement in hierarchical nanocomposites are discussed.

6.2 Experimental

To prepare the hierarchical nanocomposite, Cu and Mo with nominally equiatomic composition were co-deposited onto MgO substrate by direct-current magnetron sputtering at 700°C. 99.999% pure Cu and 99.95% pure Mo targets were confocally oriented in the sputtering chamber with a starting pressure below 2.7×10^{-7} Pa. The nominal deposition rate was held at 0.6 nm/s for both metals to grow a 5 μm thick sample. The multilayer Cu/Mo nanocomposite was prepared by sequentially depositing layers of 5 nm Cu and 5 nm Mo at room temperature.

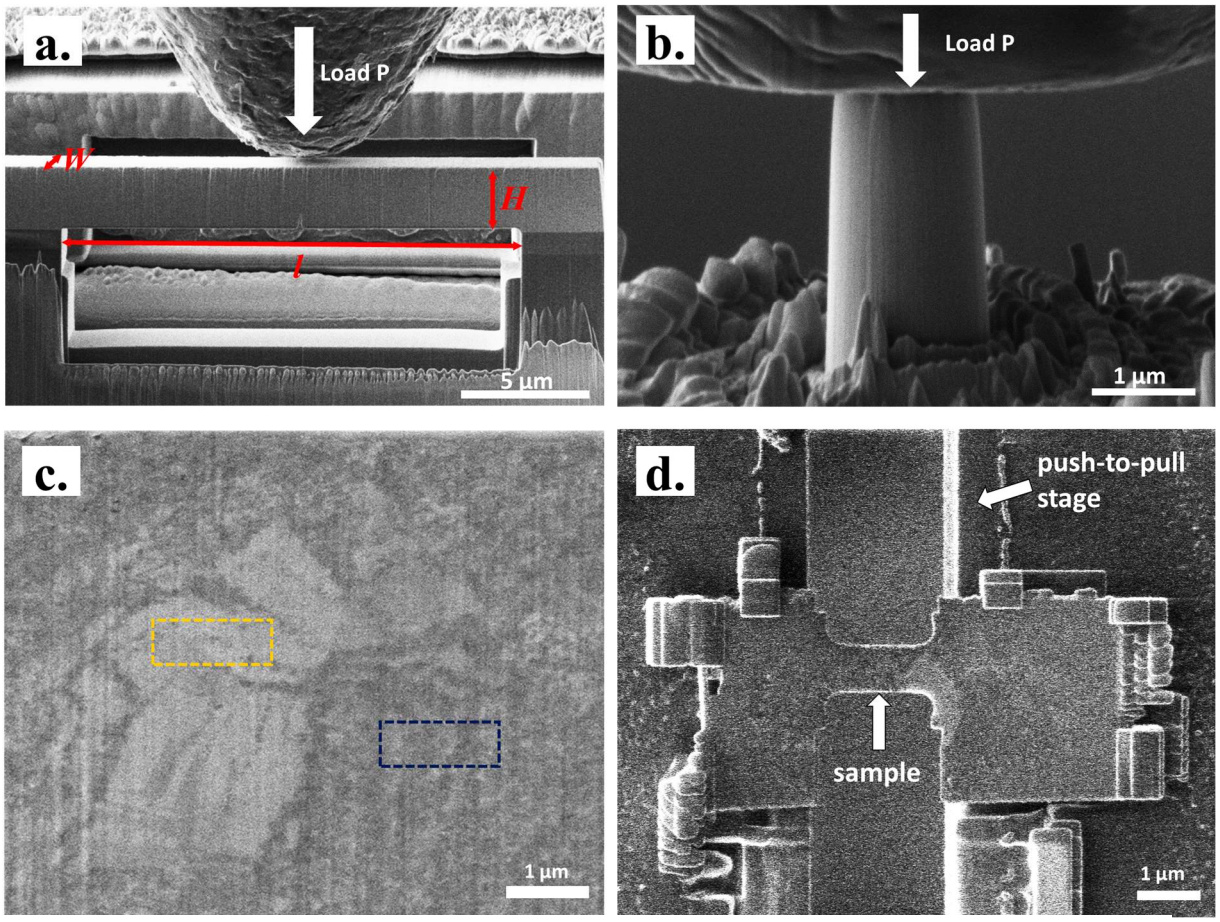

Figure 6.1 SEM images showing the setup for (a) the notched micro-beam bend test, (b) the pillar compression test, (c) sample selection for the *in situ* tensile test, yellow: Cu-rich phase, blue: Mo-rich phase, and (d) tensile test sample glued to the push-to-pull device.

Scanning electron microscopy (SEM) characterization was performed in a Thermo Fisher Magellan 400 SEM. A double Cs-corrected JEOL3100R05 and a Thermo Fisher Tecnai F30 was used to perform transmission electron microscopy (TEM) and scanning TEM (STEM) characterization of the samples. Hysitron PI 85 Picoindenter was used as the loading platform to conduct nanopillar compression tests and notched microbeam bend tests in SEM to measure the yield strength and fracture toughness of the samples respectively. The experimental setup for the pillar compression test and the bend test can be found in Figure 6.1**a** and **b** respectively. A round diamond tip with a radius of ~ 5 μm was employed for the bend test. The compression tests were performed using a diamond flat-punch indenter in displacement control mode at a fixed strain rate of 2×10^{-3}/s. The TEM and mechanical testing samples were prepared using focused ion beam (FIB) in a Thermo Fisher Helios Nanolab DualBeam SEM. At least four tests were performed for each sample to ensure the reproducibility of the data. Employing FIB lift-out technique, micro-sized pieces could be selectively picked from targeted regions of the sample and glued to a Hysitron push-to-pull device using Pt deposition to do tensile test in TEM. As shown in Figure 6.1**c**, rectangular samples can be prepared from the Cu-rich region (brighter in SEM image) and Mo-rich region and transferred to the push-to-pull stage (Figure 6.1**d**). Higher magnification characterization of the microstructure in Figure 6.1**c** is presented in Figure 6.2.

6.3 Results

The cross-sectional annular dark-field (ADF) STEM image of the hierarchical nanocomposite is shown in Figure 6.2**a**, where the film growth direction is vertical from bottom to top. ADF STEM images provide an atomic number contrast, where Cu appears darker compared to Mo. The inset is a selected area diffraction pattern (SADP) of the area, where scattered spots from both body-centered-cubic (bcc) Mo and face-centered-cubic (fcc) Cu can be observed. The

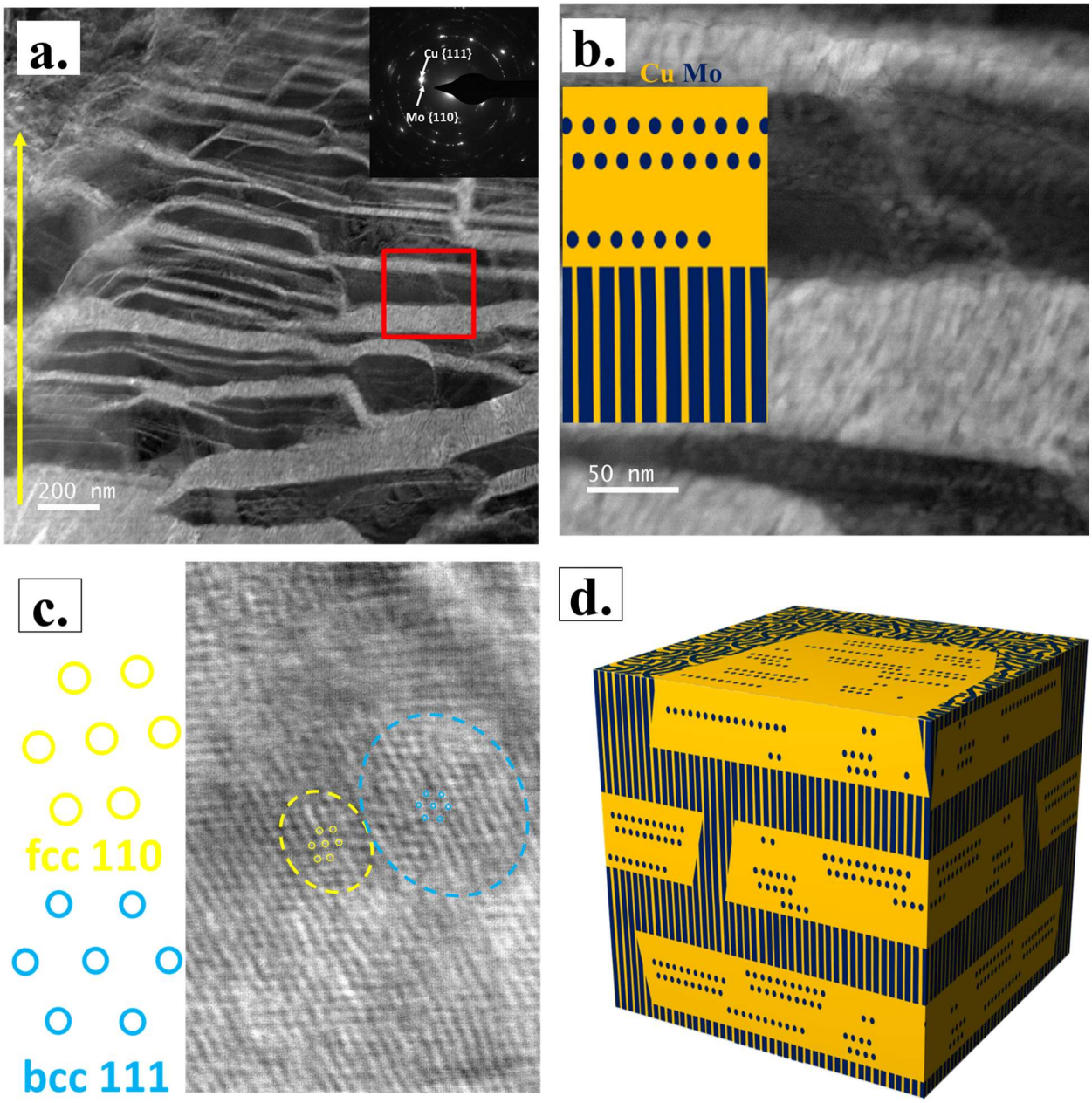

Figure 6.2 Cross-sectional STEM images of (a) the hierarchical Cu-Mo nanocomposite , inset: SADP of the region; (b) the hierarchical Cu-Mo nanocomposite at a higher magnification, inset: schematic of the two phases; (c) atomic resolution inside the Cu-rich domain showing both bcc and fcc Mo precipitates. and (d) schematic showing 3-dimensional structure of the nanocomposite.

clustering of the spots are consistent with a bcc Mo(110)//fcc Cu(111) fiber texture. From the lower magnification overview, Figure 6.2**a**, there appears to be alternating lateral Cu-rich and Mo-rich phases with layer thickness around 100 nm. A magnified image in Figure 6.2**b** shows that each

chemical domain has its own composite structure, forming a "composite of composites", or a multi-length-scale hierarchical architecture. The Mo-rich phase has a lateral concentration modulation (LCM) like composite structure with alternating Cu and Mo ligaments, where the ligament width of Mo is ~ 8 nm and that of Cu is ~ 3 nm. Inside the ~ 100 nm Cu-rich layers, Mo precipitates with diameters below 10 nm can be found. A schematic of the two phases is shown as the inset of Figure 6.2**b**, where Mo is depicted in blue and Cu in yellow. The bright field STEM atomic image in Figure 6.2**c** captured inside the Cu-rich layer shows that a larger Mo particle (~ 5 nm) takes bcc structure, whereas a smaller Mo precipitate (~ 3 nm) exhibits a metastable fcc structure, coherent with the surrounding Cu matix. This size dependent phase change of Mo has also been observed in previous reported hierarchical Cu-Mo nanocomposites [7]. Plan-view imaging of LCM structured Cu-Mo reveals an interpenetrating bicontinuous structure [6, 28]. Incorporating the above information, 3-dimensional structure of the hierarchical nanocomposite is schematically depicted in Figure 6.2**d**.

Another nanocomposite tested in this study is a Cu/Mo multilayer, the TEM image of which can be found in Figure 6.3**a,** where the arrow shows the film growth direction. This multilayer thin film has a columnar structure, with column width around 80 nm, and no inter-columnar porosity was observed. A higher magnification image in Figure 6.3**b** shows that each column is composed of alternating layers of ~ 5 nm Cu and ~ 5 nm Mo. The SADP in the inset indicates a bcc Mo(110)//fcc Cu(111)//interface fiber texture.

Based on the geometry of a three-point bend, the stress ahead of the notch, σ, can be estimated from the loading force, P, as

$$\sigma = \frac{Pl(H-h)}{8I} \quad (1)$$

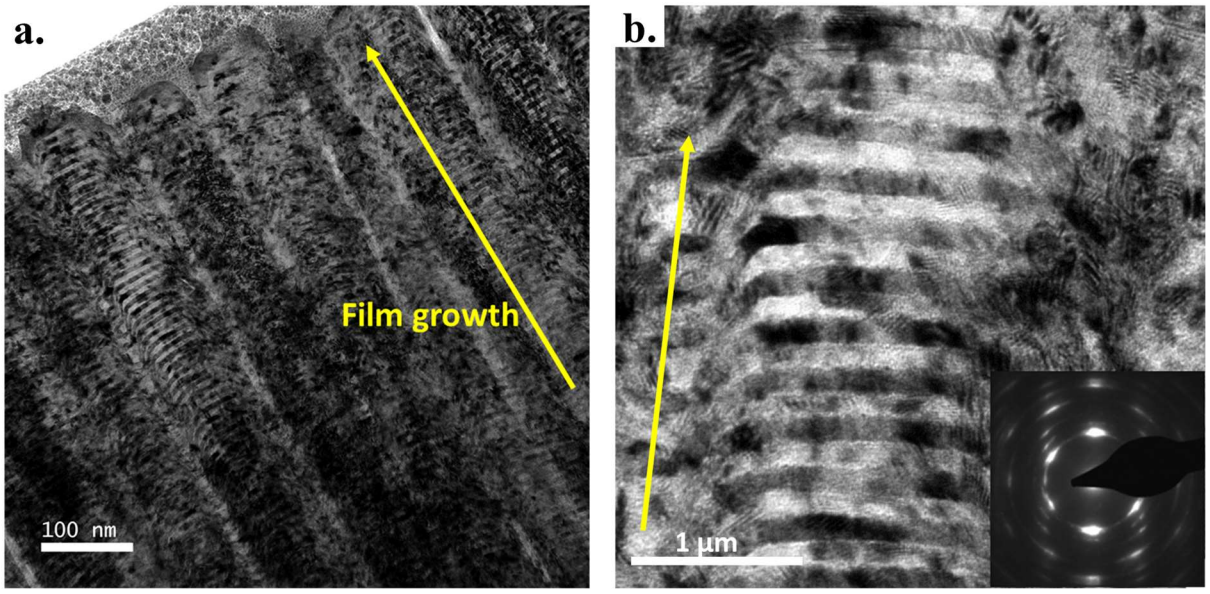

Figure 6.3 Cross-sectional TEM images of the 5 nm Cu/5 nm Mo multilayer nanocomposite at two magnifications, inset: SADP of the region. The yellow arrow indicates the film growth direction.

where *l* is the length of the beam, H is the height, h is the initial notch length, and I is the moment of inertia (Figure 6.1**a**) [29]. I is calculated as $I= W(H-h)^3/12$, where W is the width of the beam. Because the assumption of point contact between the beam and the loading tip for a conventional test is not perfectly satisfied in our experiment, the stress calculated would be an overestimation. Nevertheless, the values can be used to compare different materials examined through the same method. Figure 6.4 plots the crack tip stress vs. deflection at the middle of the beam measured during the bend tests for the two nanocomposites. A smaller load drop, which corresponds to the initiation of crack propagation, is found on the curve of the hierarchical nanocomposite (red) at around 0.7 µm deflection. The stress level further increases, until it plateaus with some fluctuation at ~ 5.2 GPa. It can be observed that on the curve for the multilayer nanocomposite, the beam failed immediately after the crack initiated at 0.55 µm deflection. The beam fractured within one image frame, while the images were captured at a rate about 1 frame/s. Figure 6.5**a** and **b** are snapshots captured during the bend test for the hierarchical and multilayer nanocomposites

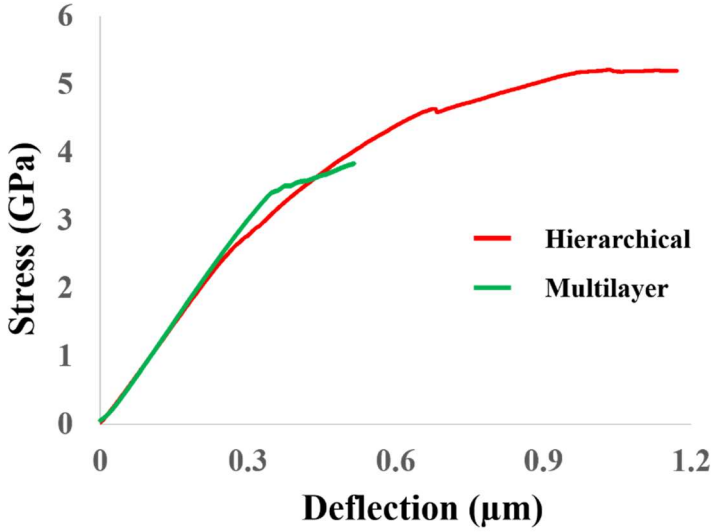

Figure 6.4 Stress-deflection curves for the nanocomposites measured from the *in situ* notched bend tests.

respectively. In Figure 6.5d**,** it is observed that during bending of the 5 nm Cu/Mo multilayer, the easy crack path was along the columnar boundaries, as indicated by the arrows. Within one image frame, the beam fractured, implying a very low resistance to crack propagation. Figure 6.5**c** shows the crack at the end of the test for the hierarchical nanocomposite after indenter tip retraction. Formation of crack branches along multiple directions can be traced, marked by the arrows. The branching occurred during the plateau on the stress curve, which might account for the fluctuations. Figure 6.5**d** shows that during another test, extended shear crack along the interface can be observed, with the shear crack length, L, reaching ~ 500 nm.

To quantify the toughness of the hierarchical nanocomposite with microscale sample size, the following equations can be used, which was obtained from finite element analysis.[30] The strain energy release rate, or *J*-integral has been shown to relate to the crack opening distance, *COD*, and tensile yield strength, σ_y of the material as

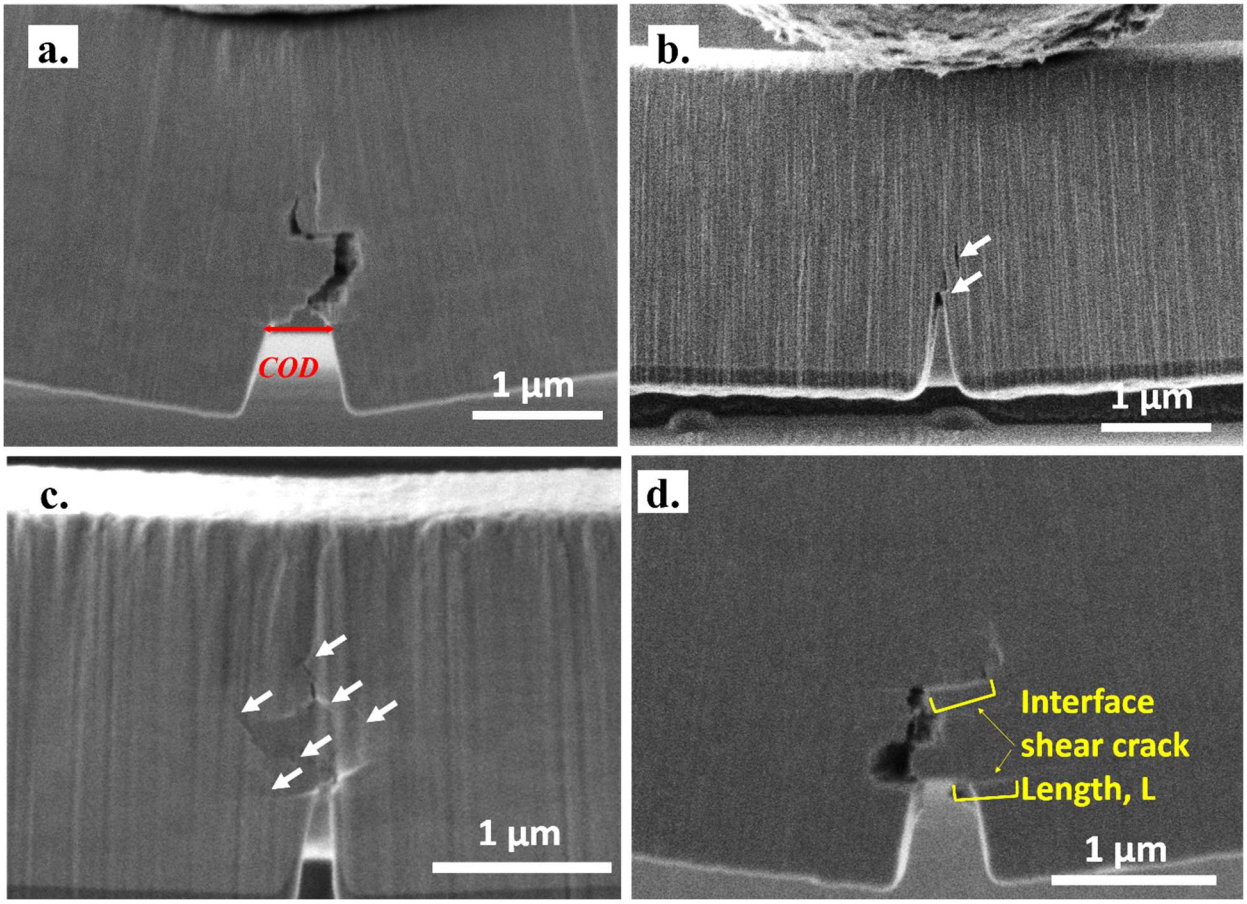

Figure 6.5 Snapshots captured during the in situ tests showing (a) crack opening displacement, (b) crack growth in 5 nm Cu/Mo multilayer, (c) multiple cracking in hierarchical nanocomposite, and (d) crack defection via shear along the Cu/Mo interface in hierarchical nanocomposite.

$$J = d_n(COD)\sigma_y \tag{2}$$

and the stress intensity factor K_I can thus be estimated as

$$K_I = \sqrt{\frac{d_n(COD)\sigma_y E}{(1-\nu^2)}} \tag{3}$$

where E is the elastic modulus, ν is the Poisson's ratio and d_n is a factor dependent on the deformation property of the material. Based on finite element calculations, these equations can be applied to both plane-stress and plane-strain situations, with some adjustment of the d_n value. [30] d_n is as low as 0.2 for non-hardening materials, and approaches 0.8 for materials with an infinite

strain-hardening rate. In the following calculations, an average value of $d_n = 0.5$ is used to estimate the J and K_I. During our *in situ* tensile test of the hierarchical structure, fracture before yielding was observed due to the limitation of microscale tensile test. True σ_y value thus cannot be experimentally measured. The fracture stress measured at 1.4 GPa was used as the lower bound of tensile yield strength for the calculations, while the compressive yield strength measured at 2.5 GPa from nanopillar compression tests was used to calculate the upper bound of J and K_I. Substituting the average modulus of bulk Cu and Mo at 230 GPa, average Poisson's ratio of 0.3, *COD* values measured from SEM frames, K_I and J values of the hierarchical nanocomposite at different crack lengths can be calculated and plotted in Figure 6.5. The data point for the multilayer is measured from the frame immediately before its fracture, which gives a K_{IC} of 1.8 MPa·m$^{1/2}$. The maximum *COD* before fracture of the hierarchical nanocomposite is measured at 480 nm, giving a K_{IC} value at 9.6~13 MPa·m$^{1/2}$ (Figure 6.5**a**). This is significantly higher than the peak K_{IC} values reported from Cu/X metallic multilayer nanocomposites, including Cu/Zr (7.5 MPa·m$^{1/2}$) Cu/Ru (7 MPa·m$^{1/2}$), Cu/Cr (3 MPa·m$^{1/2}$) and Cu/Nb (3.5 MPa·m$^{1/2}$), as listed in Table 1 [24-26]. The low value from the 5 nm Cu/ 5 nm Mo multilayer is a result mostly of easy cracking along the column boundary, which is a common observation for physical vapor deposited nanoscale

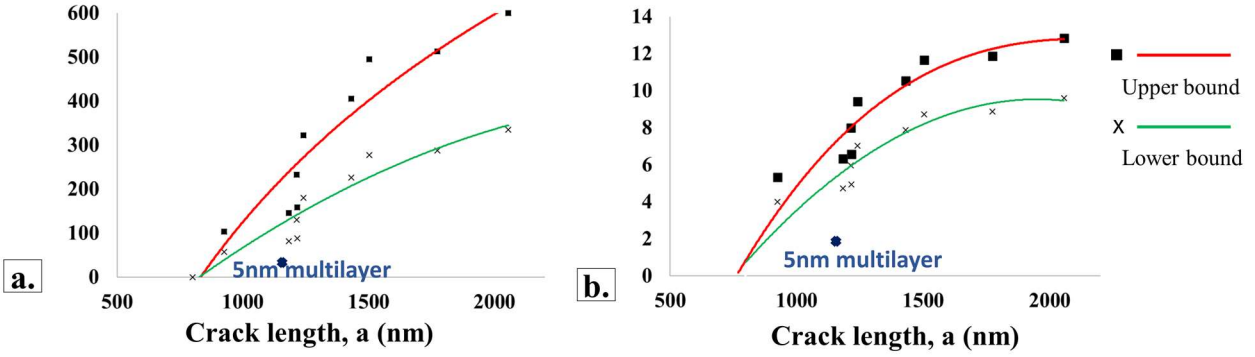

Figure 6.6 Plot of (a) *J*-internal vs. crack length and (b) K_I vs. crack length measured during the bend test for the hierarchical nanocomposite. Upper bound values were calculated using compressive yield strength and lower bound values were calculated using tensile fracture stress.

Table 1. $K_{I,max}$ values measured from Cu-based nanocomposites

$K_{I,max}$ /MPa·m$^{1/2}$	Measurement approach	Material	Structure
9.6~13	Pre-notched bending	Cu-Mo	Hierarchical
0.8~1.8	Pre-notched bending	Cu/Mo	5 nm/5 nm multilayer
4	Stretching w/ polyimide	Cu/Nb	25 nm/25 nm multilayer
7.5	Stretching w/ polyimide	Cu/Zr	25 nm/25 nm multilayer
7	Nanoindentation	Cu/Ru	25 nm/25 nm multilayer
3	Stretching w/ polyimide	Cu/Cr	25 nm/25 nm multilayer

multilayers with layer thickness of a few nm. In Figure 6.5**b**, the *J-integral* for the 5 nm Cu/ 5 nm Mo multilayer correspondent to the peak K_I is calculated and plotted at only 12 J/m^2. On the curve for the hierarchical nanocomposite, the maximum *J-integral* value is measured at~ 600 J/m^2, at the crack length of ~ 2 μm.

To further investigate crack formation in the hierarchical structure, TEM samples were prepared by FIB lift-out from the specimens after the bend test. Figure 6.7**a** shows an ADF STEM

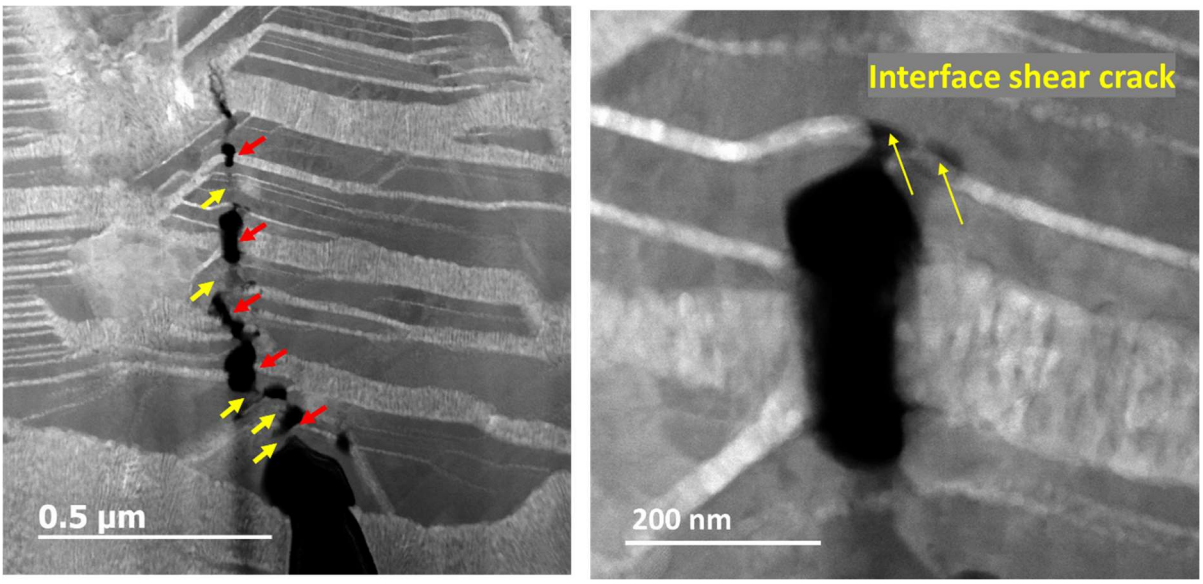

Figure 6.7 STEM images showing (a) crack propagation at an early stage, red arrows: breakage at the Mo-rich layers, yellow arrows: bridging at the copper-rich layers; (b) local shear crack along the interface.

image of a sample after crack initiation. An interesting observation is that the crack is not continuous along its path, where segments of elongated voids along the crack path with length of a few 100 nm were observed. With a closer examination, the voids are mostly accompanied by the breakage of the composite layers, indicated by the red arrows. In-between the voids, Cu-rich layers are still connected with signs of necking after significant plastic deformation, pointed by the yellow arrows.

As described in the experimental section, the Cu-rich phase with Mo nano-precipitates and the Mo-rich phase with LCM nano-ligaments can be tested separately using *in situ* tensile test in TEM. The obtained engineering stress-strain curves are shown in Figure 6.8. The yellow curve is measured from the Cu-rich phase, where the maximum flow stress is at 800 MPa and dislocation mediated plasticity was observed. The inset image taken during the experiment shows that considerable yielding and necking took place in the Cu-rich phase. On the contrary, much higher yield stress was measured in the Mo-rich phase at 2.3 GPa and the sample exhibited localized plasticity and fracture after the peak stress was reached, resulting in limited uniform elongation This shows that there is significant disparity between the mechanical properties of the two composites that make up the hierarchical composite of composites, where the Cu-rich composite exhibits uniform elongation in tension at flow stress significantly higher than pure Cu and the Mo-rich LCM composite is much stronger and exhibiting localized plasticity. It should be pointed out that observations are based on nano-scale tensile tests performed *in situ* in a TEM on thin foils prepared using FIB. In fact, from our nano-pillar compression test, a sample with structure similar to the Mo-rich composite exhibited significant deformability [28].

From these observations, crack propagation in the hierarchical nanocomposite can be described in four stages. At first, the strong but less deformable Mo-rich composite fractures after

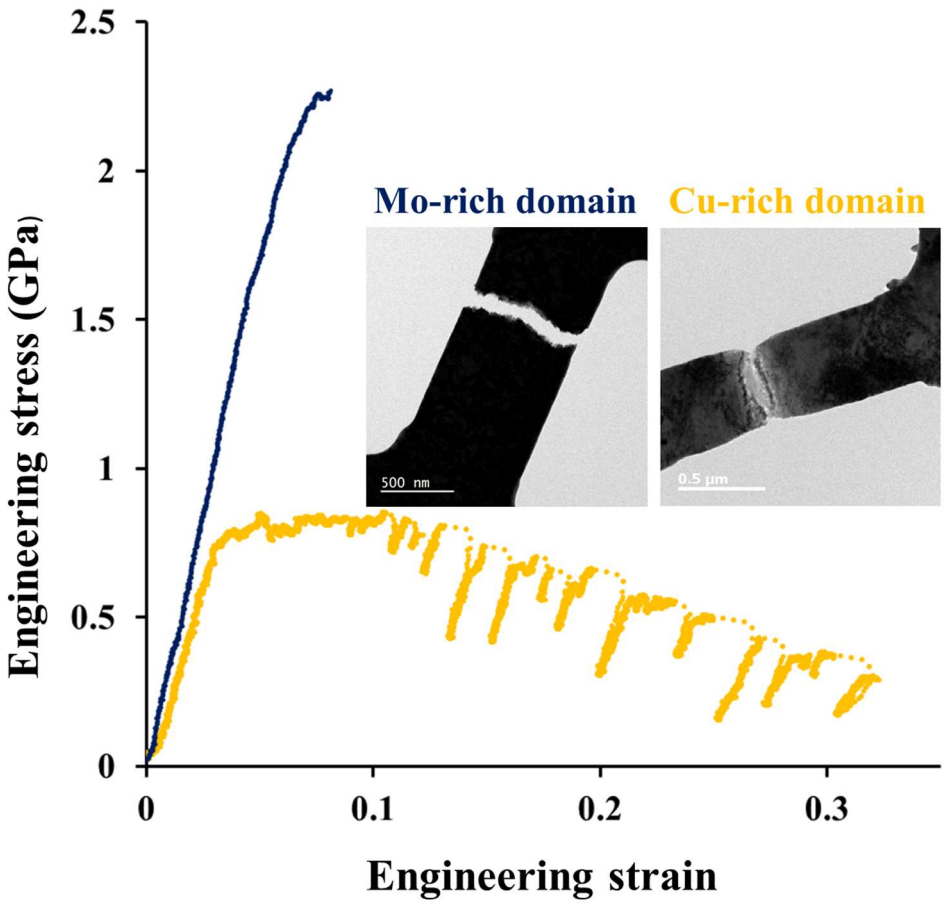

Figure 6.8 Engineering stress-strain curves measured from the *in situ* tensile tests on the Cu-rich composite domains (yellow) and the Mo-rich composite domains (blue) in the hierarchical composite (Figure 1c and d show the locations in the microstructure from where the tensile samples were cut and the test geometry, respectively); inset: snapshots from the tests.

yielding, forming nanovoids. The neighboring Cu-rich layers are still connected and accommodate the strain through plastic deformation, effectively blunting the crack tip and impeding the further opening of the crack surfaces. With extended deformation in the Cu layer, which is the second stage of crack propagation, the void widens, and Cu starts to neck. During the next stage, a new void is initiated in the next Mo-rich layer. Due to the complexity of the internal structure of the nanocomposite, the formation of a new void does not necessarily follow the original crack path. As a result, the crack path deviates with the possibility of branching. Crack deviation and

branching require more energy dissipation for crack propagation, effectively promoting crack growth resistance of the nanocomposite.

6.4 Discussion

6.4.1 Crack initiation

Research on micro-layered structure composed of alternating soft and hard domains have shown that when yielding of the soft layer is involved, two values of stress intensity factor characterize crack growth: (i) the initiation intensity factor, K_N, that is needed for initial crack re-nucleation across the soft layers, and (ii) the crack growth intensity factor, K_R, that is needed for succeeding crack growth [31]. K_N is controlled by crack renucleation in the hard layer in front of the crack tip, whereas K_R may reach a steady-state fracture resistance, K_S, or continuously rising, due to the bridging effect of the intact soft layers. Both K_N and K_R increase as the thickness of the soft layer, t_m, increases. K_R has also been shown to increase with the yield strength and volume fraction of the soft layer.

The tensile tests performed on isolated Cu-rich phase and Mo-rich phase have shown that the tensile ductility of the former far exceeds that of the latter The crack growth mechanisms discovered from the soft/hard multilayers can thus be adequately utilized when analyzing our hierarchical structure. In the small-scale yielding limit, the stress σ along the crack plane with a distance x to the crack tip can be approximated as[32]

$$\sigma \approx \frac{K_I}{\sqrt{2\pi x}} \tag{4}$$

For a crack to renucleate into the next composite layer, the stress at $x=t_m$ needs to exceed the strength of the composite layer, which gives

$$K_N = \sigma_b \sqrt{2\pi t_m} \tag{5}$$

Substituting σ_b = 2.9 GPa, measured from the nanopillar test of nanocomposite of the same structure [28], and t_m = 100 nm, the initiation intensity factor can be calculated at ~ 2.3 MPa·m$^{1/2}$. This value is supposed to be higher than that of a metallic multilayer of the same length scale, owing to the high value of σ_b. In order to increase K_N, the strength of a composite layer needs to be increased, which can be interpreted as a reduction in the ligament size, λ. Meanwhile, the thickness of the ductile layer should be increased. From previous experience on synthesizing hierarchical equiatomic Cu/Mo nanocomposite through co-sputtering, smaller λ is related to higher deposition rate and lower deposition temperature, which, however, also yield smaller t_m [33]. At lower deposition rate, the difference between surface diffusion length of Cu and Mo gets larger, promoting the formation of Cu-rich islands [7]. Therefore, to obtain a higher K_N, intermediate deposition rate and low deposition temperature are recommended, so that the thickness of the Cu-rich layer is boosted while maintaining nano-scale ligament size in the composite layer. For the same purpose, the composition of the co-sputtering can be tuned in favor of Cu.

Several cases of research on metallic multilayers used another approach to estimate K_N when the layer thickness is at nanoscale [24-26], which is also based on the assumption of alternating soft and hard layers [34]. In this model, the advancing crack is blunted by the soft/hard layer interface at the crack tip, dislocation activity would be nucleated and generated in the soft layer. The equilibrium number of dislocations, n, at a given load, can be related to the applied stress intensity K_{app} as

$$n = \frac{4\pi(1-\nu)}{\ln(\overline{t_m}/\bar{r})}\left(\frac{\bar{K}_{app}\sqrt{\overline{t_m}}}{A\sqrt{2\pi}} sin\varphi cos\frac{\varphi}{2} - \bar{\gamma}\right) \quad (6)$$

where ν is the Poisson's ratio, $\bar{r}$= 2.7r_o/b, r_o and b being the effective dislocation core radius and the magnitude of Burgers vector respectively, φ is the angle between the slip plane and the

interface, A is a factor ≈ 1 and $\bar{\gamma}$ is the normalized surface energy of the soft material. Crack initiation would take place when the maximum stress at the crack tip, σ_{tip}, reaches the cohesive strength of the material, σ_c. The normalized crack tip stress, $\bar{\sigma}_{tip}$, is related to n and $\overline{K}_{app}$ as

$$\bar{\sigma}_{tip}\sqrt{n} = 2\sqrt{\frac{2}{\pi}}\overline{K}_{app}\left(1 - \frac{3(sin\varphi cos\frac{\varphi}{2})^2}{\ln\left(\frac{\bar{t}_m}{\bar{r}}\right)}\right) + \frac{12A}{\sqrt{\bar{t}_m}\ln\left(\frac{\bar{t}_m}{\bar{r}}\right)}\bar{\gamma}sin\varphi cos\frac{\varphi}{2} \quad (7)$$

using φ = 45° for generality, ν = 0.33, b= 0.256 nm $\bar{\sigma}_{tip} = \sigma_c$=0.4, and $\bar{\gamma}$ = 0.168 for Cu [35], solving equation (5) and (6), it can be derived that n = 6.9 and $\overline{K}_{app}$ = 0.64. This calculated $\overline{K}_{app}$ value is the normalized K_N, which is related to K_N as $K_N = \overline{K}_N \mu b$, where μ is the shear modulus. Taking μ = 45 GPa for Cu, K_N is calculated at 0.72 MPa·m$^{1/2}$, lower than the value obtained from the previous small-scale yielding model. This model assumes that fracture would also happen in the soft layers, leading to crack initiation. However, as shown in Figure 6.7, the ductile Cu layers still bridge across two sides of the crack, a situation resembling more of the small-scale yielding model, where the crack tip would "leap" from one brittle layer to the next. The soft layer fracture model fails to describe crack propagation in many metallic nano-multilayers, as the bridging effect is not considered. This model underestimates the initiation stress intensity. However, in some commonly used methods to measure fracture toughness of metallic multilayer nanocomposites, including stretching with a polymer film and conducting nanoindentation, the initial bridging stage cannot be captured, and thus ignored in those studies. *In situ* straining multilayers in TEM has shown that bridging, or layer necking, is involved in the crack propagation process and supposed to improve the fracture toughness of the material [36, 37]. Besides, at tens of nms layer thickness, single glide dislocations are confined between the interfaces, so dislocation pile-up-based descriptions for the plasticity in the soft domains do not apply.

6.4.2 Crack growth

It can be observed from Figure 6.5**b** that the crack growth resistance of the hierarchical nanocomposite kept rising with crack length, with a trend to plateau at around 26 MPa·m$^{1/2}$. The loading curve in Figure 6.4 also implies that increased stress is required for crack propagation. Several interface microstructure-related toughening mechanisms are proposed as the following to account for the high crack resistance.

6.4.2.1 Bridging of the crack by the soft Cu-rich layer

As depicted in Figure 6.9, bridging, or layer necking, is a result of plastic yielding of the ductile layer. During crack growth, two effects of bridging come into play, toughening the material. First, plastic deformation ahead of the crack tip blunts the crack tip, reducing local stress intensity. Another effect is from the stretching of the bridges, which adds extra pressure during crack opening. Assuming high deformability of the soft layer, the increased energy dissipation per unit area of a crack, $\Delta\Gamma$, can be approximated as [38]

$$\Delta\Gamma = f_m \sigma u/2 \tag{8}$$

where f_m is the volume fraction of the soft layer, σ is the peak stress, and u is approximately the shear crack length along the interface. Large volume fraction of the ductile layer and high strength of the composite are thus needed to achieve a high K_R, which is similar to the conditions for a high K_N value discussed previously. Calculation of $\Delta\Gamma$ from **Equation 8** requires measurement of interface shear length, u that is describes below.

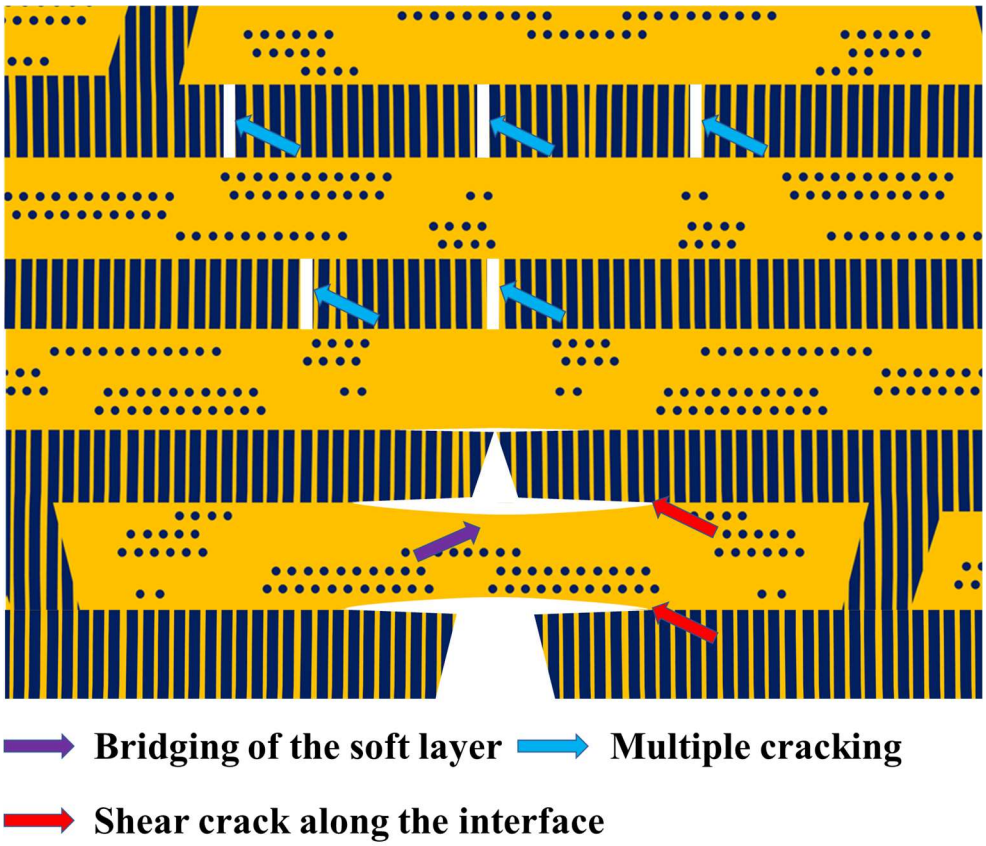

Figure 6.9 Schematic of the three toughening mechanisms. Purple arrow: bridging of the crack by the soft composite; red arrow: shear crack along the interface; blue arrow: multiple cracking.

6.4.2.2 Shear crack along the interface

Another important factor that affects crack growth in the layered structure is the occurrence of shear crack along the interface (Figure 6.9), which is analogous to interface decohesion in metal/ceramic multilayers, especially when the ratio between the shear crack length, L, and the ductile layer thickness, t_m, L/t_m exceeds 3 [31]. The normal stress ahead of the crack front in the brittle layer, σ^*, will be halved when $L/t_m = 10$. As $L/t_m \rightarrow \infty$, $\sigma^* \rightarrow 0$. Shear crack at the interface has been observed in our bend test, as shown in Figure 6.5**d**. In this case, two incidents of large-scale shear crack took place, with $L/t_m \approx 16$, effectively averted the crack growth from the original direction, by offsets of approximately 500 nm. In **Equation 8,** the interface term u can be

approximated as L.[38] Taking f_m = 0.5, σ = 800 MPa, measured from the tensile test, and u = 500 nm, $\Delta\Gamma$ can be calculated at 100 J/m^2, which is in scale with the rising of *J*-integral values in Figure 6.5**b**. Figure 6.7**b** captures a STEM image of interface shear crack at the initiation stage, where the crack has fractured the composite layer, entering the Cu-rich layer. The crack tip is effectively blunted to a radius $\rightarrow\infty$. In addition, plastic deformation of Cu can be observed with void forming at the decohesion site, indicated by arrows in Figure 6.5**b**, dissipating energy during the decohesion process.

Higher preferentiality of interface shear crack is related to a lower shear strength of the interface. Atomic modeling on a Cu/Nb bimetal interface with Kurdjumov-Sachs orientation relationship, which is similar to the Cu/Mo interfaces, revealed that shear along the interface can be activated at ~ 0.5 GPa, much lower than the theoretical strength of the two constituent metals [2]. This value also matches the experimentally measured value at ~ 0.4 GPa [39]. The modeling also shows that such an interface that is weak in shear would attract and absorb nearby dislocations, resulting in dislocation core spreading via shear along the interface. Thus, as the crack tip approaches the interface, dislocations emitted from the crack tip would be absorbed by the interface and relieve the stress field. An interface with lower shear strength can accommodate more dislocations and hence be more effective in hindering crack growth. Atomistic modeling of a fcc/bcc system revealed that while keeping the lattice misfit strain constant, the critical stress for interface shear decreases with increasing heat of mixing.[40] Cu/Mo has a positive heat of mixing of +19 kJ/mol, which is significantly higher than that of Cu/Nb (+3 kJ/mol). Therefore, it is reasonable to assume that Cu/Mo interface has an even lower shear strength compared to Cu/Nb, which accounts for the considerable shear crack length along the interface.

6.4.2.3 Multiple cracking

Multiple cracking, as demonstrated in Figure 6.9, is expected to occur via new cracks nucleating in the crack wake [32]. The local stresses in the wake thus need to exceed the stress ahead of the crack front and also the fracture strength of the hard layer. This can be achieved when bridging traction from the necking ductile layer is enough to raise the wake stress. The magnitude of bridging traction is known to positively depend on the yield strength, volume fraction, and thickness of the ductile layer [32, 41, 42]. In order to reach the required stress, a high strain hardening is necessary in the soft layer. The Mo nano-precipitates in the Cu-rich layer increase the yield strength through precipitate strengthening and those semi-coherent ones also promote strain hardening as dislocations would loop around them, increasing the effective size of the precipitates. As a result, multiple cracking is preferentially activated, delocalizing the crack damage and increase energy dissipation during crack growth. The synergistic activation of multiple mechanisms by virtue of the interface microstructure hierarchy is similar to that observed in many biological and bio-inspired composite materials.[38]

6.5 Conclusions

In this study, the fracture behavior of a co-sputtered Cu-Mo hierarchical nanocomposite, which is composed of parallel horizontal Cu-rich domains (with Mo-rich nano-precipitates that are bcc for relatively larger size and metastable fcc for diameter $\lesssim$ 3 nm) inside of a matrix of phase-separated laterally modulated 8 nm Mo/3 nm Cu nano-ligaments, was measured through *in situ* 3-point bend tests in SEM. The measurements indicate a significant crack growth resistance in the hierarchical misstructure resulting a *J*-integral value of 600 J/m^2 and K_{IC} value of 25.7 MPa·m$^{1/2}$. Similar measurements on a sequentially deposited 5 nm Cu/ 5 nm Mo multilayer revealed K_{IC} of 3.5 MPa·m$^{1/2}$ with no evidence of stable crack growth. In the hierarchical composite of composites,

while the laterally modulated 8 nm Mo/3 nm Cu composite matrix provides high strength of the materials, the Mo nano-precipitate-strengthened Cu-rich composite grains that are relatively softer but are deformable help to impede crack propagation and enhance fracture toughness of the hierarchical microstructure. Three major toughening mechanisms were identified, namely, shear crack along the relatively low shear strength Cu/Mo interfaces between the two composite domains in the hierarchical microstructure, bridging of the matrix cracks by the Mo nano-precipitate-strengthened Cu-rich grains, and multiple cracking resulting in meandering of the crack from its primary plane. Higher volume fraction and layer thickness of the Mo nano-precipitate-strengthened Cu-rich grains, accompanied by a high-strength laterally modulated composite matrix, is expected to yield better fracture resistance of the nanocomposite. This hierarchical microstructure produced via self-organization in elevated temperature co-sputtering provides an approach to tailor the mechanical behavior of a metallic material through multi-phase interface microstructural design at the nanoscale.

6.6 References

1. Buehler, M.J. and A. Misra, *Mechanical behavior of nanocomposites.* MRS Bulletin, **44**(1): p. 19-24 (2019).
2. Hoagland, R.G., R.J. Kurtz, and C.H. Henager Jr, *Slip resistance of interfaces and the strength of metallic multilayer composites.* Scripta Materialia, **50**(6) 775-779 (2004).
3. Wang, J. and A. Misra, *An overview of interface-dominated deformation mechanisms in metallic multilayers.* Current Opinion in Solid State and Materials Science,. **15**(1) 20-28 (2011).
4. Misra, A., J. Hirth, and R. Hoagland, *Length-scale-dependent deformation mechanisms in incoherent metallic multilayered composites.* Acta materialia, **53**(18): p. 4817-4824 (2005).
5. Demkowicz, M.J., *Does shape affect shape change at the nanoscale?* MRS Bulletin, **44**(1): 25 (2019).
6. Cui, Y., Derby, B., Li, N., Mara, N. A., & Misra, A. , *Suppression of shear banding in high-strength Cu/Mo nanocomposites with hierarchical bicontinuous intertwined structures.* Materials Research Letters **6**(3) 184-190 (2018).
7. Derby, B., Cui, Y., Baldwin, J., Arróyave, R., Demkowicz, M. J., & Misra, A., *Processing of novel pseudomorphic Cu–Mo hierarchies in thin films.* Materials Research Letters **7**(1) 1-11 (2019).
8. Sebastiani, M., Johanns, K., Herbert, E. G., Pharr, G. M. M. Measurement of fracture toughness by nanoindentation methods: Recent advances and future challenges. Current Opinion in Solid State and Materials Science 19, 324-333 (2015).
9. Ali, H. P. A. & Budiman, A. Advances in In situ microfracture experimentation techniques: A case of nanoscale metal–metal multilayered materials. Journal of Materials Research 34, 1449-1468 (2019).
10. Lawn, B. & Wilshaw, R. Indentation fracture: principles and applications. Journal of Materials Science 10, 1049-1081 (1975).
11. Sebastiani, M., Johanns, K., Herbert, E. G., Carassiti, F. & Pharr, G. M. A novel pillar indentation splitting test for measuring fracture toughness of thin ceramic coatings. Philosophical Magazine 95, 1928-1944 (2015).
12. Schiffmann, K. I. Determination of fracture toughness of bulk materials and thin films by nanoindentation: comparison of different models. Philosophical Magazine 91, 1163-1178 (2011).
13. Lee, J., Gao, Y., Johanns, K. & Pharr, G. Cohesive interface simulations of indentation cracking as a fracture toughness measurement method for brittle materials. Acta Materialia 60, 5448-5467 (2012).
14. Jaya, B. N., Kirchlechner, C. & Dehm, G. Can microscale fracture tests provide reliable fracture toughness values? A case study in silicon. Journal of Materials Research 30, 686-698 (2015).
15. Jaya, B. N. & Jayaram, V. Crack stability in edge-notched clamped beam specimens: modeling and experiments. International Journal of Fracture 188, 213-228 (2014).
16. Liu, S., Wheeler, J.M., Howie, P. R., Zeng, X. T., Michler, J., & Clegg, W. J. Applied Physics Letters, Measuring the fracture resistance of hard coatings. 102, 171907 (2013).
17. Kupka, D., Huber, N., Lilleodden, E. A combined experimental-numerical approach for elasto-plastic fracture of individual grain boundaries. Journal of the Mechanics and Physics of Solids 64, 455-467 (2014).

18. Di Maio, D. & Roberts, S.D. Measuring fracture toughness of coatings using focused-ion-beam-machined microbeams. Journal of materials research 20, 299-302 (2005).
19. Hintsala, E. D., Bhowmick, S., Yueyue, X., Ballarini, R., Asif, S. S., & Gerberich, W. W. Temperature dependent fracture initiation in microscale silicon. Scripta Materialia 130, 78-82 (2017).
20. Ali, H. P. A., Radchenko, I., Li, N. & Budiman, A. Effect of multilayer interface through in situ fracture of Cu/Nb and Al/Nb metallic multilayers. Journal of Materials Research 34, 1564-1573 (2019).
21. Wang, Y. Q., Fritz, R., Kiener, D., Zhang, J. Y., Liu, G., Kolednik, O., Pippan, R., & Sun, J. Fracture behavior and deformation mechanisms in nanolaminated crystalline/amorphous micro-cantilevers. *Acta Materialia*, *180*, 73-83 (2019).
22. Zhang, J. Y., Wu, K., Zhang, P., Wang, R. H., Liu, G., Zhang, G. J., & Sun, J. An easy way to prepare layered nanoplatelets: Fragment of nanostructured multilayers. Journal of Applied Physics 111, 113519 (2012).
23. Wu, K., Zhang, J.Y., Liu, G., Zhang, P., Cheng, P.M., Li, J., Zhang, G.J. and Sun, J.,Buckling behaviors and adhesion energy of nanostructured Cu/X (X= Nb, Zr) multilayer films on a compliant substrate. 61, 7889-7903 (2013).
24. Zhou, Q. , Zhang, S., Wei, X., Wang, F., Huang, P., & Xu, K. Improving the crack resistance and fracture toughness of Cu/Ru multilayer thin films via tailoring the individual layer thickness. Journal of Alloys and Compounds 742, 45-53 (2018).
25. Zhang, J.Y., Zhang, X., Wang, R.H., Lei, S.Y., Zhang, P., Niu, J.J., Liu, G., Zhang, G.J. and Sun, J. Length-scale-dependent deformation and fracture behavior of Cu/X (X=Nb, Zr) multilayers: The constraining effects of the ductile phase on the brittle phase. Acta Materialia 59, 7368-7379 (2011).
26. Zhang, J.Y., Liu, G., Zhang, X., Zhang, G.J., Sun, J. and Ma, E., A maximum in ductility and fracture toughness in nanostructured Cu/Cr multilayer films. Scripta Materialia 62, 333-336 (2010).
27. Pippan, R., Wurster, S., & Kiener, D., Fracture mechanics of micro samples: Fundamental considerations. *Materials & Design*, *159*, 252-267 (2018).
28. Cui, Y., Derby, B., Li, N., Mara, N. A. & Misra, A. Suppression of shear banding in high-strength Cu/Mo nanocomposites with hierarchical bicontinuous intertwined structures. Materials Research Letters 6, 184-190 (2018).
29. Zhou, H., Mishnaevsky, L., Brøndsted, P., Tan, J. & Gui, L. SEM in situ laboratory investigations on damage growth in GFRP composite under three-point bending tests. Chinese Science Bulletin 55, 1199-1208 (2010).
30. Shih, C. F. Relationships between the J-integral and the crack opening displacement for stationary and extending cracks. Journal of the Mechanics and Physics of Solids 29, 305-326 (1981).
31. He, M. Y., Heredia, F. E., Wissuchek, D. J., Shaw, M. C. & Evans, A. G. The mechanics of crack growth in layered materials. Acta Metallurgica et Materialia 41, 1223-1228 (1993).

32. Shaw, M. C., Marshall, D. B., Dadkhah, M. S. & Evans, A. G. Cracking and damage mechanisms in ceramic/metal multilayers. Acta Metallurgica et Materialia 41, 3311-3322 (1993).
33. Derby, B., Cui, Y., Baldwin, J. K., & Misra, A., *Effects of substrate temperature and deposition rate on the phase separated morphology of co-sputtered, Cu-Mo thin films.* Thin Solid Films **647,** 50-56 (2018).
34. Hsia, K. J., Suo, Z. & Yang, W. Cleavage due to dislocation confinement in layered materials. Journal of the Mechanics and Physics of Solids 42, 877-896 (1994).
35. Rice, J. R. & Thomson, R. Ductile versus brittle behaviour of crystals. The Philosophical Magazine: A Journal of Theoretical Experimental and Applied Physics 29, 73-97 (1974).
36. Hattar, K., Misra, A., Dosanjh, M. R. F., Dickerson, P., Robertson, I. M., & Hoagland, R. G. Direct Observation of crack propagation in copper–niobium multilayers. Journal of Engineering Materials and Technology 134, 021014 (2012).
37. Kramer, D. E. & Foecke, T. Transmission electron microscopy observations of deformation and fracture in nanolaminated Cu-Ni thin films. Philosophical Magazine A 82, 3375-3381 (2002).
38. Heredia, F. E. , He, M. Y., Lucas, G. E., Evans, A. G., Deve, H. E., & Konitzer, D. The fracture resistance of directionally solidified dual-phase NiAl reinforced with refractory metals. Acta Metallurgica et Materialia 41, 505-511 (1993).
39. Li, N., Mara, N.A., Wang, J., Dickerson, P., Huang, J.Y. and Misra, A. Ex situ and in situ measurements of the shear strength of interfaces in metallic multilayers. Scripta Materialia 67, 479-482 (2012).
40. Liu, X. Y., Hoagland, R. G., Wang, J., Germann, T. C. & Misra, A. The influence of dilute heats of mixing on the atomic structures, defect energetics and mechanical properties of fcc–bcc interfaces. Acta Metallurgica 58, 4549-4557 (2010).
41. Marshall, D., Cox, B. N. & Evans, A. G. The mechanics of matrix cracking in brittle-matrix fiber composites. Acta Metallurgica 33, 2013-2021 (1985).
42. Evans, A. G. & McMeeking, R. M. On the toughening of ceramics by strong reinforcements. Acta Metallurgica 34, 2435-2441 (1986).

Chapter 7 Conclusions and future work

7.1 Conclusions

In this dissertation, it has been shown that electron microscopy and *in situ* straining test are essential tools in designing metallic nanocomposites for superior mechanical properties. Using micro- and nano-scale *in situ* mechanical tests, high-strength Cu-Mo nanocomposites with various structures have been systematically investigated. It has been discovered that structural anisotropy would deteriorate plastic deformability due to the formation of localized shear bands or kink bands. On the other hand, uniform deformability was observed in two isotropic structures: a bicontinuous intertwined structure and a "composite of composites" hierarchical structure, where sub-micron scale Cu-rich islands containing Mo nano-precipitates are dispersed in a matrix of phase-separated Cu-Mo with nanoscale ligaments. The hierarchical structure has also been shown to have significant higher fracture resistance compared to the multilayer structure. The work on Cu-Mo nanocomposites produced via self-organization in elevated temperature co-sputtering provides an approach to tailor the mechanical behavior of a metallic material through multi-phase interface microstructural design at the nanoscale.

With the help of nano-pillar compression test and the subsequent post-mortem characterizations, deformation mechanisms of Cu-Mo nanocomposites with different architectures have been revealed. A "composite of composites" hierarchical structure where Cu-rich bicontinuous intertwined when the feature size is below a few tens of nm, the nanocomposites all possess extremely high strength over 2 GPa. The multilayer or VCM structure has been shown to

have very limited deformability due to the formation of shear band. Shear banding is a result of the regulated structure, where no resistance is posed on the shear event once initiated. When the interface is coherent, which is the case where the layer thickness of Cu is below a few nm and Cu takes the Mo bcc structure to reduce lattice energy, the slip system across the interface is continuous. Once the stress is high enough to trigger dislocation transmission across the interface, successive cutting of the neighboring interfaces will follow, leading to localized slip/shear band and failure of the material. When the layer thickness of Cu is increased, Cu recovers its stable fcc structure and forms semi-coherent interface with bcc Mo. The semi-coherent Cu/Mo interface is known to be weak in shear, which means that dislocation can be easily activated along the interface with very low resolved shear stress. In the regulated multilayer structure, once there is a small shear component along the interface that is enough to trigger interfacial slip, through an "avalanche" effect, shear band across multiple layers will form. When the layer thickness is further increased to micron scale, the softer Cu layers will yield first, leading to local extrusion of Cu.

Through co-sputtering of equiatomic Cu and Mo at high temperatures, when the surface diffusion rate exceeds the deposition rate, LCM Cu-Mo nanocomposites can be fabricated, where phase-separated random Cu-Mo patterns stack on each other, producing vertical nano-ligaments. When the ligament size is below ~ 3nm, which at low deposition temperature and thus slow surface diffusion, coherent bcc Cu/bcc Mo interface forms. Due to this continuity of slip system, with a manner similar to that of coherent VCM structure, localized shear band forms under loading. With higher deposition rate and larger ligament size, weak-in-shear fcc Cu/ bcc Mo interfaces present. Owing to the LCM structure, the nanocomposite has high anisotropy in mechanical properties. When loaded along the ligament direction, easy slip along the interfaces results in the formation of kink band, similar to the situation in fiber-reinforced composites and laminate structures.

Although kink band is also a form of strain localization, high stress over 2.4 GPa is still sustained in the nanocomposite. When the deposition temperature is further increased, bulk diffusion can no longer be ignored, leading to a randomized morphology--the RCM structure. In consequence of the structural and mechanical isotropy, RCM nanocomposite has simultaneous high strength and good deformability, where high strength over 2.2 GPa can be maintained after 30% plastic deformation.

At low deposition rates, hierarchical Cu-Mo nanocomposites form, where sub-micron scale Cu-rich islands containing Mo nano-precipitates are dispersed in a matrix of phase-separated Cu-Mo with nanoscale ligaments. The formation of these Cu-rich islands is believed to be a result of large disparity between the surface diffusion lengths of Cu and Mo at low deposition rate. The fast diffusing Cu atoms tend to agglomerate together, forming islands. Samples were prepared from the Cu-rich island and the matrix using FIB lift-out techniques from *in situ* tensile test. The results show that the Cu-rich islands are softer with dislocation-mediated ductility, whereas the matrix is extremely strong but lacks tensile stretchability. Pillar compression test shows that the hierarchical nanocomposite is strong and deformable, where the softer and more deformable Cu-rich islands take up more plastic deformation compared to the matrix, promoting deformability of the nanocomposite, while the matrix provides high strength. Micro-scale pre-notched 3-point bend test was designed to further study the mechanical behavior of the nanocomposites. Based on the results, the hierarchical nanocomposite has much higher fracture resistance compared to the 5 nm / 5nm multilayer and many anther Cu-based metallic multilayers in reported the literature. Three interface microstructure-induced mechanism were discovered to account for the crack hindrance: crack bridging by the Cu-rich layer, crack deflection via shear along the Cu/Mo interface, and multiple cracking.

7.2 Future work

One question remaining unanswered in the Cu-Mo nanocomposite is how the ligament size change the mechanical behavior of the bicontinuous intertwined structure. Limited by the deposition rate and temperature currently achievable in our sputtering chamber, only bicontinuous intertwined (RCM) sample with ligament size of ~ 15 nm has been fabricated. Knowledge on Cu-based multilayers indicates that the deformation mechanisms might change when the ligament size is decreased down to a few nm and increased over a few hundred nm. The current work focused on fabricating nanocomposites through high-temperature co-sputtering. In the future, room temperature deposition followed by annealing could be performed to obtain bicontinuous samples with controlled ligament size and test their mechanical properties. Another limitation on sample preparation is the lack of knowledge on how to control the size, shape and distribution of the Cu-rich islands in hierarchical samples. Hierarchical structures with different volumetric ratio, thickness and spatial arrangement of the Cu-rich islands can be tested and compared with the currently reported nanocomposite to better verify the fracture resistance mechanisms and help better understand crack propagation in a hierarchical architecture. Besides, my work focused on the compression behavior of the nanocomposites, with some exploration on tensile and fracture properties. Further work may include further exploration on tensile and fracture behavior of Cu-Mo nanocomposite using better experimental design that saves sample preparation time and can be conveniently standardized to test other materials and make comparisons.

My work studied the mechanical behavior of Cu-Mo systems, where the semi-coherent fcc Cu/ bcc Mo interfaces, which are weak in shear, present and dominate the mechanical behavior of the material. Following this work, other bi-metallic nanocomposites can be tested and compared with the Cu-Mo nanocomposite of the same structure. For example, Cu-W or Ag-Mo LCM

structures can be fabricated and tested using the nano-pillar compression test to find out the influence of interface properties on the mechanical behavior of a nanocomposite and the conditions where shear band and kink band are triggered. The results will further contribute to the design of nanocomposites that will suppress strain localization and thus solve the long-existing strength-deformability dilemma. Another approach would be doping on of the phases with another metal. For example, in our Cu-Mo system, Nb which has much lower yield strength and elastic modulus compared to Mo can be mixed into Mo. With gradual tuning the content of Nb in Mo from 0 to 100 %, the interface properties would progressively change. Through this approach, the effect of a board spectrum of interface properties on mechanical behavior of the nanocomposites can be systematically investigated. Taking one step further, tri-metallic systems, where three mutually immiscible metal, such as Cu, Mo and Ag, are co-sputtered together can be designed for targeted mechanical performance.